DEVELOPMENT OF THERMALLY CONTROLLED LANGMUIR–SCHAEFER CONVERSION TECHNIQUES FOR SUB-10-NM HIERARCHICAL PATTERNING ACROSS MACROSCOPIC SURFACE AREAS
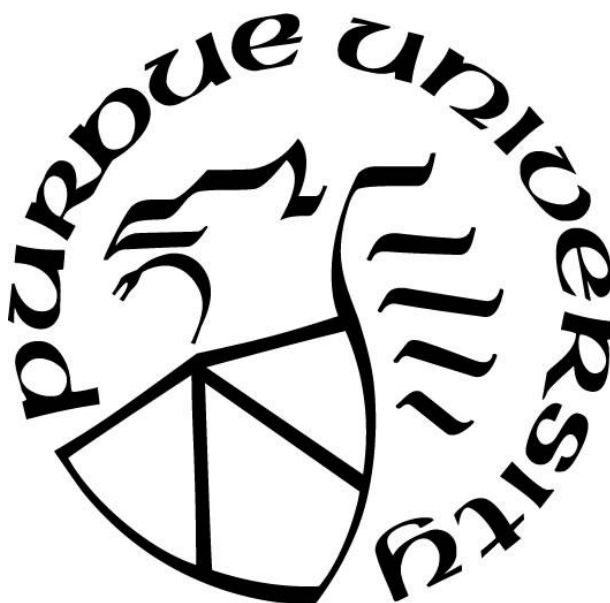
by

Tyler Robert Hayes

A Dissertation

Submitted to the Faculty of Purdue University

In Partial Fulfillment of the Requirements for the degree of

Doctor of Philosophy

Department of Chemistry

West Lafayette, Indiana

December 2020

THE PURDUE UNIVERSITY GRADUATE SCHOOL
STATEMENT OF COMMITTEE APPROVAL

Dr. Shelley A. Claridge, Chair

Department of Chemistry &

Weldon School of Biomedical Engineering

Dr. Christina W. Li

Department of Chemistry

Dr. Chengde Mao

Department of Chemistry

Dr. Alexander Wei

Department of Chemistry &

Department of Materials Science and Engineering

Approved by:

Dr. Christine Hrycyna

Dedicated to my wife, Katelyn Hayes,
my grandparents, Gordon and Janet Burkart,
my parents, Steve and Laura Hayes,
my brother and sister-in-law, Brad and Sarah Hayes,
and the remainder of my FAMILY.

Without your endless love and support,
this would not have been possible

ACKNOWLEDGMENTS

"Feeling gratitude and not expressing it is like wrapping a present and not giving it."

-20th century American author, William Arthur Ward

I have been blessed with a community of individuals who have believed in, and championed for, my education. The privilege and gratitude I feel to have been surrounded by such a large number of selfless individuals who have provided unwavering support and encouragement for my academic success is hard to convey in words; but I will do my best, as you all deserve nothing less.

First, I would like to express my deepest gratitude and appreciation to my PI, Professor Shelley A. Claridge, for believing in my academic potential and serving as an unparalleled source of guidance and support in my pursuit of it. You are the major reason why I chose to attend graduate school at Purdue University. Your expertise in chemistry, enthusiasm for research, and relentless work to ensure all members of our laboratory gain the required skills and knowledge to become leading professional scientists within our field of study is polarizing. Thank you for developing me into the independent scientist I am today. You instilled in me the ability to ask broader questions to solve bigger problems; and how to draw deeper connections between my work and others for new applications. I will always be indebted to you for the research and professional growth opportunities you provided to me as a member of your laboratory. Thank you.

Next, I would like to thank Professor Christina Li, Professor Chengde Mao, and Professor Alexander Wei for serving on my advisory committee. I thoroughly enjoyed the feedback and questions you raised during my original research proposal oral examination and the closing conversation we shared following my dissertation defense. I am honored and humbled to have your approval of my work.

I wish to thank all former and current members of the Claridge Lab for the training, research advice, and friendships you provided. I would like to thank Dr. Shane Russell and Dr. Jae Jin Bang for giving a phenomenal poster presentation during recruitment weekend; I instantly knew I wanted to become a member of the Claridge Lab. Both Dr. Russell and Dr. Bang taught me how to be an effective team leader through observation of their actions as senior lab members. Thank you for being great role models and natural leaders. I would like to further thank

Dr. Bang for training me how to perform a Langmuir–Schaefer conversion and how to acquire publication quality images of our amphiphile monolayers using atomic force microscopy (AFM). Another special thank you goes to my fellow "Trilayer Office Members", Dr. Jae Jin Bang and Dr. Tyson Davis. Sharing the small windowed office with the two of you will always be one of the fondest memories I have of graduate school. How we were as productive as we were with all the laughing we did in that room at each other's expense will never cease to astound me. I will never be able to thank Dr. Davis enough for the friendship we developed upon joining the Claridge Lab in same year. We successfully navigated our teaching responsibilities, graduate courses, cumulative exams, Analytical seminars, OP's, two ACS National conferences, and dissertation defenses by leaning on each other for support and guidance. I couldn't envision a greater friend and lab mate to go through the program together with. Thank you.

I would like to thank Dr. Terry Villarreal for years of laughter and for his guidance in further developing my organic chemistry skillset. I would also like to thank Dr. Ashlin Porter for being a great friend, and for always asking thought provoking questions during my group presentations that often led to better research experiments and output. I would like to thank Jeremiah Bechtold for being a great friend a colleague; I have never met anyone with a more positive outlook on life and natural ability to make friends. I would like to extend a huge thank you to Erin Lang for her friendship and for all her hard work and expertise in preparing tailored gold nanowire solutions for my thermally controlled rotary Langmuir–Schaefer (TCR–LS) conversion manuscript. Additionally, I would like to extend a big thank you to Anni Shi for the molecular modeling expertise she provided to my TCR–LS manuscript, and for her friendship as well. I would like to thank Laura Williams, Anamika Singh, Juan Arango, and Matthew Clark for all our scholarly conversations and the friendships we developed. Finally, I would like to express my gratitude to our former lab technician and instrument designer, David McMillan, for all his hard work in prototyping and fabricating the heated dipper apparatus for my thermally controlled Langmuir–Schaefer conversion manuscript. The practical skills, engineering insight, and machining expertise you provided me cannot be readily found in a textbook. Thank you.

Next, I would like to extend my sincere appreciation to a few of the professional staff scientists and engineers working in the Jonathan Amy Facility for Chemical Instrumentation who either trained me on a specific instrument, or provided their own professional expertise in helping to develop our thermally controlled LS technology. I would like to recognize James Zimmerman

for his significant role and contribution to the success of our TCR–LS conversion project. Your expertise in temperature control and motion control systems was invaluable in the design and fabrication of our heater roller transfer stage. I would additionally like to thank James Zimmerman and Cathy McIntyre for always being willing and able to quickly fix our heated dipper apparatuses when they would experience a mechanical failure. I would like to thank Konrad Kliewer for being one of the best IT site specialists I have ever met. Thank you for always being able to troubleshoot my general computer hardware or software issues. I would like to extend a sincere thank you to Dr. Hartmut Heddrich for the expertise he provided to grant proposal and exploratory research projects that required high vacuum technology, metal deposition, FTIR spectroscopy, and optical microscopy. Finally, I would like to thank Dr. Pat Bishop for the instrumentation training and expertise she shared with me in atomic force microscopy, chromatography, and mass spectrometry. Thank you for always being available to help resolve any technical questions or problems relating to the instruments in the RIC; and for always being quick to share your advice on how maximize instrument performance.

I am indebted to Dr. Christopher Gilpin of the Electron Microscopy Facility for serving as a mentor, friend, and subject matter expert in scanning electron microscopy. The knowledge and skillet I developed in scanning electron microscopy is a direct reflection of your natural ability to effectively communicate your subject expertise; coupled with a strong commitment to develop novice users into experts. Thank you for everything you taught me, and for providing me a true passion for electron microscopy.

Dr. Cynthia Harwood, Professor Marcy Towns, Marybeth Miller and the rest of the General Chemistry Office support staff made my four semesters as a teaching assistant one of my fondest experiences as a graduate student. I cannot begin to express how much I enjoyed serving as a teaching assistant to Professor Towns and Dr. Harwood. Thank you for providing me the opportunity to exclusively TA, CHM111/112, for you during my first two years in the program.

I would like to thank Betty Hatfield, Debbie Packer, Lynn Rider, and Jenalee Converse of the Main Office for always being a friendly source for information relating to the graduate program. Additionally, I would like to extend further appreciation to Lynn Rider for her outstanding guidance and help in the formatting of this dissertation. Thank you.

My acceptance into the Analytical Chemistry Division at Purdue would not have been achieved without the research and early career work opportunities provided to me by

Professor David S. Ballantine of Northern Illinois University and Dr. Robert Sobel of FONA International Inc. Professor Ballantine instilled in me a passion for Analytical Chemistry. I will always be grateful to you for your recommendation of me for an internship with FONA International Inc. prior to my Senior year at NIU. Thank you believing in me, and for providing me the unique opportunity to continue my continuous extraction research initiated at FONA in your laboratory at NIU. Dr. Robert Sobel saw more in me, than I did in myself, when I worked under his supervision in the Analytical and R&I laboratories at FONA. Thank you for getting me out of my comfort zone and pushing me to pursue a PhD in Chemistry. Thank you.

It would be wrong of me to omit my praise and gratitude I have for my former FONA colleagues Benjamin Bunchean, Michael Gundlach, and Kendall Jaderberg. Thank you all for being the best mentors a freshly minted baccalaureate chemist could possibly hope to meet and work amongst in their first 'real' job. You inspired confidence in myself when I didn't have a lot. You taught me how to be a true professional. You will always have a friend in me. Thank you.

I would like to pay my special regards and indebtedness to Mr. Schiller, my high school chemistry, advanced chemistry, and physics teacher whom inspired me to become a scientist and pursue a career in chemistry. I won teaching awards at Purdue because I mirrored your teaching style with my students. It was a privilege to be a student in your class. I will always be grateful to you. Thank you.

I wish to thank my entire FAMILY (Hayes', Burkart's, Carlson's, Hanson's, Hensley's, and Vance's). Thank you ALL for believing in me and cheering me on from afar.

I would not have accomplished my degree without the unconditional love, support and encouragement from my parents, Steve and Laura Hayes, brother and sister-in-law, Brad and Sarah Hayes, and the world's greatest grandparents, and honorary Claridge Lab members, Gordon and Janet Burkart. The late-night phone calls for support, the to-and-from work research updates, and the countless hours listening to me practice my dissertation presentation will never be forgotten. I love you all.

Finally, I wish to thank my wife, Katelyn Hayes. You are everything to me. When I had a hard day on campus, the thought of you and a better future kept me motivated. The degree may be in my name, but it is ours to share. I will always love you (more) and look forward to our future together.

Thank you Purdue University.

TABLE OF CONTENTS

LIST OF FIGURES

ABSTRACT

As hybrid 2D materials are incorporated into next-generation device designs, it becomes more and more pertinent that methods are being developed which can facilitate large-area structural control of noncovalent monolayers assembled at 2D material interfaces. Noncovalent functionalization is often leveraged to modulate the physical properties of the underlying 2D material without disrupting the extended electronic delocalization networks intrinsic to its basal plane. The bottom-up nanofabrication technique of self-assembly permits sub-10-nm chemical patterning with low operational costs and relatively simple experimental designs.

The Claridge Group is interested in leveraging the unique chemical orthogonality intrinsic to the cellular membrane as a means of creating sub-10-nm hydrophilic-hydrophobic striped patterns across 2D material interfaces for applications ranging from interfacial wetting to large-area molecular templates to guide heterogeneous nanoparticle assembly. Using Langmuir–Schaefer conversion, standing phases of polymerizable amphiphiles at the air-water interfaces of a Langmuir trough are converted (through rotation) to lying-down phases on 2D material substrates. Using room temperature substrates, transfer of amphiphiles to a lowered substrate results in small domains and incomplete surface coverage.

Recognizing that heating the substrate *during* the LS conversion process may lower the energy barriers to molecular reorientation, and promote better molecular domain assembly, we developed a thermally controlled heated transfer stage that can maintain the surface temperature of the substrate throughout the deposition process. We found that heating *during* transfer results in the assembly of domains with edge lengths routinely an order of magnitude larger than transfer using room temperature substrates that are more stable towards rigorous repeat washing cycles with both polar and nonpolar solvents.

To promote the effectiveness of the LS conversion technique beyond academic environments for the noncovalent functionalization 2D material substrates for next-generation device designs, we designed and built a thermally controlled rotary stage to address the longstanding scaling demerit of LS conversion. First, we report the development of a flexible HOPG substrate film that can wrap around the perimeter of the heated disk and can be continuously cycled through the Langmuir film. We found that thermally controlled rotary (TCR) LS conversion can achieve nearly complete surface coverage at the slowest translation speed tested (0.14 mm/s).

TCR–LS facilitates the assembly of domains nearly 10,000 μm^2 which were subsequently used as molecular templates to guide the assembly of ultranarrow AuNWs from solution in a non-heated rotary transfer step. Together, these findings provide the foundation for the use of roll-to-roll protocols to leverage LS conversion for noncovalent functionalization of 2D materials. A true roll-to-roll thermally controlled LS conversion system may prove to be advantageous and a cost-efficient process in applications that require large areas of functional surface, or benefit from long-range ordering within the functional film.

CHAPTER 1.   INTRODUCTION

In October of 2004, Konstantin Novoselov, Andre Geim, and co-workers reported the direct observation of the electric field effect (*i.e.* the ability to modulate the electric conductivity of a material through an applied external electric field), in atomically thin carbon films.[1] Remarkably, these scientists were able to isolate single-layer graphene sheets through the repeated mechanical exfoliation of highly oriented pyrolytic graphite (HOPG) using Scotch tape; producing the first two-dimensional (2D) material in the world.[1] Immediately, a scientific rush ensued to characterize the material properties of graphene.[2-4] As the unprecedented properties of graphene were reported,[5-9] interest expanded into the isolation and characterization of other 2D materials such as transition metal dichalcogenides (TMD),[10-12] hexagonal boron nitride (h-BN),[13] and black phosphorus (BP).[14] In the sixteen years following the discovery of single-layer graphene by Novoselov, Geim, and co-workers, not only have numerous 2D materials been isolated and studied,[3-4, 15] they have been incorporated into electronic[16-20] and optoelectronic devices,[21] energy devices,[22] and sensors.[23-25]

A central challenge within the fields of materials chemistry and surface science is developing nanofabrication techniques that can precisely control sub-10-nm chemical patterning over macroscopic areas of layered 2D materials for incorporation into next-generation devices.[26-28] An 'ideal' nanofabrication method would permit high patterning throughputs with near atomic precision, low operational costs, and minimal introduction of structural defects.[26] While no single nanofabrication method has been established that can claim all the figures of merit above, substantial scientific progress has been made towards this challenging enterprise through extensive development of "top-down" and "bottom-up" nanofabrication techniques.

Briefly, top-down nanofabrication techniques leverage different forms of lithography (*e.g.* optical (EUV), E-beam, soft, nanoimprint, block copolymer, and scanning probe) to obtain nanostructures with dimensions substantially less than 100 nm from a larger starting material.[26] Optical (EUV) and E-beam lithography have been extensively used within the electronics industry for fabrication of electronic circuitry. While these two top-down nanofabrication techniques offer highly controllable spatial patterning capabilities into the sub-10-nm regime,[29] low sample throughput and high operational costs are significant drawbacks.[26] Conversely, bottom-up nanofabrication techniques (*e.g.* atomic layer deposition, sol-gel nanofabrication, molecular self-

assembly) leverage the self-assembly of atoms and molecules to build up nanostructures.[26] Of the bottom-up nanofabrication techniques, molecular self-assembly on 2D materials permits sub-10-nm spatial resolution with relatively low process complexity and associated costs.[26] Unfortunately, control over the molecular self-assembly into precise patterns with discrete template positioning across a substrate is substantially more limited.

In recent years, hybrid 2D materials have begun to be incorporated into next-generation device designs.[21, 30-34] Noncovalent functionalization with organic molecules[35-42] or inorganic nanoparticles[43-44] is often leveraged to modulate the physical properties of the 2D material without disrupting the extended electronic delocalization networks intrinsic to its basal plane.[35] For decades, it has been known that polycyclic hydrocarbons and molecules with long alkyl chains form stable, noncovalently adsorbed, lying-down phase monolayers at the interface of 2D materials (*e.g.* graphene, HOPG, MoS$_2$).[45-47] The adsorption of polycyclic hydrocarbons on graphitic surfaces is driven primarily by π-π interactions between the graphitic hexagonal lattice and the aromatic ring structure of the polycyclic hydrocarbon.[36] For long chain hydrocarbons, excellent epitaxial match between the graphitic hexagonal lattice and zig-zag alkyl backbone of the hydrocarbon promotes molecular adsorption.[36]

Long chain hydrocarbons are often functionalized with diacetylene reactive groups to promote lateral (in plane) strengthening within the monolayer upon photopolymerization of the diyne to yield the ene-yne conjugated polymer,[48] since the per methylene group intermolecular forces amongst adjacent long chain alkanes are relatively weak (~5 kJ/mol of CH$_2$).[49] Research interest in noncovalently adsorbed diacetylene monolayers on HOPG,[48, 50] graphene,[51] and MoS$_2$[52] surfaces was driven by the potential of the ene-yne conjugated polymer to serve as a molecular wire,[53] since the photopolymerization process results in a slight topographic protrusion of the polymer backbone away from the surface of the 2D substrate.[54-55]

In the Claridge Lab, we are interested in leveraging amphiphilic lipid species that contain an internal diyne moiety to create more robust noncovalently functionalized monolayer templates upon photopolymerization.[56-57] Herein, we utilize throughout the dissertation, the photopolymerizable diyne phospholipid species 1,2-bis(10,12-tricosadiynoyl)-*sn*-glycero-3-phosphethanolamine (diyne PE) for all experimental studies. Previous work in our group has shown that diyne PE forms a sitting-phase upon adsorption to HOPG in which its two alkyl tails are aligned in epitaxy with the hexagonal lattice of graphite, and the terminal primary amine of the

headgroup projecting away from the interface towards its local surrounding environment.[56] Atomic force microscopy (AFM) revealed that diyne PE molecules form lamellar domains along the HOPG surface through drop-casting and Langmuir–Schaefer conversion (more detail below) with ~6 nm periodicity.[56] Further analysis using semi-empirical molecular modeling, and molecular dynamics simulations revealed diyne PE aligns in head-to-head geometry on the surface of HOPG.[56]

There are several common molecular self-assembly methods that can facilitate noncovalent functionalization of 2D material surfaces; they include: drop-casting from organic solvents,[48, 58-59] flow-induced wicking,[60-61] solution-shearing,[62] and deposition from Langmuir films.[53, 56, 63-64] While drop-casting from organic solvent requires minimal experimental effort to achieve noncovalent molecular assembly over small areas, domain heterogeneity over larger areas often occurs due to significant challenges that arise in controlling the solvent drying front. Long-range ordering of large polyaromatic hydrocarbons on HOPG has been demonstrated using flow-induced wicking and solution-shearing; both of which are modified drop-casting methods.[60-62] Molecular self-assembly using the solution processing techniques outlined above often result in significant challenges when attempting to generate long-range molecular ordering, or assembly over large substrate areas, for long chain amphiphiles and other important groups of molecules. Fortunately, long-range self-assembly of amphiphilic molecules on solid substrates can be achieved using Langmuir transfer techniques.[64]

Central to all Langmuir transfer techniques, molecular films of amphiphiles are preordered to a desired packing density through the compression of movable trough barriers at the air-water interface of a Langmuir trough prior to being transferred to a material substrate that has been vertically brought into contact with the Langmuir film. The orientation of the vertically lowered material substrate with regards to the Langmuir film surface establishes whether the transfer is referred to as Langmuir–Blodgett, or Langmuir–Schaefer transfer. In Langmuir–Blodgett, LB, transfer the substrate is oriented perpendicular to the Langmuir film, and drawn vertically through it.[65-66] Conversely, in Langmuir–Schaefer, LS, transfer the substrate is oriented parallel to the Langmuir film, then lowered into contact, and then withdrawn.[67] In both LB and LS transfer, ordered standing phase Langmuir films are patterned as standing phase molecular films to the receiving substrate.[64, 68] Our group[56-57, 69-70] and others[53-54, 71-72] have shown that LS transfer can also be used to functionalize 2D materials with lying-down monolayers through the conversion of

standing phase Langmuir films to ordered lying-down phases on 2D substrates, in a process we refer to as LS conversion. In LS conversion, the Langmuir film undergoes a fundamental reordering (molecular rotation) from a standing phase to a lying-down phase on the receiving substrate. While traditional LS conversion has been leveraged often by researchers to prepare noncovalently adsorbed SAMs on layered 2D material substrates for scanning probe investigations,[53-54, 71-72] the domain sizes reported were rather small (often ~100 nm in edge length) and likely not robust enough to withstand solution processing conditions employed in device fabrication protocols .

With the heightened demand for novel hybrid materials to be used in upcoming device designs, it has become increasingly more important to develop scalable nanofabrication transfer processes. In addition to being scalable, nanofabrication transfer processes should be designed to facilitate large-area noncovalent functionalization of 2D material surfaces with large ordered molecular domains. For LS conversion, the most commonly associated demerits include: 1) incomplete surface coverage of molecular domains across the substrate, 2) limited ability to produce domains larger than a few-μm in edge length, and 3) limited throughput due to the sequential nature of the deposition process and limit on practical trough sizes. In this work, two transfer protocols are detailed that not only improve upon the listed disadvantages of LS conversion above, but also promote new unique opportunities using large-area diyne PE SAM domains to serve as molecular templates to direct the assembly of other heterogeneous nanostructures (here AuNWs).

In Chapter 2, we demonstrate that controlling the temperature of the 2D material substrate *during* LS conversion can lead to significant increases in both the extent of monolayer transfer and the size of the assembled molecular domains of diyne PE on HOPG using a temperature-controlled transfer stage. The transfer stage is readily attachable to the automated vertical dipper of a commercial Langmuir trough. Postulating that applying heat may lower the energy barriers to the molecular reordering of the standing phase at the air-water interface to the lying-down phase on the receiving substrate *during* LS conversion, we tested two different heating routes: 1) fast quench, and 2) *in situ* annealing. For the fast-quench method, the substrate is heated prior to transfer and then allowed to cool rapidly upon contact with the Langmuir film. Conversely, when transferring *via* the *in* situ annealing method, the substrate is heated prior to transfer and then maintained at the setpoint temperature while in contact with the Langmuir film. We show that the polymerized

molecular domain structure is substantially different using fast-quench versus *in situ* annealing heating methods at elevated temperatures. Further comparison of polymerized monolayer structure is made between heated samples *during* LS conversion (fast-quenched, *in situ* annealed) and room temperature LS converted samples subjected to post-transfer annealing at 50 °C for 60 min. Additionally, we investigate the relationship between substrate setpoint temperature and domain edge contour density after 1 min transfers to identify the optimum temperature range that yields the largest ordered domains. Since *in situ* annealing domain sizes were routinely an order of magnitude larger than room temperature LS converted samples, we subjected polymerized room temperature and 70 °C *in situ* annealed samples to a series of solvent washing assays to compare their relative stabilities towards solution processing. We found that polymerized monolayers of diyne PE transferred through *in situ* thermal annealing exhibit enhanced stability towards repeated washing cycles with polar and nonpolar solvents versus polymerized room temperature LS converted samples.

In Chapter 3, we address the limited throughput barrier associated with LS conversion that keeps the technique from being leveraged more broadly for the noncovalent functionalization of 2D materials with sub-10-nm chemically orthogonal striped phases of lying-down amphiphiles. Drawing inspiration from industrial roll-to-roll processing techniques, we designed and fabricated a thermally controlled rotary transfer stage to examine potential contributors to successful roll-to-roll LS conversion for industrial implementation. To achieve thermally controlled Langmuir-Schaefer (TCR-LS) conversion, we designed a pliant HOPG substrate film that can be tightly wrapped around the periphery of the thermally controlled copper disk so that during the continuous cycling into and out of contact with the diyne PE Langmuir film the substrate is heated evenly. Furthermore, we investigate how the translation rate of the substrate film impacts both the surface coverage and domain size distribution in five test zones along the length of the flexible substrate film. Nearly complete surface coverage was obtained along the entire length of the film for the slowest tested translation rate (0.14 mm/s). Domain size analysis revealed that TCR–LS can produce very large domains (nearly 10,000 μm^2), which were subsequently used as molecular templates to guide the assembly of ultranarrow AuNWs through a sequential non-heated rotary transfer process. Our findings suggest roll-to-roll transfer methods could be used to leverage thermally controlled LS conversion for large-area noncovalent functionalization of 2D materials.

CHAPTER 2.   MULTIMICROMETER NONCOVALENT MONOLAYER DOMAINS ON LAYERED MATERIALS THROUGH THERMALLY CONTROLLED LANGMUIR–SCHAEFER CONVERSION FOR NONCOVALENT 2D FUNCTIONALIZATION

2.1   Introduction

Controlling surface functionalization of 2D materials has emerged as a major requirement in applications including nanoelectronics and the preparation of hybrid materials.[35-36, 73-74] To preserve electronic conjugation within the 2D layer, substrates are often functionalized noncovalently, using lying-down monolayers of functional alkanes or polycyclic aromatic hydrocarbons that experience strong van der Waals interactions with the substrate.[35-36, 50, 58, 75-79] Ligand–substrate interactions can then be used to modulate substrate electronic structure,[80-85] while the exposed face of the monolayer controls interactions with the environment (e.g. interfacial wetting, analyte binding, growth of gate oxides).[56, 69, 86-90] Although individual molecule–substrate interactions are relatively weak, molecules incorporating a polymerizable group (e.g. internal diyne, Figure 2.1) can be assembled and subsequently polymerized to increase the robustness of the functional interface.[40, 48, 53, 55-56, 86, 91] Jointly, these capabilities confer utility as a sub-nm thick interlayer for hybrid materials that require controlled coupling to the layered material structure.
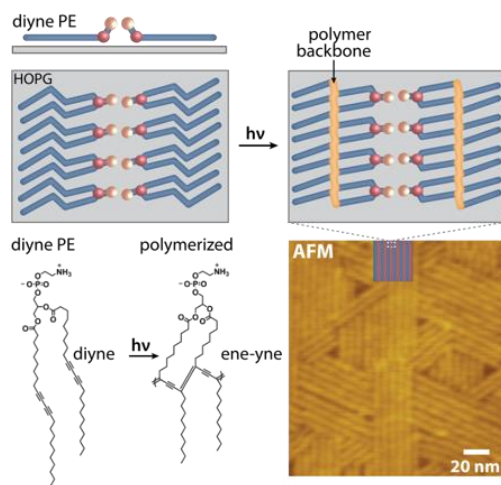
Figure 2.2.1. Illustration of diyne PE monolayer structure.

Utilization of noncovalent monolayers to control 2D material surface chemistry in scalable industrial processes such as solution- and spray-coating elevates the importance of robustness toward a range of solvents.[56, 82, 86] In most classes of monolayers, molecular desorption occurs orders of magnitude more rapidly at defects,[92-94] suggesting the importance of long-range order. Long-range molecular alignment in the monolayer also has the potential to improve function, similar to performance gains achieved in other classes of film structures through long-range structural control.[95-98]

Here, we report a process for rapidly increasing ordering in noncovalent monolayers on 2D materials. We achieve these results using a modified Langmuir–Schaefer (LS) technique that enables *in situ* thermal annealing during monolayer assembly. Molecular domains assembled with 1 minute of *in situ* annealing are much larger than those achieved with 1 hour of conventional post-assembly annealing at the same temperature (Figure 2.2). Fast annealing is advantageous from the perspective of both processing efficiency as well as limiting exposure to elevated temperatures for reactive functional molecules (e.g. the diynes utilized here) that have limited thermal stability. We find that diynoic phospholipid monolayers annealed in this way, and subsequently photopolymerized, are stable toward vigorous washing with both polar and nonpolar solvents (e.g. water, ethanol, tetrahydrofuran (THF), and toluene). This enhanced stability suggests utility in applications that require subsequent solution processing.
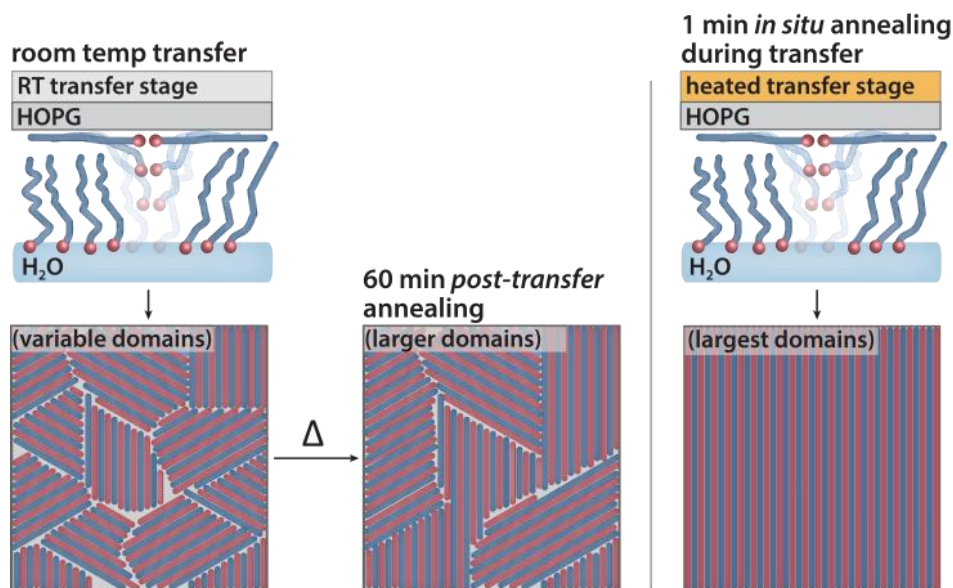
Figure 2.2. Langmuir–Schaefer conversion to create horizontally-oriented monolayer structures, at room temperature (left), with post-transfer annealing (center), and with *in situ* annealing (right).

In situ annealing leverages useful differences between LS conversion (i.e. transfer to form lying-down phases) and classical LS transfer of standing phase monolayers.[67] In both processes, a standing phase monolayer of amphiphiles is pre-assembled on an aqueous subphase, and a (usually hydrophobic) substrate is lowered onto the top of the molecular film and withdrawn, transferring molecules to the substrate. In classic LS transfer of standing phases, transferred molecules retain their original ordering; thus, transferring from tightly packed source films minimizes defects.[99-100] In contrast, in LS conversion of standing phases to lying-down phases, each molecule must rotate up to 90° from its initial orientation in the source film to form the horizontally-oriented monolayer (Figure 2.2, top left).

LS conversion has been used previously to prepare surfaces for scanning probe studies of noncovalent monolayers.[48, 55-56, 72, 86, 101-102] Typical reported domain edge lengths are on the order of ~100 nm, which does not address the need for long-range order, and transfer efficiency and ordering can be variable.[103] However, if adequate control were developed over the conversion process, it could represent a useful means of controlling monolayer structure over greater length scales.

Post-assembly thermal annealing has been used to increase ordering and decrease run-to-run variability in other monolayer chemistries, including standing phases of alkanethiols on coinage metals.[94, 104] While we have found this strategy moderately helpful in improving surface ordering in noncovalent monolayers (*vide infra*), the relatively long typical annealing times (hours) are inconvenient and can cause unwanted thermal polymerization in the diynes utilized here, creating high molecular weight polymerized rows of molecules that limit additional Ostwald ripening[105-106] to create larger domains.

To lower energetic barriers to molecular reordering, we examined the possibility of annealing *during* the initial molecular transfer and assembly process, by integrating a custom-built heated transfer stage that enables control of substrate temperature during LS conversion. We find this approach increases domain sizes and transfer uniformity, as well as robustness toward solution processing, factors that are important for many applications of noncovalently functionalized 2D materials.

2.2 Results and Discussion

2.2.1 Structure of Striped Noncovalent Monolayers

For these studies, we utilized a polymerizable amphiphile, 1,2-bis(10,12-tricosadiynoyl)-*sn*-glycero-3-phosphoethanolamine (diyne PE, Figure 2.1). Diyne PE is known to form horizontally-oriented phases on HOPG, with sub-nm headgroup ridges conducive to visualization of lamellar structure via AFM imaging.[56] In our experience, dual-chain amphiphiles exhibit greater native stability toward solvent washing than single-chain amphiphiles such as 10,12-pentacosadiynoic acid (PCDA), likely due to the additional connectivity conferred by tethering pairs of chains through phospholipid headgroups. Thus, diyne PE presents a useful test system for examining the further impacts of annealing on stability toward solution processing.

Typical results for transfer of diyne PE to a room temperature HOPG substrate are shown in Figure 2.3a; in the image shown, many narrow domains with lengths 100–1000 nm are observed. However, significant areas of the surface lack ordered domain structure. In practice, a variety of domain structures, aspect ratios, and coverage may also be observed across a single substrate (typical substrate dimensions 10 mm × 10 mm). Using samples of this type, we tested the effects of heating molecular films after the LS transfer process was completed (Figure 2.3b). After 60 minutes of post-transfer annealing at 50 °C (a temperature chosen to maximize molecular mobility while minimizing thermal polymerization), many of the narrow domains have merged, but significant vacancies remain. Although annealing somewhat improves domain ordering and size, it is also advisable to limit diyne exposure to elevated temperatures in order to minimize thermal polymerization.[107] Therefore, we examined additional possibilities for improving molecular ordering and domain size.

Postulating that increased temperatures *during* monolayer transfer might lower energetic barriers to molecular re-ordering, we compared two approaches: (1) elevating the substrate temperature prior to transfer, then allowing it to rapidly equilibrate to the aqueous subphase temperature during transfer (*fast quench*, Figure 2.3c,d) and (2) elevating the substrate temperature prior to transfer, and maintaining a setpoint temperature throughout transfer (*in situ annealing*, Figure 2.3e,f). The transfer process places the relatively small HOPG substrate (typical dimensions 1 cm × 1 cm × 1 mm) in contact with the large thermal mass of the aqueous subphase. Thus, to enable the second approach, we designed and fabricated a temperature-controlled transfer stage that was suspended from the automated dipper on a commercial Langmuir trough and utilized for

the experiments discussed below. When mounted on the transfer stage, the sample is maintained near a desired setpoint temperature by placing it in contact with an aluminum cylinder encasing a cartridge heater regulated by a PID controller.
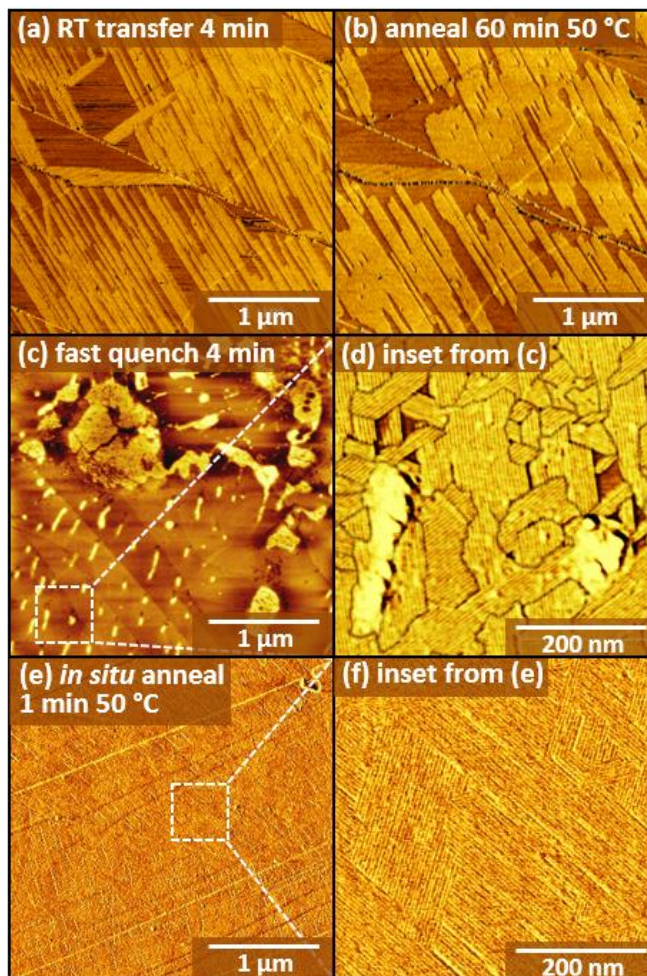
Figure 2.3. AFM images of diyne PE films. (a) Film transferred at room temperature for 4 minutes, then (b) subjected to post-transfer thermal annealing for 60 minutes at 50 °C. (c) Film transferred to an HOPG surface that was pre-heated, then allowed to cool rapidly to the subphase temperature during 1 minute LS transfer (*fast quench*). (d) High-resolution image from the area high-lighted in (c); pixels are darkened along domain boundaries as a guide to the eye. (e) Film transferred with the substrate pre-heated and held at set-point temperature of 50 °C throughout 1-minute LS transfer (*in situ* annealing). (f) High-resolution image from area shown in (e), illustrating larger domain size.

The results of fast-quench Langmuir–Schaefer conversion are shown in Figure 2.3c and d. Here, the HOPG substrate was pre-heated to 90 °C, then loaded on the standard (non-heated) dipper and slowly lowered onto the subphase; typical substrate temperatures at the time of contact

are in the range of 50–70 °C, with some variability induced by factors including HOPG thickness (which changes slightly each time the HOPG is cleaved). Transferred films contain a significant fraction of domains with curved edges (Figure 2.3c). Higher-resolution imaging reveals a mixture of lying-down phases (Figure 2.3d, striped regions) and standing phase domains (Figure 2.3d, lighter regions), presumably reflecting local molecular density variations in the subphase monolayer. In Figure 2.3d, contrast is adjusted at domain edges as a guide to the eye (see Appendix A for original image). Molecular domains assembled through fast-quench transfer are typically quite small (~60 are visible in an area with an edge length of 500 nm in Figure 2.3d), consistent with fast transfer and limited diffusion.[108] Overall, the transfer density increases by a factor of 2–3 in comparison with films transferred to a room temperature substrate.

The increased surface coverage and transfer rate observed when using the fast-quench protocol *vs.* room-temperature transfer are consistent with drying of the HOPG surface upon pre-heating (Figure 2.4). Recent evidence has pointed to a water contact angle of ~64° for freshly cleaved HOPG, which increases to values above 90° over the course of ~20 minutes in normal laboratory environments due to the adsorption of atmospheric contaminants.[109-110]
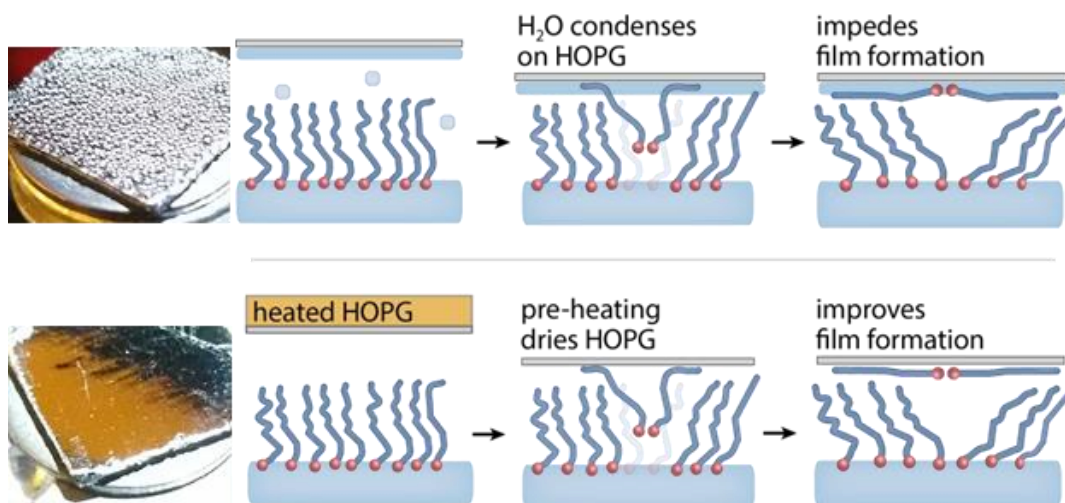
Figure 2.4. Illustration of the impact of heating HOPG surface prior to monolayer transfer. (Top) Water condensed on room temperature HOPG surface impedes film formation; (bottom) drying surface facilitates formation of alkyl–π van der Waals contacts, increasing transfer.

Freshly cleaved HOPG substrates utilized in these experiments immediately spend 1-5 minutes in the high-humidity environment above the aqueous subphase prior to contact during dipping (due to the relatively slow translation speeds of the automated dipper, used to minimize

vibrations as the dipper comes in contact with the liquid). Thus, we have observed that droplets of water can begin to condense on the surfaces of room-temperature samples prior to contact with the subphase (Figure 2.4, top left). Drying the surface would be expected to increase molecular transfer rates by facilitating formation of van der Waals contacts between alkyl chain termini and the HOPG, producing the smaller domain sizes observed.

In contrast, when the substrate is preheated to 50 °C and maintained at a setpoint temperature of 50 °C throughout transfer, full coverage and relatively large ordered lamellar domains are observed (Figure 2.3e,f), consistent with Ostwald ripening.[105, 108]

2.2.2   Examination of Transferred Domain Structure Versus Dipper Temperature

To establish an optimum temperature range for transfer and annealing to create large ordered domains, we performed a series of transfers with *in situ* annealing at setpoint temperatures from 30–90 °C. AFM images (Figure 2.5) illustrate that heating the substrate slightly above the ambient temperature increases the transfer ratio, with many small domains (<100 nm edge length). Pixels are darkened at domain edge boundaries as a guide to the eye (for larger versions of original images without pixel value adjustment, see Appendix A).

At temperatures 40 °C and below (Figure 2.5a–c), a mixture of standing phase and horizontally-oriented molecular domains is observed. Domains are fairly small, resulting in a high density of domain edges; molecules at domain edges are typically less stable and have a greater probability of desorption during solvent processing. To quantify the impact of thermal annealing on the prevalence of domain edges, we measure total line edge contour lengths per unit area (Figure 2.6), arriving at values in the range of 35–45 $\mu m/\mu m^2$ at transfer temperatures 40 °C and below. At temperatures of 50–60 °C (Figure 2.5d–e), standing phases are no longer observed, and larger ordered domains of horizontally-oriented striped phases are formed, with edge densities of ~30 $\mu m/\mu m^2$. At temperatures ≥70 °C (Figure 2.5f–h), the largest domains are observed (total edge densities ~20 $\mu m/\mu m^2$). However, at temperatures above 70 °C, the increased prevalence of small inclusion domains suggests instances of thermal polymerization.[107] Undulations along the lamellar axis may indicate thermochromic phase transitions.[111] The PID controller on the transfer stage also allows the setpoint temperature to be ramped throughout the transfer; we tested effects of raising and lowering setpoint temperature throughout transfer and did not observe substantial changes in domain structure (see Appendix A).
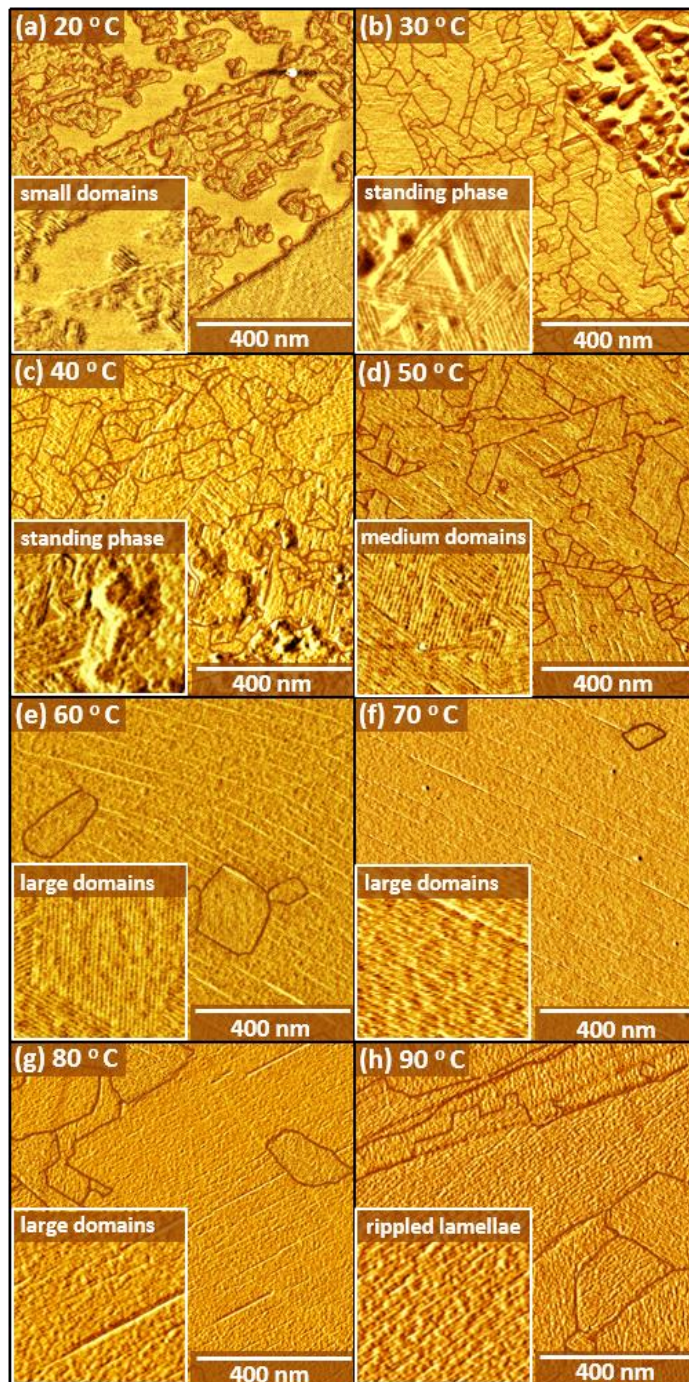
Figure 2.2.5. AFM images of diyne PE films transferred for 1 min at setpoint temperatures of (a) 20 °C, (b) 30 °C, (c) 40 °C, (d) 50 °C, (e) 60 °C, (f) 70 °C, (g) 80 °C, and (h) 90 °C, showing increased domain sizes at higher temperature. Pixels are darkened along domain boundaries to guide the eye.
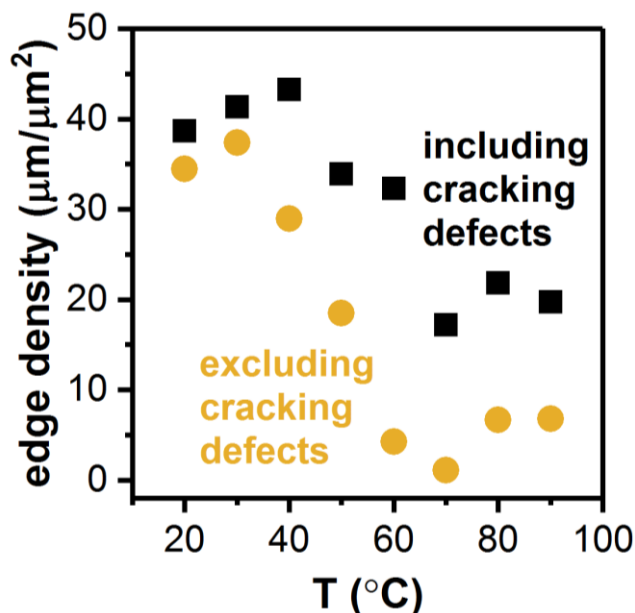
Figure 2.2.6. Domain edge contour density per μm^2 after 1-minute transfer at specified temperature.

Optimized protocols with setpoint temperatures of 70 °C (Figure 2.7) result in routine transfer of domains with edge lengths ≥10 μm (as in Figure 2.7a), substantially greater than domain sizes when room temperature substrates are utilized. In Figure 2.7a, an AFM phase image exhibits characteristic long-range molecular ordering, based on aligned monolayer features that extend from the upper left corner of the image to the lower right (edges enhanced for clarity; for original image presented at full page width, see Appendix A). Figure 2.7b shows a high-resolution AFM topography image, in which individual rows of molecules are apparent; the linear features evident in the larger phase image are visible as cracking defects parallel to the monolayer lamellar axis. Such features are consistent with conformational changes that occur during polymerization as the internal diyne rehybridizes to form the ene-yne polymer backbone; molecular models (Figure 2.7c) indicate that lamellae narrow by ~0.2 nm during polymerization.

In AFM images with long-range ordering, cracks with widths of 2–5 nm occur with a periodicity of 50–100 nm, suggesting a high degree of polymerization. Previous studies of solid-state polymerization of smaller diynes (e.g. diacetylene-*bis*(toluenesulfonate)) have demonstrated a reaction rate increase of over 2 orders of magnitude when the material reaches ~10–20% conversion, due to strain accrual based on the difference between monomer and polymer lattice parameters.[112-113] We have not routinely observed cracking defects in the smaller domains formed

through room-temperature transfer, and it is possible that one of the impacts of *in situ* thermal annealing is to increase molecular alignment in ways that improve polymerization efficiency.
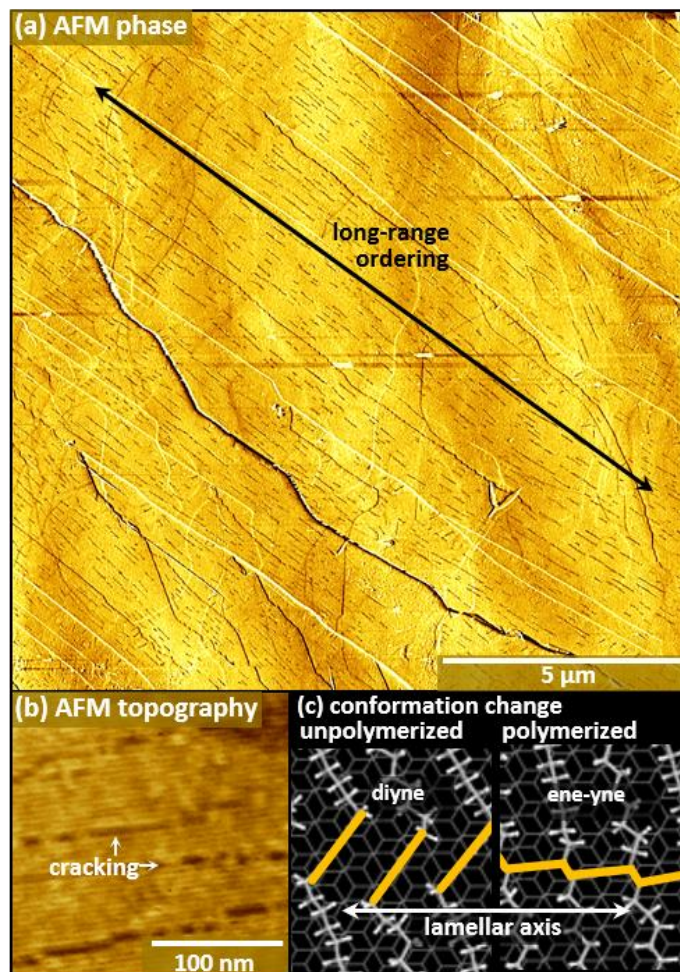
Figure 2.2.7. AFM images of long-range ordering. (a) Representative phase image illustrating molecular ordering over multiple µm, including over step edges in HOPG. Pixels are darkened along cracking defects as a guide to the eye. (b) Topography image illustrating cracks formed in diyne PE monolayer during polymerization. (c) Molecular models of change in diyne PE monolayer structure during polymerization, leading to cracking defects visible in (a–b).

Polymerization-induced cracking results in a relatively high lower bound on line edge density (~20 µm/µm^2), even in areas with a high degree of molecular alignment. Figure 2.6 shows scatter plots of line edge densities both including (black markers) and excluding (gold markers) polymerization-induced crack defects, for comparison. However, polymerized edge sites likely represent a lower etching probability than disordered sites at the edges of small, kinetically trapped domains formed at low temperature.

Although we tested transfer times as long as 30 minutes (see Appendix A), most ordering appears to occur within the first minute, and a more significant contributor to domain extent appears to be the size of terraces in the HOPG substrate. Step edges commonly represent nucleation points for domain growth; in some cases, this has the effect of promoting domain alignment across step edges. Within large domains, we occasionally observe smaller domains with alternate epitaxial alignment, even at relatively long equilibration times, again consistent with early polymerization events that preclude completion of domain alignment during long annealing periods.

Because one of the goals of controlling molecular alignment over significant length scales is to improve robustness toward solution processing, we conducted a series of solvent washing assays using solvents with varying dielectric constants (ε) and surface tensions (γ) (Figure 2.8).[114] Samples were washed vigorously for a total of 30 seconds with a stream of water ($\varepsilon = 80.1$, $\gamma = 72.4$ mN/m), ethanol ($\varepsilon = 24.5$, $\gamma = 22$ mN/m), THF ($\varepsilon = 7.58$, $\gamma = 26.4$ mN/m), or toluene ($\varepsilon = 2.35$, $\gamma = 28.4$ mN/m), then blown dry with nitrogen. After washing with water (Figure 2.8a,b) or toluene (Figure 2.8g,h), which are not good solvents for the monomeric phospholipid, the final surface coverage is essentially the same as the initial coverage prior to washing (see Appendix A for pre-washing images). When samples are washed with ethanol (Figure 2.8c,d) or THF (Figure 2.8e,f), domains edges are eroded for samples transferred at room temperature (Figure 2.8c,e), while annealed samples with large domains (Figure 2.8d,f) again retain essentially complete coverage; cracking defects visible prior to washing are not substantially enlarged, consistent with polymerization of molecular rows on both edges of the crack.

Figure 2.9 quantifies the relationships between molecular removal and annealing illustrated in the AFM images in Figure 2.8. Overall, we find that solvents with an intermediate dielectric, which are reasonable solvents for the monomer (e.g. ethanol, THF), remove 10–20% of the molecules from non-annealed monolayers (Figure 2.9, left), but ≤2% of the molecules from annealed monolayers. This finding demonstrates that *in situ* annealing is an effective strategy for further stabilizing the interface toward solution processing.

Because receding solvent fronts can remove molecules from a surface in order to minimize their surface energy, we also examined the relationship between solvent surface tension and molecular removal. However, for the system investigated here, molecular removal does not appear

to be correlated with surface tension (Figure 2.9, right); both the most strongly etching solvent (ethanol) and weakly etching solvent (toluene) have approximately the same surface tension values.
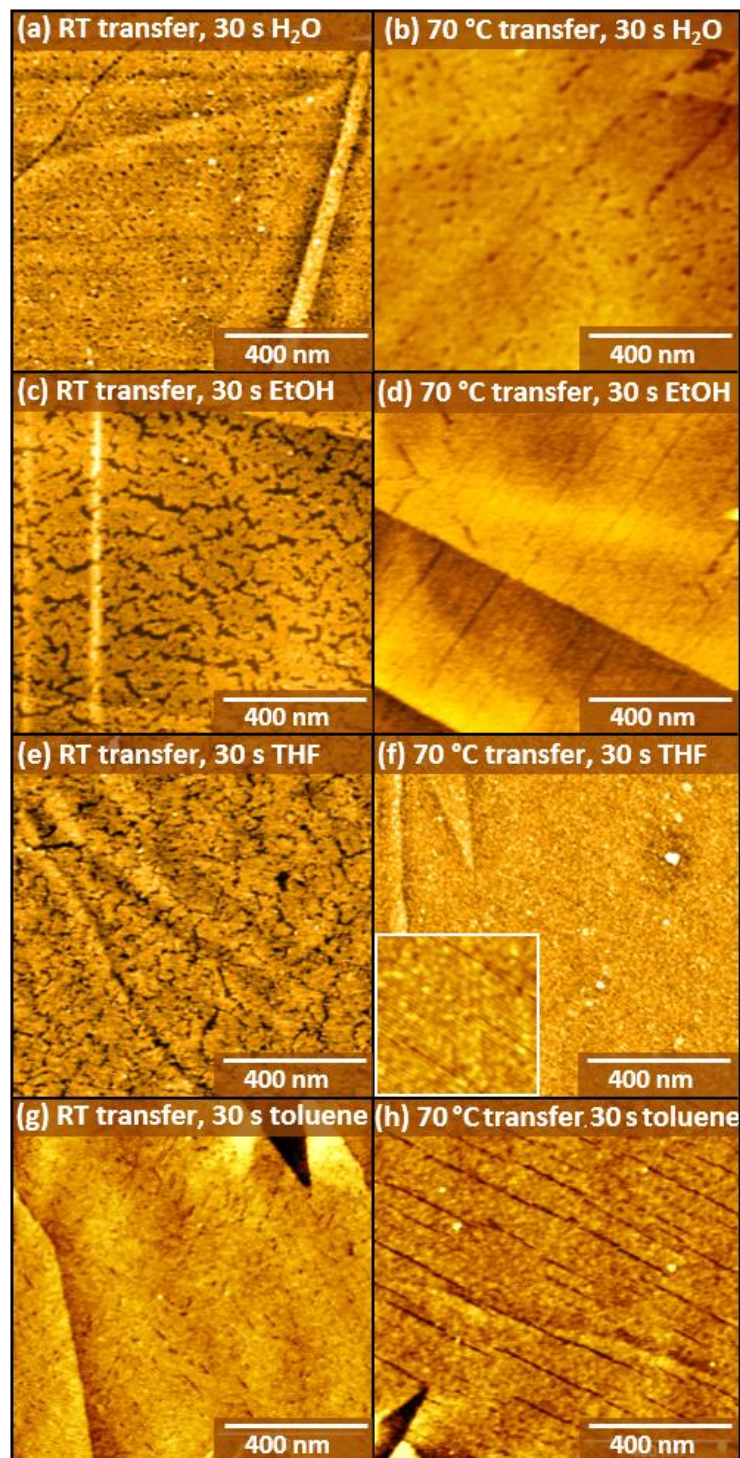
Figure 2.2.8. AFM images of diyne PE films after 30 s of vigorous washing with deionized water (a,b), ethanol (c,d), THF (e,f), and toluene (g,h).
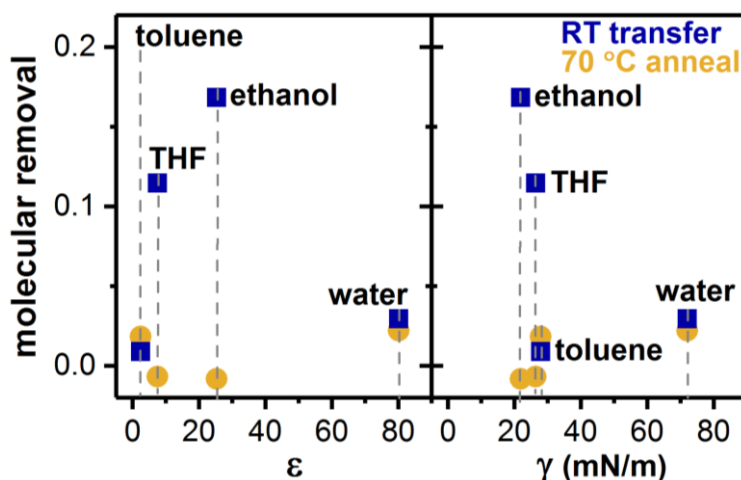
Figure 2.2.9. Molecular removal from annealed (gold) and room temperature (blue) transferred monolayers vs. dielectric constant (ε, left) and surface tension (γ, right) of the washing solvent. Small negative values at two data points above result from backfilling of vacancies during washing.

2.3 Conclusion

We have shown that controlling substrate temperature during Langmuir–Schaefer conversion of a standing phase to a lying down phase can substantially increase both the extent of transfer and the size of ordered domains in noncovalent monolayers on 2D materials. This increased order is achieved in typical *in situ* annealing times of 1−5 min, in contrast with more limited results achieved with an hour or more of conventional post-transfer annealing at the same temperature. Further, we find that monolayers of diynoic phospholipids transferred through this *in situ* thermal annealing process and subsequently polymerized exhibit enhanced stability toward vigorous washing with a range of polar and nonpolar solvents. Together these capabilities represent an important advance in the use of noncovalent monolayer chemistries to control 2D material surfaces in solution processing environments commonly used in device preparation.

2.4 Experimental Methods

2.4.1 Materials

Chloroform (Sigma-Aldrich, St. Louis, MO, ≥99% purity), tetrahydrofuran (Sigma-Aldrich, St. Louis, MO, anhydrous inhibitor-free, ≥99.9% purity), absolute ethanol (Decon Labs, Inc., King of Prussia, PA, 100% purity), toluene (Fisher Scientific, Pittsburgh, PA, 99.9% purity), and manganese(II) chloride tetrahydrate (Sigma-Aldrich, St. Louis, MO,

≥98% dry basis) were used as received from their corresponding manufacturers. 1,2-bis(10,12-tricosadiynoyl)-*sn*-glycerol-3-phosphoethanolamine (diyne PE) (>99.0% purity) was purchased from Avanti Polar Lipids (Alabaster, AL). Highly oriented pyrolytic graphite (HOPG) substrates, grade ZYB, were purchased from MikroMasch (Watsonville, CA). Milli-Q water (≥18.2 MΩ·cm resistivity) was used in all experiments. Ultra-high purity nitrogen was purchased from Indiana Oxygen Company (Indianapolis, IN, 99.999% purity). PELCO conductive liquid silver paint, standard SEM pin stub mounts, and double coated carbon conductive tape were purchased from Ted Pella, Inc. (Redding, CA).

2.4.2 Instrumentation

Atomic force micrographs were acquired using a Veeco MultiMode AFM with NanoScope V controller (Bruker Instruments, Billerica, MA) or an Asylum Cypher ES AFM (Oxford Instruments, Santa Barbara, CA). Self-assembled monolayers of diynoic phospholipids were prepared on a Langmuir–Blodgett trough from either KSV-NIMA (Biolin Scientific, Stockholm, Sweden) or Kibron (Helsinki, Finland).

2.4.3 Design and Use of Heated Dipper

To enable temperature-controlled LS transfer, a temperature-controlled transfer stage was fabricated for integration with the automated dipper on a commercial Langmuir trough. The transfer stage comprises an aluminum cylinder with an embedded cartridge heater regulated by a PID controller. Samples are mounted on the cylinder utilizing standard 12 mm diameter high quality magnetic stainless-steel AFM specimen discs (alloy 430, Ted Pella, Inc.) that mount on a magnet recessed in the body of the cylinder. To maximize temperature uniformity across the HOPG surface, a thin film of silver conductive epoxy (H20E Epo-Tek, Ted Pella, Inc.) was used to affix the back of the HOPG substrate to the specimen disc surface; epoxy curing was carried out at 80 °C for 3 hours.

2.4.4 Langmuir–Schaefer Conversion of Diynoic Phospholipids

Self-assembled monolayers of diyne PE were prepared via LS transfer on a KSV-NIMA or Kibron Langmuir–Blodgett trough. All sample handling steps were performed under

UV-filtered light to minimize photopolymerization. Prior to depositing the lipid solution on the subphase, the subphase was heated to 30 °C using a Beckman GeneLine Cooler and held at this temperature throughout the LS deposition. LS transfer of diynoic phospholipids was carried out by spreading 30 µL of 0.50 mg/mL diyne PE in $CHCl_3$ on a subphase of 5 mM $MnCl_2$ in Milli-Q water, with 1-µL droplets of the lipid solution spaced evenly in a grid across the subphase to increase source film uniformity.

The trough was allowed to equilibrate for 30 minutes in order for the $CHCl_3$ used in phospholipid deposition to evaporate. Subsequently trough barriers were swept inward (6.23 mm/min each barrier) to adjust the surface pressure. When the surface pressure reached 30 mN/m, an automated dipper attachment on the LB trough was utilized to lower a freshly cleaved HOPG substrate onto the subphase (dip rate = 6 mm/min) with the cleaved surface facing down. The HOPG was freshly cleaved immediately prior to lowering onto the subphase. In some experiments, the standard dipper was utilized, whereas in others, the heated dipper attachment was added to enable control over substrate temperature, as specified in the manuscript text.

When the heated dipper attachment was utilized, the HOPG surface temperature was recorded using an Analogic Digi-Cal II thermocouple calibrator, model AN6520, placed in direct contact with the surface of the substrate, just before cleaving the HOPG. After the specified amount of time in contact with the subphase (typically 1–4 minutes), the HOPG was gently lifted out of contact with the subphase using the automated dipper. Surface temperature measurements immediately after transfer, as the HOPG is lifted out of contact with the subphase, indicate that the substrate is within 2 °C of the setpoint at 50 °C, and within 5 °C of the setpoint at 90 °C. We anticipate that tighter regulation of the sample temperature at high setpoint values may be possible through further optimization of the placement of the embedded thermocouple and cartridge heater. Diacetylene-functionalized amphiphile samples prepared using the described procedure were photopolymerized by 1 hour of irradiation under a 254-nm, 8 W, UV lamp with approximately 4 cm between the lamp and the sample surface.

2.4.5 Solvent Washing

In all four of the solvent washing assays (water, ethanol, THF, and toluene) the diyne PE monolayers were subjected to a vigorous stream of solvent from an appropriate wash bottle or glass syringe in 5-second intervals. Immediately following each solvent wash, the sample was

blown dry with ultra-high purity nitrogen. This process was repeated up to 6 times (30 seconds total solvent contact time with sample) with AFM imaging performed at the same locations after each wash cycle.

2.4.6   AFM Imaging

All standard AFM measurements were performed using a Veeco MultiMode (Bruker Instruments, Billerica, MA) instrument in tapping mode with 0.01–0.025 Ohm·cm Antimony (n)-doped Si Bruker RFESP-75 tips (nominal force constant 3 N/m and radius of curvature <12 nm). Imaging of the dry thermal annealing process was performed using an Asylum Cypher ES (Oxford Instruments, Santa Barbara, CA) instrument with an integrated heating/cooling sample stage. After initial imaging, the sample stage was heated to 50 °C for 1 h before being cooled to 25 °C for the final measurements. Imaging was performed in tapping mode using 0.01–0.025 Ohm·cm Antimony (n) doped Si Mikromasch HQ:NSC tips (nominal force constant 3 N/m and radius of curvature <12 nm).

2.4.7   Molecular Modeling

Software packages Maestro and Macromodel (Schrödinger, Cambridge, MA) were used, respectively, to visualize the structures of diynoic phospholipids on graphene and to perform force field minimizations. All models were simulated using the OPLS_2005 force field, with no solvent file and extended cutoffs for van der Waals, electrostatic, and hydrogen-bonding interactions. Minimizations were performed using the Polak-Ribiere conjugate gradient (PRCG) algorithm and gradient method with 50,000 runs and a convergence threshold of 0.05. Most minimizations converged in less than 10,000 runs. For all calculations, atoms in the graphene sheets were frozen, in order to more closely mimic the structure of HOPG. Thus, while they contributed to the forces present in the system, their positions did not change in response to conformational changes of the adsorbed phospholipids.

CHAPTER 3. LARGE-SCALE NONCOVALENT FUNCTIONALIZATION OF 2D MATERIALS THROUGH THERMALLY CONTROLLED ROTARY LANGMUIR-SCHAEFER CONVERSION

Introduction

Advances in nanoscale electronics,[21, 30] photovoltaics[31-32] and biosensors[33-34] incorporating 2D hybrid materials have elevated the demand for scalable processes that can control the surface chemistry of 2D materials such as graphene,[35-36] highly oriented pyrolytic graphite (HOPG),[56, 69, 86] transition metal dichalcogenides (e.g., MoS_2, WS_2),[37, 70, 115] and black phosphorous[38, 115] over large areas. In order to preserve the extended electronic delocalization networks intrinsic to the basal plane of 2D materials, noncovalent functionalization with organic molecules[35, 37-42] or inorganic nanoparticles[43-44] is often leveraged to modulate 2D material physical properties.

Noncovalent functionalization of 2D materials can be achieved *via* several methods, including drop-casting from organic solvents,[48, 58-59] flow-induced wicking,[60-61] solution-shearing,[62] and deposition from Langmuir films.[56, 63-64, 116] While drop-casting from organic solvent is experimentally expedient for assembly over small areas, significant challenges arise in controlling solvent drying and other processes that can lead to heterogeneity in assembled structures over larger areas. Modified drop-casting methods (*e.g.* flow-induced wicking, solution-shearing) that control solvent flow near the substrate can promote long-range ordering for molecules such as polyaromatic hydrocarbons on HOPG.[60-62] However, for many other classes of important functional molecules, such as long-chain amphiphiles, substantial challenges arise in generating long-range molecular ordering, or ordering over large areas of 2D substrates, using solution processing techniques. Langmuir transfer techniques can enable long-range ordering of amphiphilic molecules on solid substrates through the preordering of molecular films on an aqueous subphase prior to transfer.[64, 68, 117] Langmuir–Blodgett, LB, transfer (substrate is oriented perpendicular to the Langmuir film, and drawn vertically through it)[65-66] and Langmuir–Schaefer, LS, transfer (substrate is oriented parallel to the Langmuir film, and lowered into contact, then withdrawn)[67] have both been broadly utilized for ordering and patterning of standing phase

molecular films.[64, 68] LS transfer has also been shown by our group[56-57, 69-70] and others[54, 71-72, 116] to be useful in functionalizing 2D materials through the conversion of standing phase Langmuir films to ordered lying-down phases on 2D substrates, a process we refer to as LS conversion.

Most classical approaches to both LB and LS transfer seek to strictly maintain the initial molecular ordering in the Langmuir film by transferring segments of the standing phase film directly to the receiving substrate. However, for LS conversion, the film undergoes a fundamental reordering, from standing phase at the air–water interface to lying-down phase on the receiving substrate (Figure 3.1a). This difference creates new opportunities to manipulate the transfer process to generate long-range order, and to increase functionalized surface area. Recently, we developed a heated transfer stage to control substrate temperature during LS conversion.[117] Thermally controlled transfer enabled assembly of noncovalent molecular domains of diyne phospholipids with edge lengths at least an order of magnitude larger than those assembled through room temperature LS conversion, with full coverage transfer in as little as 1 min. Monolayers transferred in this way exhibited increased robustness toward subsequent solution processing in solvents with a range of polarities, in comparison with those transferred at room temperature.[117]

A longstanding barrier to the broad use of Langmuir transfer methods has been limited throughput, due to the serial nature of transfer and limit on practical trough sizes.[118] Drawing inspiration from roll-to-roll processing techniques used industrially, a few accounts have recently reported LB transfer of nanoparticles from an air-liquid interface across large substrate films.[119-121]

LS conversion has the potential to be an especially good candidate for roll-to-roll processing, since the translation of the receiving substrate across the Langmuir film (Figure 3.1a) can in principle contribute to the reordering required to form the lying-down phase. In this work, we designed and built a thermally controlled rotary transfer stage to examine possible contributors to successful roll-to-roll LS conversion (Figure 3.1a). The thermally regulated rotary transfer stage enables large-area noncovalent functionalization of 2D materials with lying-down striped phases (~6 nm periodicity) of amphiphiles (here, photopolymerizable phospholipids), achieving ordered domain sizes up to nearly 10,000 µm². We demonstrate utility of these large-area functional patterns in a subsequent rotary transfer process, assembling ultranarrow gold nanowires (AuNWs) with core diameters <2 nm and average lengths of 300–500 nm (Figure 3.1b).

(a) scalable surface functionalization via thermally controlled rotary Langmuir–Schaefer conversion
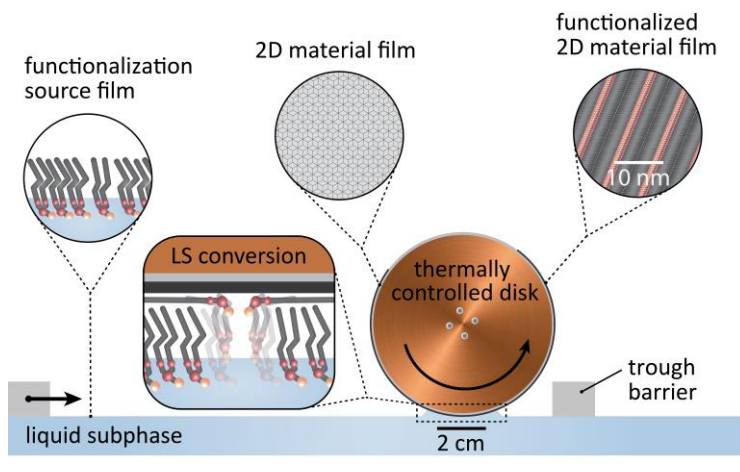
(b) sequential surface functionalization
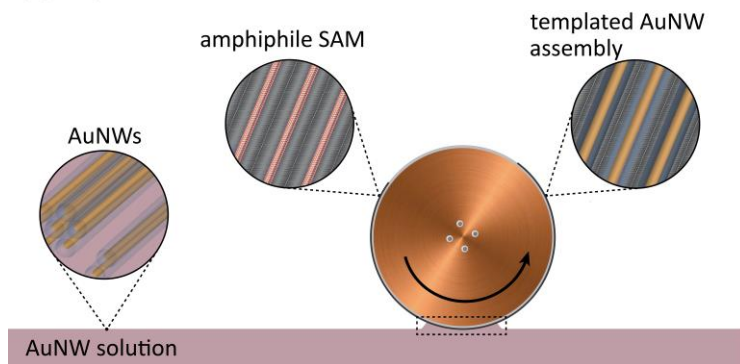
Figure 3.1. (a) Illustration of thermally controlled rotary Langmuir–Schaefer conversion to create nm-resolution chemical patterns exhibiting long-range order. (b) Illustration of sequential rotary transfer to utilize nm-resolution surface templates for further surface functionalization (here, assembly of gold nanowires (AuNWs)).

3.1 Results and Discussion

3.1.1 Noncovalent Functionalization of HOPG with Diyne Phospholipids via Thermally Controlled Rotary LS Conversion

To prototype an LS conversion protocol readily extensible to roll-to-roll transfer, we designed a copper disk with four embedded cartridge heaters and a type K thermocouple (Figure 3.2 and Appendix B Figure S.B.1). The disk was mounted on a translator that allowed it to be lowered into contact with the aqueous subphase, as shown in Figure 3.2a. When in contact, the subphase forms a meniscus at the base of the disk (Figure 3.2b (right) and 3.2d). In order to promote a consistent meniscus shape between thermally controlled rotary LS conversion

37

experiments, the bottom of the disk was submerged ~1 mm into the subphase, so that ~33 mm of the perimeter resides between the advancing and receding fronts of the meniscus during disk rotation.
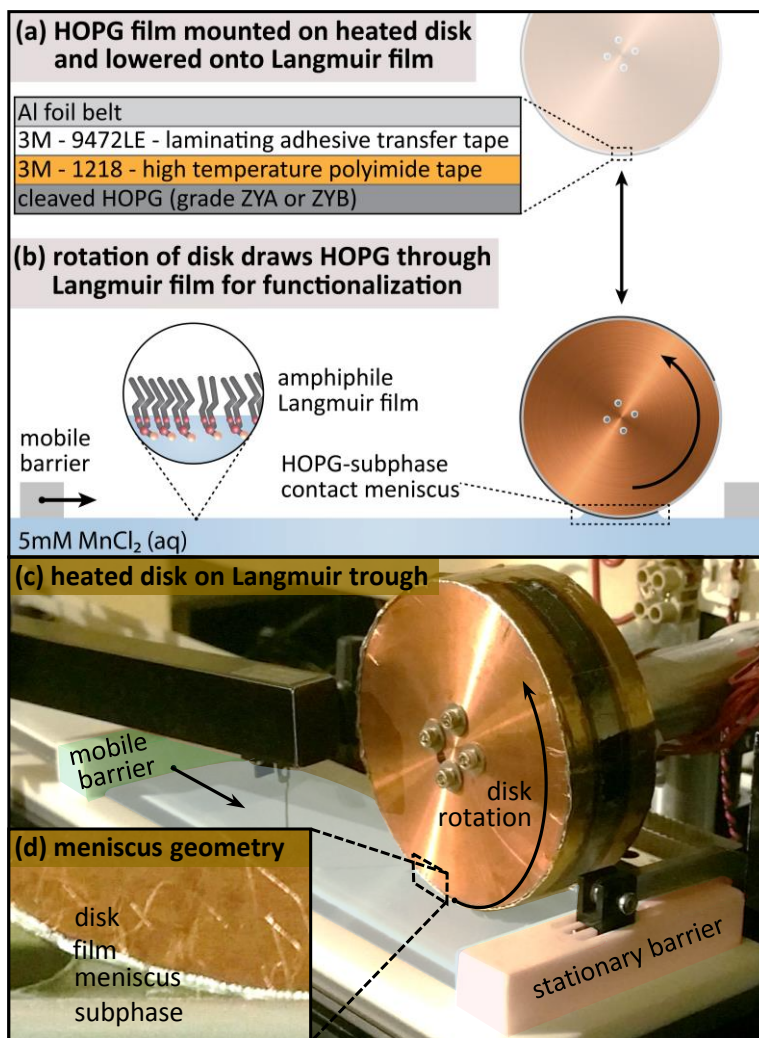
Figure 3.2. (a-b) Schematic of heated copper disk with film of HOPG mounted during transfer. (c) Image of thermally controlled rotary transfer stage positioned over trough, illustrating single barrier compression geometry. (d) Detail of HOPG–subphase contact meniscus.

We have previously shown thermally controlled LS conversion of polymerizable amphiphiles can be achieved on HOPG, MoS_2 and CVD graphene on nickel substrates.[70, 117, 122] For all experiments here, thin films of HOPG cleaved from a bulk substrate were leveraged to create long pliant HOPG films as inexpensive analogues to CVD graphene sheets. The HOPG films were prepared by repeatedly cleaving an HOPG substrate with high temperature polyimide

tape; each HOPG tape cleavage was then adhered face up onto a strip of double-sided laminating adhesive tape atop an aluminum foil belt. Subsequently, the belt was mounted firmly around the periphery of the copper disk for noncovalent functionalization (Figure 3.2a-c and Appendix B Figure S.B.2). More details on film preparation can be found in the Experimental Methods section.

In this study, striped phases of the photopolymerizable amphiphile 1,2-bis(10,12-tricosadiynoyl)-*sn*-glycero-3-phosphoethanolamine (diyne PE, Figure 3.3) were prepared using the new rotary translation stage under LS conversion conditions previously reported by our group,[56, 117] in a transfer process we refer to as thermally controlled rotary LS conversion (TCR–LS conversion). For all TCR–LS conversions of diyne PE to HOPG films performed in this manuscript, the temperature of the HOPG surface was maintained at 80 ± 3 °C; the setpoint temperature was chosen based on results achieved previously utilizing a non-rotary thermally controlled LS conversion stage.[117] The elevated temperature promotes long-range ordering of assembled molecular domains, and nearly complete monolayer surface coverage of striped phases, which in our experience results in minimal retention of subphase as the trailing edge of the HOPG film emerges from the receding front of the meniscus.

Since the motion of the thermally controlled disk is directional in TCR–LS conversion (here, counterclockwise, Figure 3.2b), transfers were carried out in a single-barrier compression geometry (Figure 3.2c, mobile barrier is false-colored green; stationary barrier false-colored red). To assess whether the LS conversion process is impacted (*e.g.* monolayer surface coverage, relative domain sizes) by the translation rate of the HOPG belt across the amphiphile source film, substrate film translation rates of 1.10 mm/s, 0.54 mm/s, and 0.14 mm/s were tested.

As observed previously with the non-rotary thermally controlled transfer stage,[117] standing phases of diyne PE assembled on an aqueous subphase can be transferred to form noncovalently adsorbed lying-down striped phases on the HOPG belt using TCR–LS conversion. Molecular models in Figure 3.3a and 3.3b illustrate the lamellar structure of diyne PE on HOPG, both before (Figure 3.3a) and after (Figure 3.3b) photopolymerization. Atomic force microscopy (AFM) images show lamellar periodicity of unpolymerized TCR–LS converted diyne PE on HOPG (Figure 3.3c). Larger-scale AFM images (Figure 3.3d) illustrate pre-polymerization diyne PE domain structure; domains orient in epitaxy with the hexagonal HOPG lattice (black arrows), resulting in ~120° angles between domains. At μm scales, topographic features on the HOPG

surface begin to obscure features in the monolayer structure, since the 0.34 nm thickness of each HOPG layer is similar to the thickness of the monolayer.
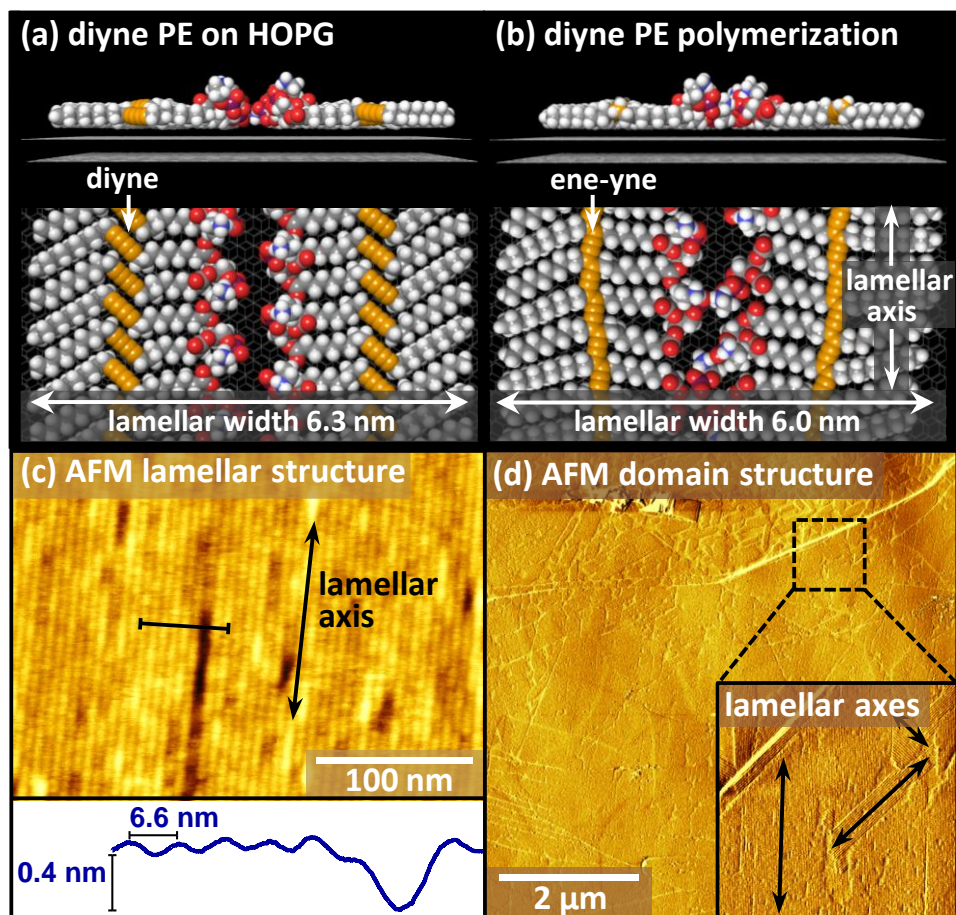
Figure 3.3. (a-b) Molecular models of diyne PE lamellar phase assembled on HOPG (a) prior to and (b) following photopolymerization. (c) AFM image illustrating lamellar periodicity of unpolymerized diyne PE film. (d) Larger-scale AFM image (phase), illustrating unpolymerized lamellar phase domains oriented epitaxially with hexagonal HOPG lattice (black arrows).

Previously, we have found that it is possible to resolve structural details of these monolayers by scanning electron microscopy (SEM),[63, 122-124] based on a combination of large contrast differences between the thin (<1 nm), predominantly insulating monolayer, and the more conductive HOPG substrate. The presence of polymerization-induced cracking defects[63] serve to highlight the lamellar row orientation (Figure 3.4a,b). Here, SEM images in Figure 3.4b and 3.4c show monolayer diyne PE domains at a scale comparable to the AFM image in Figure 3.3d, to highlight the similar information that can be derived regarding both molecular domain structure

and surface coverage. Throughout the rest of the manuscript, characterization is based primarily on large-area SEM images.

3.1.2 Comparison of Surface Coverage and Molecular Domain Morphologies Based on Stage Translation Rate

The rotation rate of the transfer stage determines both the length of time each point on the HOPG surface spends in contact with the Langmuir film, as well as the rate of translation of the HOPG surface through the leading edge of the meniscus bearing the Langmuir film (Figure 3.2d). To examine whether either of these factors contributed to domain ordering, we tested a range of rotation rates chosen to produce substrate translation rates of 0.14–1.10 mm/s, equivalent to HOPG–Langmuir film contact times of 4 min to 30 s. Contact time is calculated as the time required for a point on the disk surface to travel between the leading and trailing edges of the HOPG–subphase meniscus. Functionalization was examined in evenly spaced testing zones with x coordinates from 10–20 mm (in the first segment of HOPG to contact the Langmuir film as the disk is lowered) to 130–140 mm. For all tested translation rates, we observed nearly complete surface coverage of striped phases (>95%) in regions up to 80 mm along the HOPG strip (Figure 3.4d). In the last two test regions (100–110 mm and 130–140 mm), the slowest translation rate (0.14 mm/s) maintained nearly complete surface coverage (>98%); however, there appears to be a threshold speed between 0.14-0.54 mm/s at which surface coverage begins to decrease. This finding may be consistent with a limited rate at which the Langmuir film can restructure to refill the area of the film depleted by the transfer stage.

Both stage translation rate and linear position along the transfer path impacted the distribution of molecular domain sizes (Figure 3.5). Measured domain sizes varied by several orders of magnitude, from <0.01 μm^2 to >8000 μm^2, frequently requiring manual image segmentation to detect domain edges. To quantify the extent of molecular ordering observed at points along the transfer path, we segmented contiguous blocks of 100 domains in each of three representative SEM images selected from three discretely spaced locations within each of the five testing zones along the transfer path. For each HOPG translation speed (0.14 mm/s (left), 0.54 mm/s (center), 1.10 mm/s (right)), this generated a set of 300 domain areas. Each set is represented in two ways in Figure 3.5 — first, as a fraction of the total surface area occupied by domains in a given size range (gold bars), and second, as a histogram of the frequency with which

domains in a given size range were observed (blue bars). As a guide to the eye, 1 μm^2 and 100 μm^2 areas are indicated by a pair of dotted lines in each histogram. Calculated mean values for each test region were often very different from median values, and had large associated standard deviations, consistent with skewed distributions. The median absolute deviation (MAD, the interval from the 25th –75th percentile of the distribution), is a measure of dispersion of data that is insensitive to outliers,[125] and therefore, was utilized to describe the median domain size distributions in Figure 3.6a.
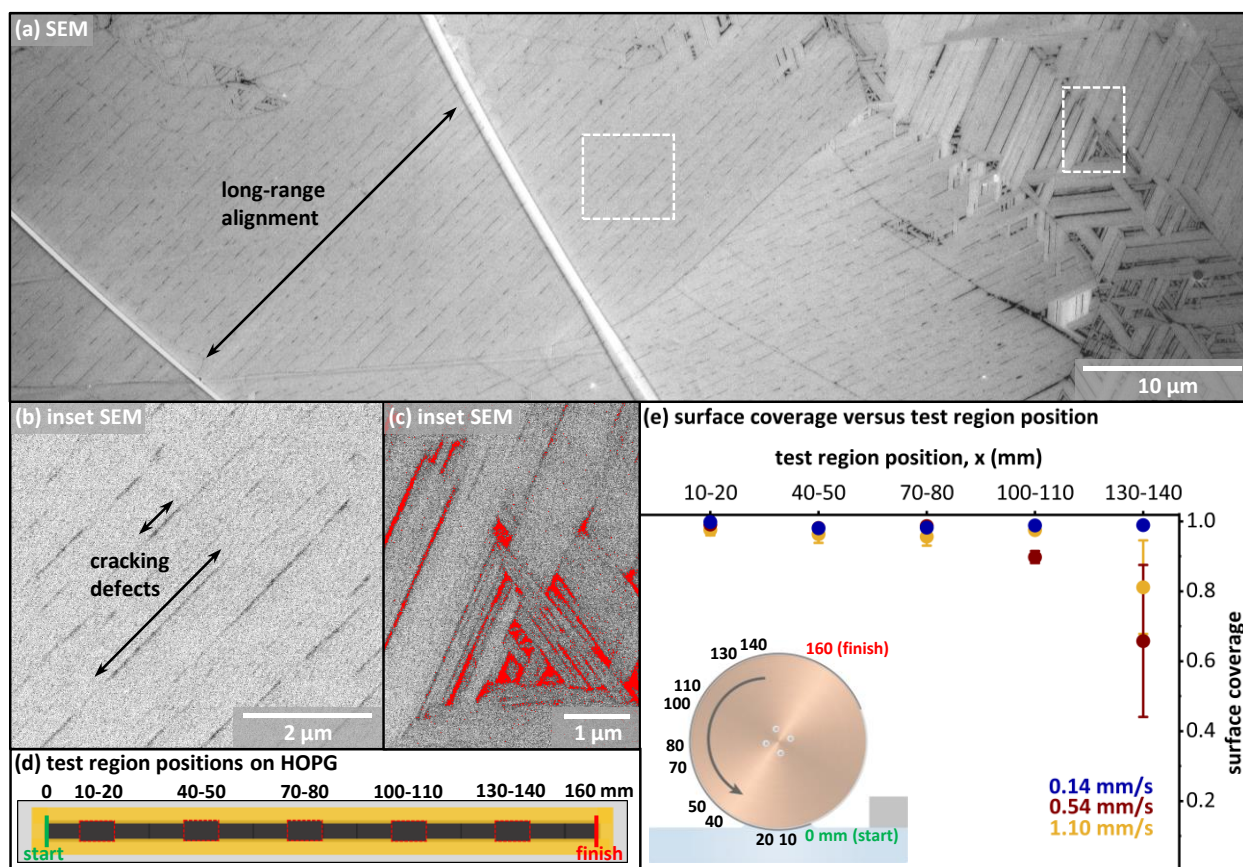
Figure 3.4. (a-c) SEM images illustrating quantification of surface coverage for diyne PE on HOPG. (b) and (c) are enlargements of areas in (a) highlighted with white boxes. (b) shows a subset of an area in (a) exhibiting long range molecular alignment. In (c), red masking highlights vacancies used to calculate surface coverage for images at scale shown in (a). (d) Illustration of the five test zones along the flexible HOPG substrate film (red dashed boxes). (e) Quantification of surface coverage along HOPG films for the three tested stage translation rates (0.14 mm/s (blue), 0.54 mm/s (red) and 1.10 mm/s (gold).
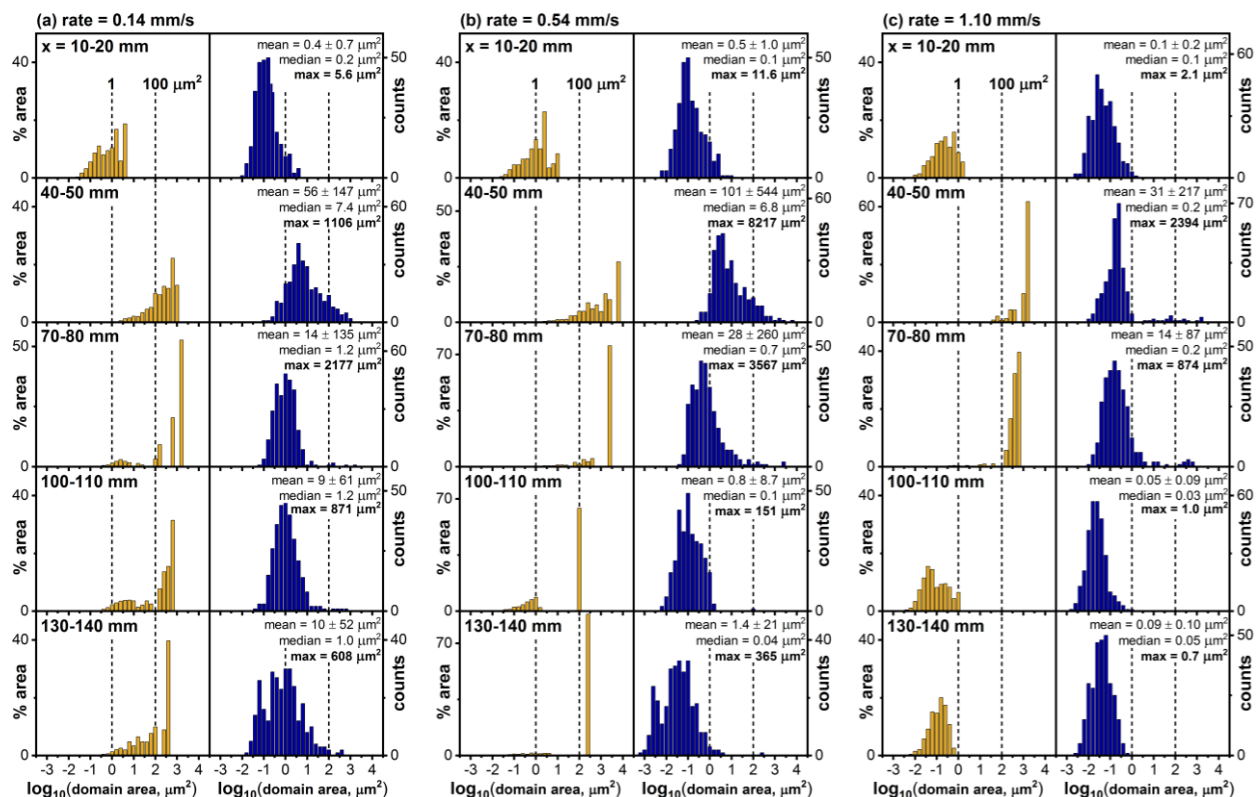
Figure 3.5. Histograms of quantified molecular domain sizes for HOPG translation rates of: (a) 0.14 mm/s, (b) 0.54 mm/s, and (c) 1.10 mm/s. Each set of measurements is presented as counts (blue bars), and as % measured area occupied by domains of that size (gold bars).

Median (Figure 3.6a) and maximum (Figure 3.6b) observed domain sizes suggest substantial advantages associated with translation of the stage during transfer. The first test zone (10–20 mm) is in the region lowered into contact with the Langmuir film. Small median domain sizes (0.1–0.2 μm^2) were observed for all three translation rates in the 10–20 mm test zone, with maximum observed individual domain areas 2.1–11.6 μm^2. Regions of the HOPG film brought into contact with the Langmuir film through rotation of the transfer stage (x = 30–140 mm) primarily exhibited much larger molecular domains (median domain areas up to 7.4 μm^2), with domain sizes >100 μm^2 routinely observed, and occasional domains with areas approaching 10,000 μm^2. In most cases, domains were largest for x = 40–50 mm (the first translated test region) and decreased in later test zones along the transfer path.

Maximum domain areas (Figure 3.6b) were typically orders of magnitude greater than the median values, and did not exhibit a clear dependence on translation rate. While median domain sizes exhibited some correlation with translation rate (larger domains associated with slower

translation), all three translation rates produced similar maximum domain sizes for x = 40–50 mm and 70–80 mm, with similar sizes for slow (0.14 mm/s) and medium (0.54 mm/s) transfer rates through the end of the test strip (140 mm). Since the sizes of large domains do not correlate strongly with either median domain size or surface translation rate, we suggest that very large ordered molecular domains on HOPG may arise through transfer of molecules *from* large ordered molecular domains in the Langmuir film. This possibility could also be consistent with observed morphological features of large ordered domains of diyne PE on HOPG. For instance, in the large ordered area of diyne PE that occupies much of the SEM image in Figure 3.4a, molecular ordering extends across several step edges, including at least two that are tall enough to cause significant electron scattering (bright features running from upper left to lower right), and across two sets of HOPG terraces with a rotational offset (rotational offset boundary extends from upper left to lower right, in the ordered area).
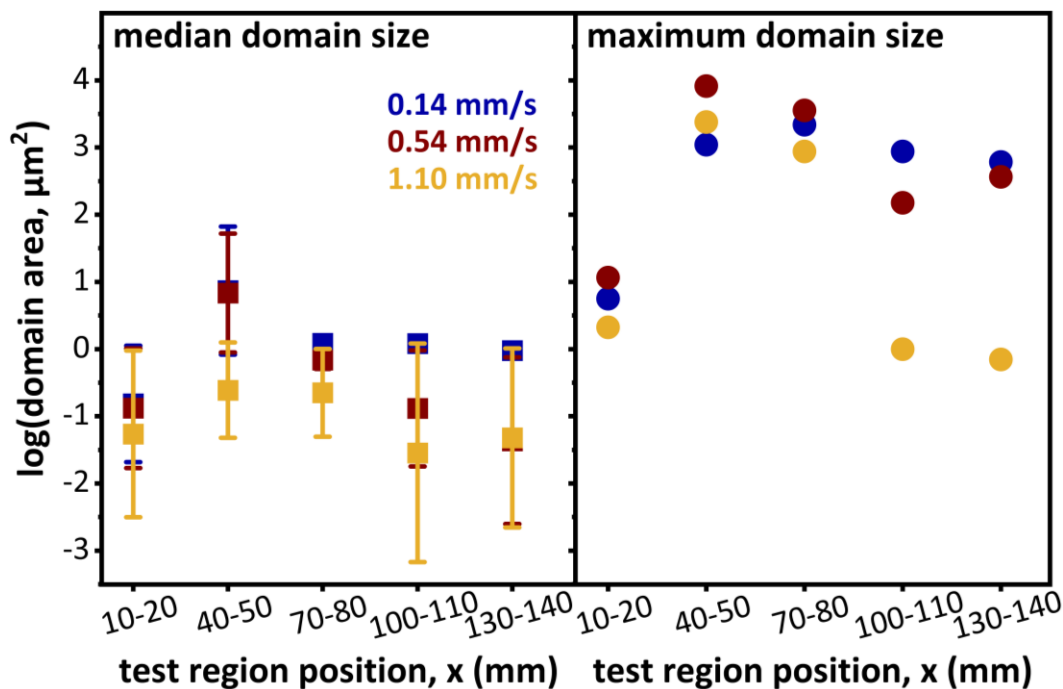
Figure 3.6. (a) Median and (b) maximum domain sizes tabulated for stage translation rates of 0.14 mm/s (blue), 0.54 mm/s (red), and 1.10 mm/s (gold). Median domain sizes along film are reported with calculated median absolute deviations.

Overall, the surface coverage and molecular domain size analyses indicate high degrees of coverage for all tested translation rates. However, for applications in which surface coverage must

be very near 100%, or that benefit from uniformly larger ordered domains (as evidenced by small MAD values near the end of the HOPG film), slow translation rates (here, 0.14 mm/s) may be beneficial.

3.1.3 Sequential Rotary Transfer of Gold Nanowires to TCR–LS Converted Diyne PE Monolayer Template Films

Because physical properties of nanocrystals (*e.g.* plasmon resonance wavelengths) and their coupling between nanocrystals vary with particle orientation and interparticle distance,[126-128] controlling ordering and orientation of anisotropic nanocrystals is a significant goal in next-generation materials. Both the assembly of high-aspect ratio particles (here, >200:1) and achieving interparticle spacings independent of nanocrystal ligand shell thickness are difficult to achieve using most superlattice assembly methods. For instance, the most common strategies, based on slow evaporation of solvent, rely on shape complementarity and contact between ligand shells to induce ordering.[129] However, recently, we have demonstrated that striped phases of diyne PE can be utilized to generate well-ordered arrays of long (300–500 nm), flexible AuNWs.[130] Here, we demonstrate the assembly of AuNWs on long flexible films of diyne PE striped phases first assembled on HOPG *via* TCR–LS conversion (Figure 3.7a), using a non-heated sequential rotary transfer approach in the second assembly step to increase the surface area of functionalization while providing large areas of ordered template surface.

AuNWs were synthesized using a previously reported procedure (see AuNW synthetic protocol in Appendix B),[130] which produces nanowires with metal core diameters of 1.5-2 nm (Figure 3.7b), with oleylamine ligand shells. Previously we have demonstrated that these flexible narrow wires interact with striped diyne PE surface templates containing arrays of orientable dipoles (Figure 3.7d), forming highly aligned arrays of individual AuNWs (Figure 3.7c,e), in a process that appears to involve polarization of the Au core to create repulsive interactions between the wires.[130]

Here, following TCR–LS assembly of a striped template of diyne PE on HOPG (Figure 3.7d), we lowered the rotating translation stage into contact (unheated, translation rate of 0.02 mm/s) with a reservoir of AuNW solution. This process generates large areas of highly aligned individual AuNWs on the template surface (Figure 3.7f). Figure 3.7f and 3.7g highlight the significance of domain size in orienting the flexible AuNWs over a given area of the diyne PE
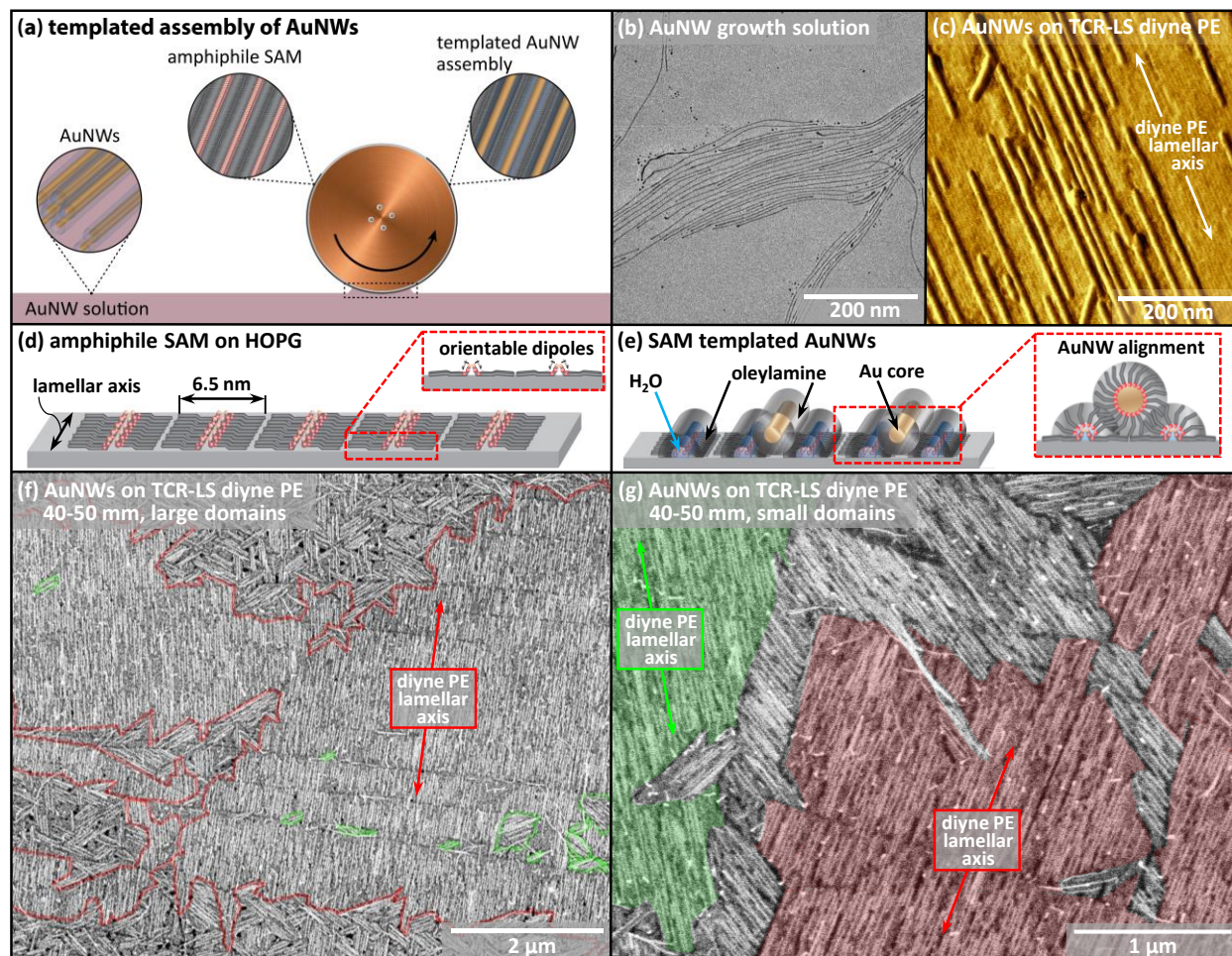
Figure 3.7. (a) Schematic illustrating sequential transfer of AuNWs to striped template. (b) TEM image of ultranarrow AuNWs. (c) AFM image of assembly of AuNWs on striped phase diyne PE. (d) Illustration of diyne PE SAM noncovalently adsorbed atop HOPG. (e) Illustration of AuNW alignment on diyne PE/H_2O/oleylamine stripes. (f-g) SEM images of AuNWs assembled on striped phase diyne PE template through sequential rotary transfer at room temperature. In (f), as a guide to the eye, the border of a large unidirectional diyne PE domain is highlighted in red; small inclusion domains with different lamellar axes highlighted in green. (g) Higher magnification SEM image highlighting AuNW alignment along diyne PE lamellar axes (green and red).

SAM template. Diyne phospholipid amphiphiles orient in epitaxy with the hexagonal HOPG lattice, resulting in ~120° angles between domain lamellar axes. In Figure 3.7g, two small diyne PE domains with different lamellar axes have been false colored green and red as a guide to the eye. Within both domains, the flexible AuNWs (observed as lighter contrast lines against the darker contrast diyne PE template) orient along the lamellar axes of the diyne PE domains. The flexibility of the AuNWs can be observed within the red domain, in wires adsorbed out of alignment with the lamellar axis (indicated with red arrow). A large area of a diyne PE SAM template that is

46

comprised of small domains would have poor overall unidirectional alignment of AuNWs. Conversely, Figure 3.7f highlights the ability of large unidirectional diyne PE domains (here, the perimeter of a large domain has been highlighted in red, with small inclusion domains with different lamellar axis direction highlighted in green) to orient AuNWs along a single axis over a large area of the molecular template. AuNW coverage extended the entire length of the HOPG film (Figure S.B.10), illustrating the capacity of the template to scalably guide heterostructured interface assembly.

3.2   Conclusion

We have shown that, using a temperature-controlled, variable-speed rotating transfer stage, it is possible to perform large-area functionalization of 2D materials with amphiphilic molecules via LS conversion. This approach produces very large (nearly 10,000 μm^2) ordered molecular domains, and can subsequently be used to direct assembly of other nanostructures (here, ultranarrow AuNWs). These findings lay foundations for the use of roll-to-roll transfer methods to leverage LS conversion for surface functionalization of 2D materials. Such a capability is potentially advantageous in applications that require large areas of functional surface, or benefit from long-range ordering within the functional film.

3.3   Experimental Methods

3.3.1   Materials

Absolute ethanol (100% purity) was purchased from Decon Labs, Inc. (King of Prussia, PA) and used as received. Methylene chloride (HPLC grade, ≥99.9% purity) and 2-propanol (HPLC grade, ≥99.9% purity) were purchased from Fisher Scientific (Fair Lawn, NJ) and used as received. Tetrachloroauric(III) acid trihydrate (ACS reagent grade, ≥49.0% Au purity) and cyclohexane (99.5% purity, extra dry) were purchased from ACROS Organics (Fair Lawn, NJ) and used as received. Chloroform (reagent grade, ≥99% purity), manganese(II) chloride tetrahydrate (dry basis, ≥98% purity), oleylamine (technical grade, 70% purity), triisopropylsilane (TIPS) (98% purity), and molecular sieves (4 Å) were purchased from MilliporeSigma (St. Louis, MO) and used as received. 1,2-bis(10,12-tricosadiynoyl)-*sn*-glycero-3-phosphoethanolamine (diyne PE) (>99.0% purity) was purchased from Avanti Polar Lipids, Inc. (Alabaster, AL) and used as received. Large

highly oriented pyrolytic graphite (HOPG) substrates (grade ZYA, 20-mm x 30-mm x 2-mm) were purchased from Momentive Performance Materials Quartz, Inc. (Strongsville, OH); smaller HOPG substrates (grade ZYA and ZYB, 10-mm x 10-mm x 1-mm) were purchased from MikroMasch (Watsonville, CA). Aluminum foil was purchased from Fisher Scientific (Fair Lawn, NJ). Adhesive transfer tape (3M product 9472LE), and high temperature polyimide tape (3M product 1218), were purchased from Digi-Key (Thief River Falls, MN). PELCO colloidal silver, 20-mm AFM metal specimen discs, standard SEM pin stub mounts, and double coated carbon conductive tape were purchased from Ted Pella, Inc. (Redding, CA). 0.01-0.025 Ω·cm Antimony (n)-doped Si Bruker RFESP-75 probes (nominal force constant 3 N/m and radius of curvature <12 nm) purchased from Bruker AFM Probes (Camarillo, CA) along with 0.01-0.025 Ω·cm (n)-doped silicon MikroMasch HQ:NSC18/No Al probes (nominal force constant 2.8 N/m with 8 nm radius of curvature) purchased from MikroMasch USA (Watsonville, CA) were used as received. Milli-Q water ($\geq$18.2 MΩ·cm resistivity) was used in all experiments. Ultra-high purity nitrogen (99.999% purity) was purchased from Indiana Oxygen Company (Indianapolis, IN).

3.3.2 Instrumentation

Self-assembled monolayers of diyne PE were prepared on a Kibron Langmuir–Blodgett trough (Helsinki, Finland). Atomic force micrographs were acquired using either a Veeco MultiMode AFM with NanoScope V controller (Bruker Instruments, Billerica, MA) or an Agilent 5500 AFM/SPM (Agilent Technologies, Inc., Palo Alto, CA). Scanning electron micrographs were acquired using a Teneo VS SEM (Thermo Fisher Scientific, Hillsboro, OR). Transmission electron micrographs were acquired using a Tecnai G2 20 TEM (Thermo Fisher Scientific, Hillsboro, OR).

3.3.3 Design of TCR–LS Transfer Stage

The thermally controlled rotary (TCR) LS transfer stage (Figure S.B.1) was designed and fabricated to allow a 3.0-in diameter x 1.0-in thick copper disk to rotate with programmable speed and temperature during Langmuir–Schaefer transfer. The copper disk was machined to house a type-K thermocouple along with 4 evenly spaced 20-W cartridge heaters connected in parallel. An external Omega temperature controller was used to regulate the input power supplied to the

cartridge heaters, enabling the surface of the substrate to be maintained at a specified setpoint temperature. Rotation of the copper disk was achieved using a brushless DC motor with a 200:1 gear head and programmable driver allowing a minimum shaft speed of 0.005 RPM, corresponding to a transit rate of 0.02 mm/s for the surface of the copper disk being drawn along the Langmuir film.

3.3.4   Preparation of Flexible HOPG Substrate Films

To enable LS conversion of standing phases into lying-down phases over large substrate areas using the TCR–LS transfer stage, pliant HOPG films were prepared to accommodate the curved surface of the copper disk (Figure S.B.2). First, a sheet of aluminum foil was affixed to the benchtop to provide a clean working surface. Next, a second sheet of aluminum foil was folded to form a 1.0-in wide belt (width of copper disk) and affixed at both ends to the first aluminum foil sheet. The top surface of the aluminum foil belt was then cleaned with 2-propanol to remove trace oils from its manufacturing process. Laminating adhesive transfer tape (3M product 9472LE) was cut to a desired length and affixed to the aluminum belt, with pressure from a weighted roller to ensure uniform contact.

Next, grade ZYA or ZYB HOPG was cleaved with high temperature polyimide tape (3M product 1218). Two parallel edges of the tape were carefully trimmed to ensure no adhesive was exposed between HOPG segments; each piece of trimmed polyimide tape was then affixed to the adhesive transfer tape with the edges of HOPG segments adjoined to form a contiguous film. The cleaving, cutting, and adhering cycle was repeated until the desired length of HOPG film was achieved. To avoid leaching of adhesive residue into the LB trough from the exposed top and bottom edges of the polyimide tape, additional polyimide tape was placed, adhesive side facing down, over the top and bottom exposed tape edges down the long axis of the belt. Finally, the top surface of the belt, excluding the freshly mounted HOPG cleaves, was cleaned a final time with 2-propanol.

3.3.5   TCR–LS Conversion of Diyne Phospholipids

Monolayers of noncovalently adsorbed diyne PE on HOPG were prepared via TCR–LS conversion under single barrier compression on a Kibron Langmuir-Blodgett trough. All sample

handling steps were performed under UV-filtered light to minimize photopolymerization. The trough and barriers were thoroughly cleaned with ethanol and water prior to the addition of a 5 mM $MnCl_2$ in Milli-Q water subphase. After cleaning the subphase through repeated barrier compression and aspiration, the subphase was heated to 30 °C using a ThermoTek T255P chiller and held at this temperature throughout the TCR–LS transfer. The Kibron trough was initialized to 21635 mm^2 and reduced in area to 21,000 mm^2 for each rotary LS conversion experiment to provide room for the temperature probe to be inserted between the outside edge of the left barrier and the wall of the trough. To improve amphiphile source film uniformity, 60 µL of 0.50 mg/mL diyne PE in $CHCl_3$ was spread evenly in a grid across the subphase, in 1-µL droplets, from the left barrier to the right barrier. The trough was equilibrated for 30 min to allow the $CHCl_3$ spreading solvent to evaporate. Following equilibration, single barrier compression of the phospholipid film was initiated by sweeping the left barrier in at 6.10 mm/min towards the right (stationary) barrier, until a target surface pressure of 30 mN/m was achieved. Once the target surface pressure was reached, the source film was maintained at 30 mN/m for 30 min while the flexible HOPG substrate film was prepared.

Prior to mounting the substrate film, the copper disk of the heated roller transfer stage was washed 3× with hexane and ethanol, and once with 2-propanol, to remove any residual tape adhesive or subphase salts from previous transfers. All TCR–LS conversions were performed with substrate set point surface temperatures of 80 ± 3 °C, as measured by an Analogic Digi-Cal II thermocouple calibrator, model AN6520, placed in direct contact with the substrate prior to deposition. Following mounting and heating of the substrate film on the copper disk, the TCR transfer stage was positioned next to the Kibron trough with the copper disk adjacent to the right barrier, and the bottom edge of the disk several mm above the trough. The copper disk (and mounted HOPG film) was lowered into contact with the Langmuir film, using the z-axis translation stage. The wheel was then rotated counterclockwise at shaft rotation rates calculated to cause the HOPG to translate across the Langmuir film at rates of 1.10 mm/s, 0.54 mm/s or 0.14 mm/s, corresponding to HOPG–Langmuir film contact times of 30 s, 1 min, and 4 min, respectively. Once the trailing edge of the HOPG film emerged from the receding HOPG–subphase contact meniscus, rotation was halted, and the copper disk was raised out of contact with the subphase.

Following each TCR–LS conversion transfer of diyne PE to HOPG, the pliant HOPG belt was removed from the copper wheel, flattened, and gently blown dry with ultra-high purity

nitrogen. Upon drying, the functionalized HOPG was placed under a 254 nm 8-W UV lamp for 1 h to initiate photopolymerization of the diacetylene groups in the functional molecular layer. The distance between the lamp and the sample surface was approximately 4 cm.

3.3.6 Sequential Rotary Transfer of AuNWs to TCR–LS Converted Diyne PE Monolayer Films

Sequential surface functionalization of TCR–LS transferred diyne PE monolayers with AuNWs (see AuNW synthetic protocol outlined above) was achieved via a roll-to-roll inspired processing technique in a humidity-controlled enclosure within a fume hood. First, the copper disk of the heated roller was cleaned thoroughly with three cycles of hexane and ethanol – ending with one rinse of 2-propanol – to remove any residual tape adhesive, subphase salts, or AuNW growth media and wires from previous experiments. Next, a petri dish was cleaned with DI water and soap, followed by three thorough rinse cycles of hexane and ethanol, and placed in an oven set to 130 °C for 30 min to dry. While the petri dish was in the oven, an aluminum lab jack was placed alongside the heated roller transfer stage. Next, the TCR–LS diyne PE monolayer belt was removed from the vacuum desiccator it was held in overnight.

Once removed from the vacuum desiccator, the diyne PE monolayer belt was tightly mounted to the TCR transfer stage with 3M high temperature polyimide 1218 tape. To remove any adhesive residues transferred to the top edges of belt from handling the tape during mounting, a Kimwipe saturated with 2-propanol was run down the edges of the film atop the downward facing polyimide tape (see Preparation of flexible HOPG substrate films above). Once the film was mounted, the petri dish was retrieved from the oven and place atop the aluminum lab jack to cool. A humidity logger (Onset HOBO MX1101 temp/RH logger) was placed next to the petri dish atop the aluminum jack. While the petri dish cooled, the humidity control enclosure was placed over the TCR apparatus and purged with nitrogen gas until the relative humidity fell within the range of 15% ± 2% RH.

Upon reaching the desired 15% ± 2% RH range, the humidity enclosure was briefly raised to allow 50 mL of the 14.5-h aged AuNW growth solution to be added to the petri dish. Once the humidity control box was repositioned over the TCR stage, the enclosure was sealed airtight to the fume hood benchtop with duct tape, allowing the relative humidity to quickly re-equilibrate to ~15%. Next, the floor jack was raised in order to bring the AuNW growth solution into contact

with the diyne PE monolayer film. The disk was then rotated counterclockwise in the same motion as the initial transfer cycle. The linear velocity of the disk was set to 0.02 mm/s.

To obtain uniform AuNW surface density across the entire length of the TCR–LS diyne PE monolayer film (Figure S.B.10), 5 mL of "used" (from the petri dish) AuNW solution was removed and replaced with 5 mL of "fresh" (from remaining 50 mL of the 14.5-h aged AuNW solution prepared for experiment) AuNW solution every 12 min via a 10-mL syringe through a small hole in the humidity enclosure. The relative humidity throughout the rotary transfer was measured at 14.3% ± 0.7% RH.

After the last portion of the TCR–LS diyne PE monolayer film passed through the receding diyne PE/AuNW growth solution contact meniscus, the belt was brought out of contact with the growth solution by lowering the lab jack. Following the removal of the film from the copper disk, the film was washed with 1 mL cyclohexane (growth solution solvent) per 10-mm segment of film to ensure any excess oleylamine capping ligands were removed from the film.

3.3.7   AFM Imaging

All standard AFM measurements and micrographs were acquired using either a Veeco MultiMode with Nanoscope V controller (Bruker Instruments, Billerica, MA) in tapping mode with 0.01-0.025 $\Omega\cdot$cm Antimony (n)-doped Si Bruker RFESP-75 probes (nominal force constant 3 N/m and radius of curvature <12 nm), or an Agilent 5500 AFM/SPM (Agilent Technologies, Inc., Palo Alto, CA) in tapping mode with 0.01-0.025 $\Omega\cdot$cm (n)-doped silicon MikroMasch HQ:NSC18/No Al probes (nominal force constant 2.8 N/m and with 8 nm radius of curvature).

3.3.8   TEM Imaging

All TEM images were acquired from a Tecnai G2 20 (Thermo Fisher Scientific, Hillsboro, OR) with a lanthanum hexaboride (LaB$_6$) filament at an accelerating voltage of 200 kV. TEM grids were prepared by dropping 5 µL of the AuNW growth solution on a copper grid covered by a carbon film.

3.3.9 SEM Imaging

Scanning electron micrographs were acquired using a Teneo VS SEM (Thermo Fisher Scientific, Hillsboro, OR). Samples were cut from the pliant HOPG films and mounted onto 20-mm AFM metal specimen discs with double coated carbon conductive tape. PELCO colloidal silver was applied around the sample perimeter to provide enhanced electrical contact between the sample and the specimen disc, minimizing surface charging during SEM imaging. Samples on specimen discs were then mounted to standard SEM pin stub mounts with double coated carbon tape. High resolution imaging of horizontally-oriented striped phase SAMs and surface-templated AuNW arrays prepared by rotary transfer was achieved using the in-column Trinity detector T3 in OptiPlan mode at working distances of 5-6 mm. Beam currents in the range of 0.20-0.80 nA were selected for best resolution image acquisition through a 32-µm diameter aperture with an accelerating voltage of 5.00 kV.

3.3.10 SEM Image Analysis

Functionalization was examined at five evenly spaced testing zones along the flexible HOPG substrate film, as described in the manuscript. X coordinates were 10–20 mm (the first segment of HOPG to contact the Langmuir film as the disk is lowered), 40–50 mm, 70–80 mm, 100–110 mm, and 130–140 mm (last segment). To quantify the surface coverage of the diyne PE monolayer along the flexible HOPG film for each of the three translation rates tested, low magnification (5,000×, 82.9 µm HFW (horizontal field width)) SEM images were acquired from three discrete locations within each of the five testing zones. We then selected the most representative low magnification image from each of the three discrete imaging locations and masked unfunctionalized areas within each image *via* color thresholding in ImageJ. Quantification of masked pixel area per SEM image allowed us to calculate the average surface coverage and its associated standard deviation (Figure 3.4e) for each of the five testing zones (Figure 3.4d) The masked and unmasked images we used to quantify the surface coverage in Figure 3.4e are included in Appendix B (Figures S.B.3-S.B.8).

3.3.11 Molecular Modeling

Software packages Maestro and Macromodel (Schrödinger, Cambridge, MA) were used, respectively, to visualize the structures of diyne phospholipids on graphene and to perform force field minimizations. All models were simulated using the OPLS_2005 force field, with implicit water solvent file and extended cutoffs for van der Waals, electrostatic, and hydrogen-bonding interactions. Minimizations were performed using the Polak-Ribiere conjugate gradient (PRCG) algorithm and gradient method with 50,000 runs and a convergence threshold of 0.05.

APPENDIX A. SUPPORTING INFORMATION FOR CHAPTER 2

Multimicrometer Noncovalent Monolayer Domains on Layered Materials through Thermally Controlled Langmuir–Schaefer Conversion for Noncovalent 2D Functionalization

Dry Annealing of PE Films

Films of diyne PE were subjected to dry thermal annealing at 50 °C to examine the extent to which domain uniformity and size could be increased. Figure S.A.1a and S.A.1d show 10 μm and 3 μm AFM images of a sample transferred at room temperature, prior to thermal annealing. Long, narrow domains stretch between step edges in the HOPG substrate. Figure S.A.1b and S.A.1e) show the same areas of the surface after 15 minutes of heating at 50 °C. A few of the needle-like domains have merged. After 60 minutes of heating (Figure S.A.1c and S.A.1f), further domains have merged, but many vacancies are still visible.
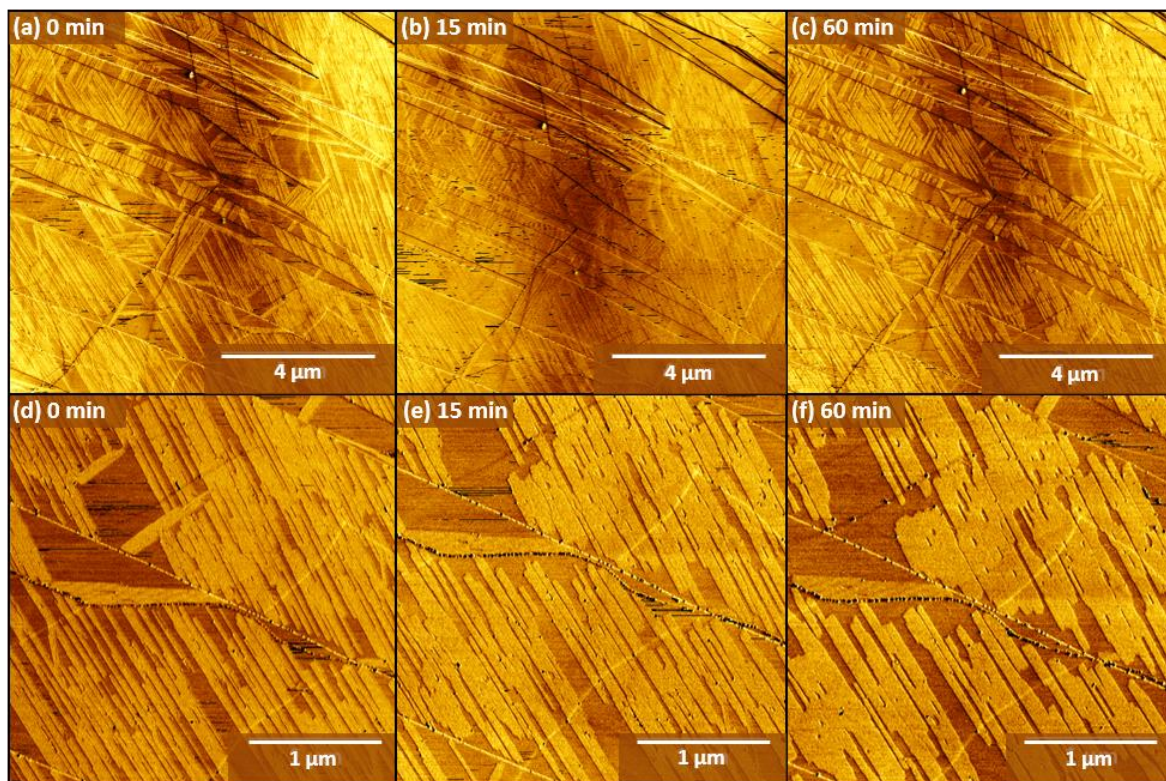
Figure S.A.1. AFM images of diyne PE monolayers (a,d) before and (b,c,e,f) after dry annealing at 50 °C.

Unprocessed AFM Images Showing Effect of Temperature on Transferred Domain Structure

Samples were prepared by transferring molecules to substrates mounted on the heated dipper with setpoint temperatures from 20–90 °C, and 1-minute transfer times. In the manuscript, edges at which the molecular alignment changes are highlighted as a guide to the eye; here, original images are shown at larger scales in Figures S.A.2 and S.A.3 for comparison.
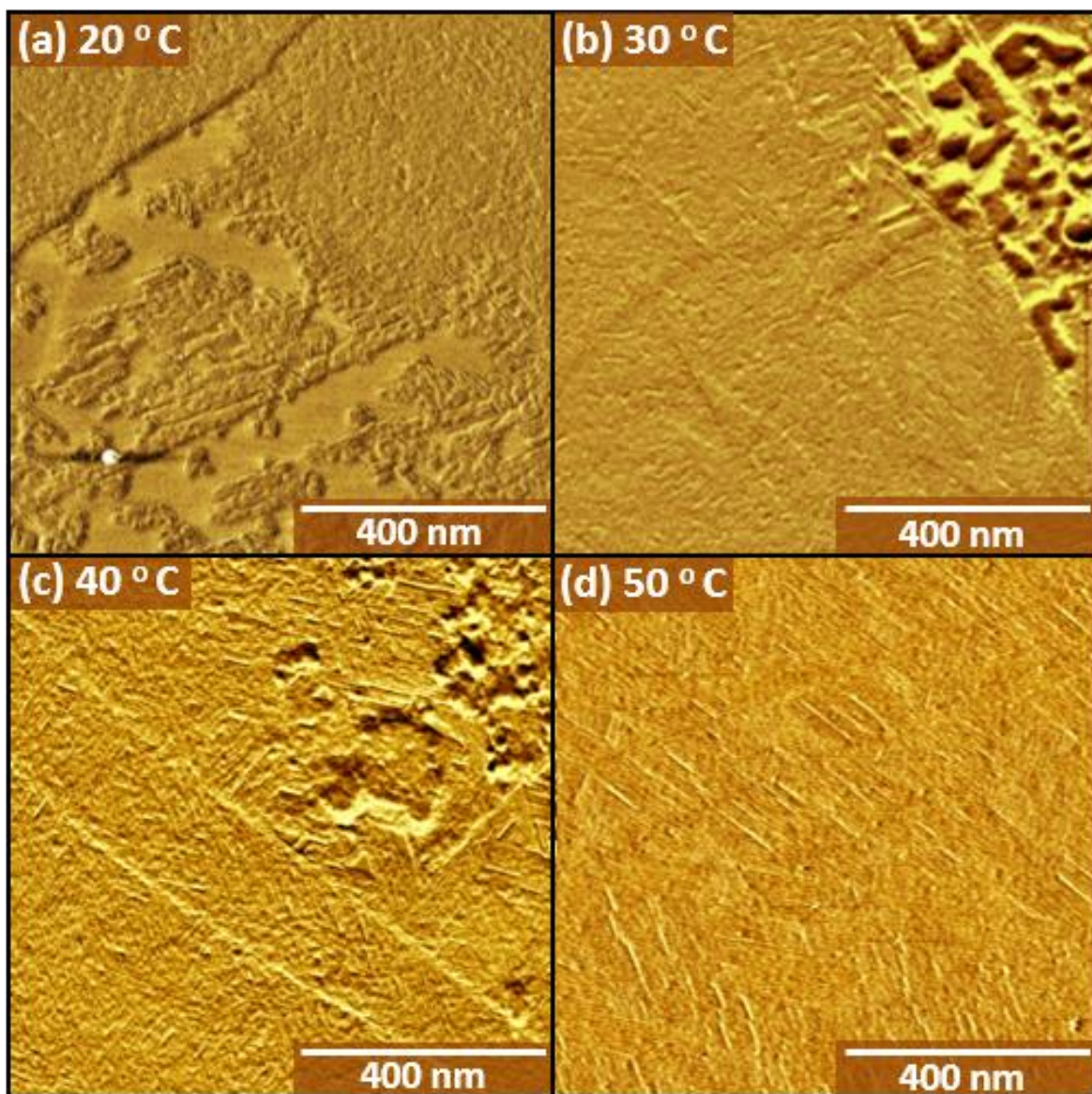
Figure S.A.2. Unprocessed AFM images showing domain structures after 1-minute sample contact, with dipper setpoint at stated temperature: (a) 20 °C, (b) 30 °C, (c) 40 °C, or (d) 50 °C.
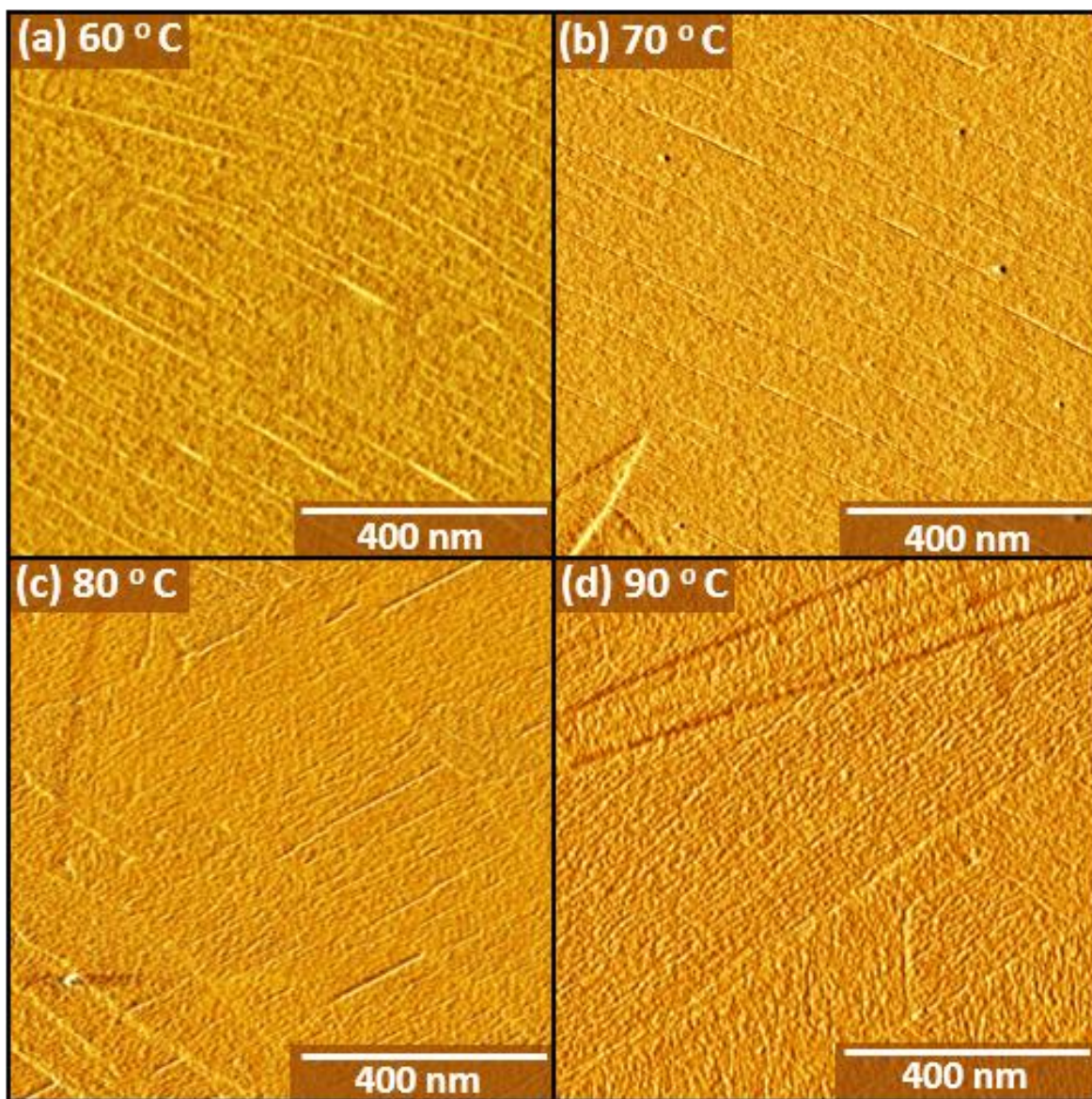
Figure S.A.3. Unprocessed AFM images showing domain structures after 1-minute sample contact with heated dipper setpoint at stated temperature: (a) 60 °C, (b) 70 °C, (c) 80 °C, or (d) 90 °C.

Effects of Increased Transfer Time on Domain Structure

To examine the effects of transfer time on domain structure, samples were transferred with contact times ranging from 1 to 30 minutes. Figure S.A.4 shows typical images acquired from samples with 1-minute (Figure S.A.4a,d), 10-minute (Figure S.A.4b,e), and 30-minute (Figure S.A.4c,f) contact times. After 1-minute, multiple-µm domains are already evident. Although qualitatively there appears to be a slight increase in overall ordering at timepoints greater than 1-minute, topographical asperities (including step edges) in the HOPG surface appear to have

a stronger influence on the molecular ordering. Although we observe a general decrease in domain size at shorter transfer times (< 1-minute), it is difficult to precisely quantify the relationship between contact time and domain size, due to uncertainties in the transfer time (*ca.* 10 s) introduced by the slow withdrawal of the dipper from the aqueous subphase.
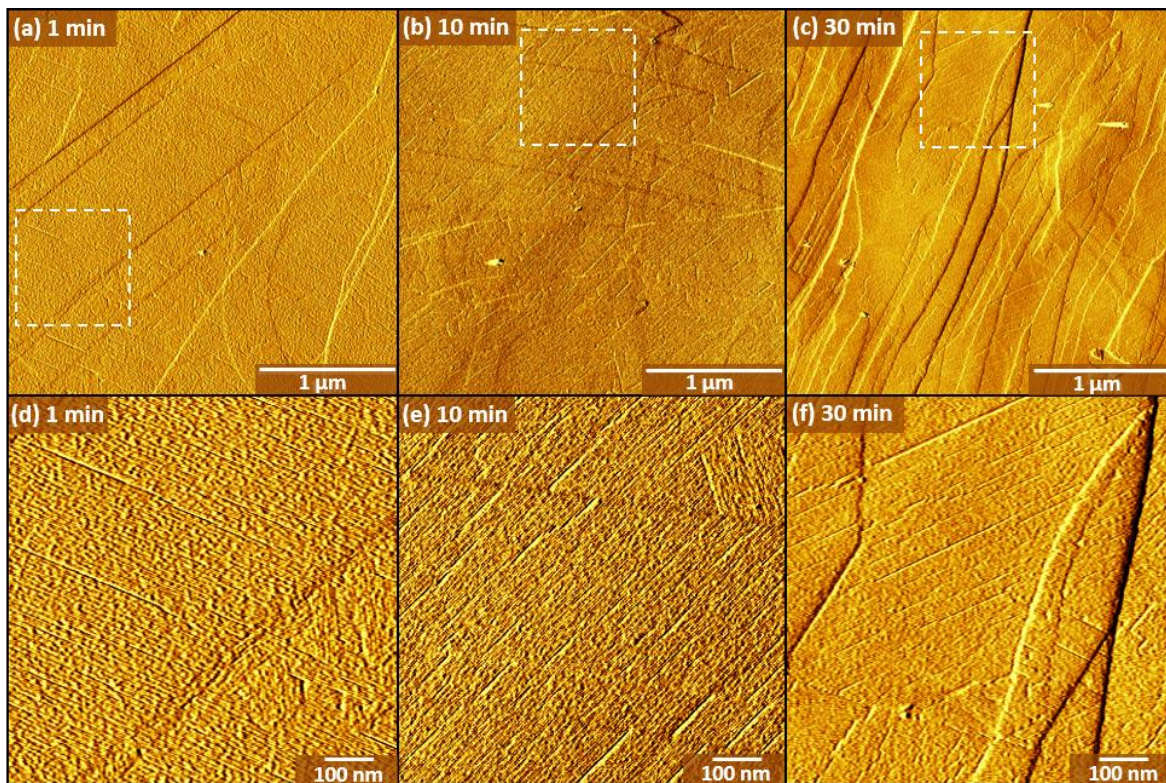
Figure S.A.4. AFM images of diyne PE samples with (a) 1-minute, (b) 10-minute, and (c) 30-minute transfer times. (d–f) show higher resolution images in areas highlighted with dotted white lines in (a–c).

Large-Scale Image of Long-Range Ordering

Optimized transfer protocols lead to routine transfer of domains with very long-range alignment. Due to the fairly small topography and phase contrast variations in the monolayer relative to HOPG surface topography, polymerization-induced cracking defects are highlighted in the version of the image presented in the manuscript, to assist in visualizing long-range order. Here, the unadjusted image (Figure S.A.5) is shown at larger scale for visual comparison.
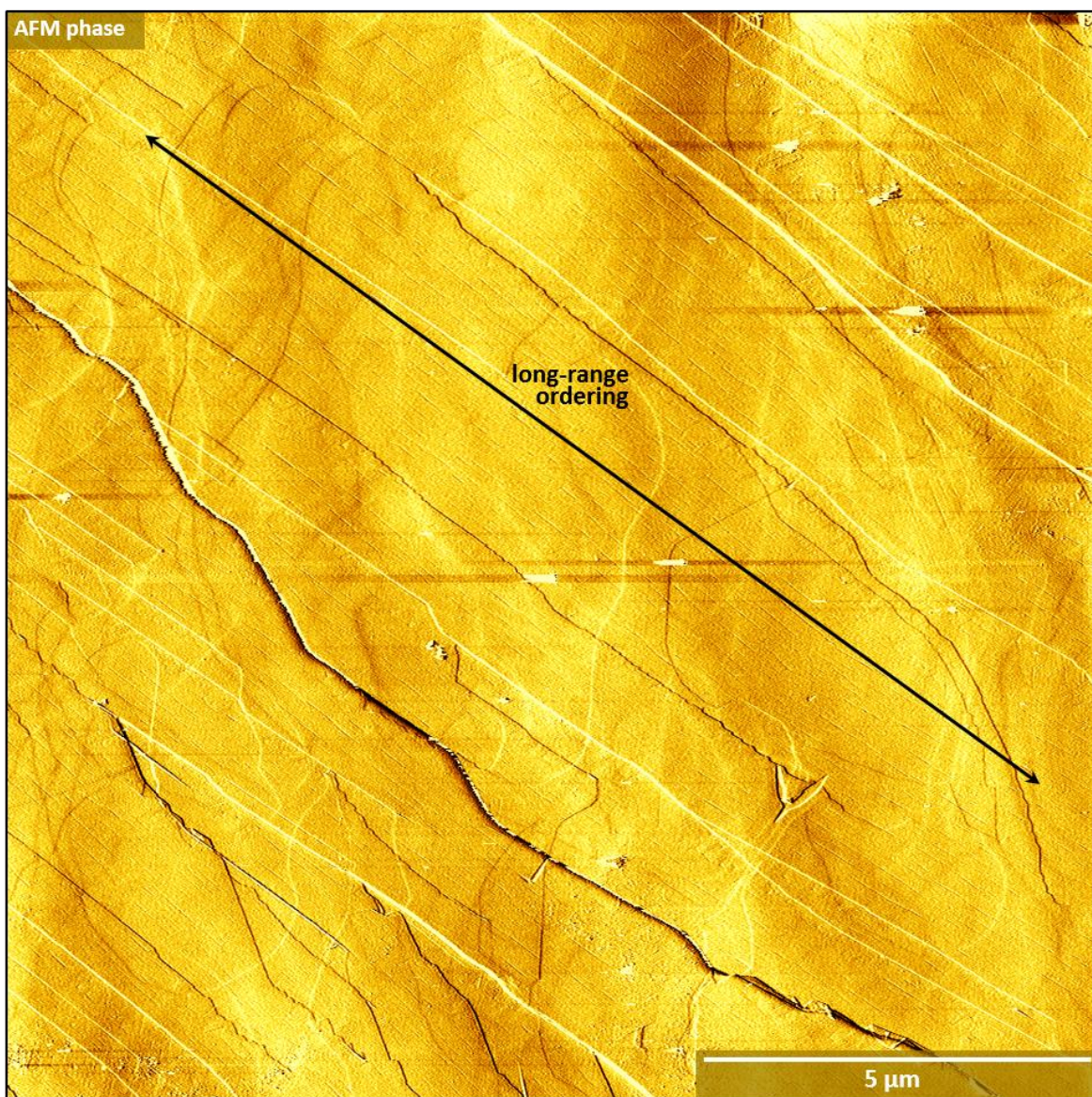
Figure S.A.5. AFM image of diyne PE film transferred at 70 °C setpoint temperature with 1-minute transfer time.

Large-Scale Images of Solution-Processed Diyne PE Films

To compare robustness toward solution processing based on transfer conditions, films of diyne PE transferred either at room temperature or with *in situ* thermal annealing at 70 °C for 1-minute were washed vigorously with solvent for 5-second intervals and then dried with nitrogen and imaged after 5, 10, 15, and 30 seconds total washing. Figures S.A.6 and S.A.7 show pre-wash images (panels a and d), as well as images acquired after a total of 10 seconds (panels b and e) or 30 seconds (panels c and f) of washing with ethanol. Samples transferred at room temperature

(Figure S.A.6) experienced loss of molecules from the monolayer after both 10 and 30 seconds of washing, visible as vacancies in the high-resolution topographic images in Figure S.A.6b,c. Images in (a-c) and (d-f) were acquired through repeated imaging of the same position in the sample, to facilitate comparison. Larger scale (3 μm edge length) phase images reveal variations in phase contrast at 10 seconds (e) and 30 seconds (f) that illustrate similar loss of molecules across the surface. Each sample was imaged in at least three large-scale locations to verify that the coverages were representative of the entire sample.

Figure S.A.6. AFM images of diyne PE samples transferred at room temperature and washed with EtOH. (a,d) High-resolution and larger-scale images of the sample surface prior to washing. High-resolution and larger scale images of the same position on the sample after (b,e) 10 seconds and (c,f) 30 seconds of vigorous washing with EtOH.

In comparison with the fractional loss in surface coverage in Figure S.A.6, samples transferred with *in situ* thermal annealing at 70 °C for 1 minute (Figure S.A.7) experience very minimal loss of surface coverage, even after vigorous washing with ethanol for 30 seconds (Figure S.A.7c,f).
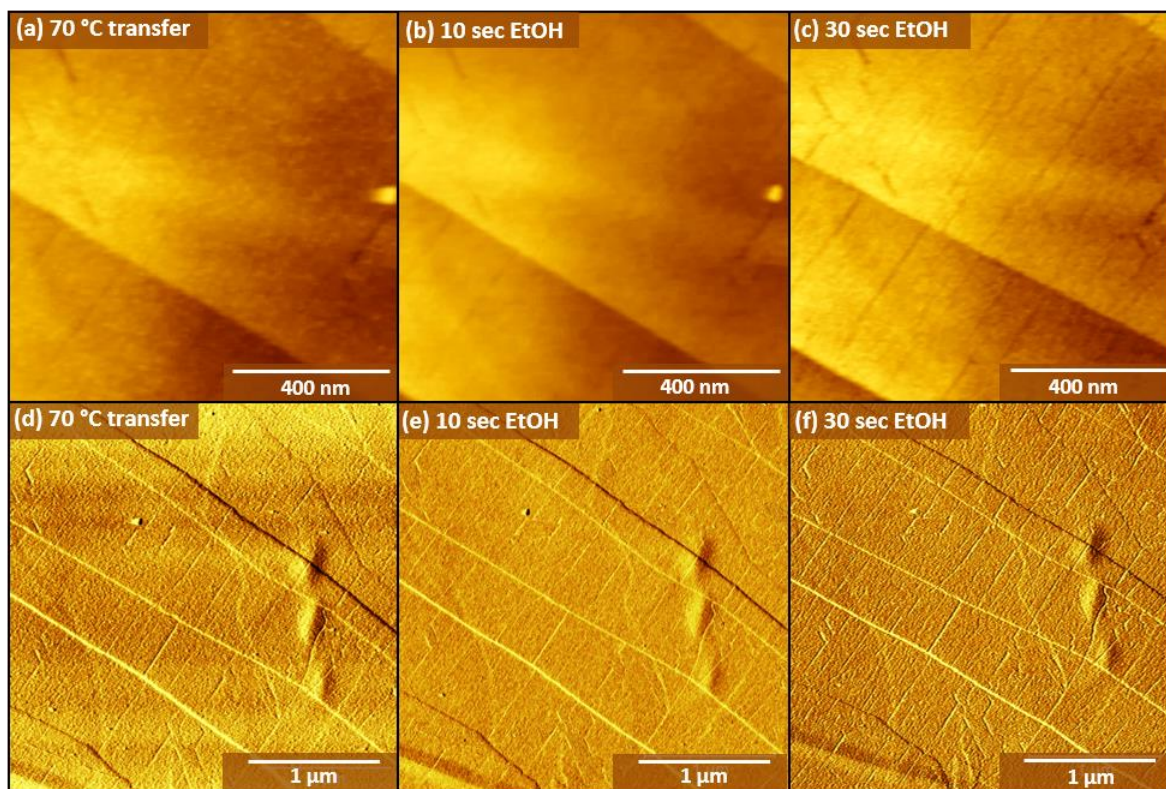
Figure S.A.7. AFM images of diyne PE samples transferred with *in situ* thermal annealing at 70 °C for 1 minute and washed with EtOH. (a,d) High-resolution and larger-scale images of the sample surface prior to washing. High-resolution and larger scale images of the same position on the sample after (b,e) 10 seconds and (c,f) 30 seconds of vigorous washing with EtOH.

Samples were also washed with other solvents for comparison. Figures S.A.8 and S.A.9 show the results of washing non-annealed and annealed samples with deionized water. While we had anticipated that the higher surface tension solvent might accelerate the loss in surface coverage, we find that both non-annealed (Figure S.A.8) and annealed (Figure S.A.9) samples retain essentially complete coverage after washing with water. We postulate that the hydrophobic alkyl chains that comprise the majority of the exposed monolayer retain greater ordering when the surface is exposed to water (*vs.* ethanol). Decreasing the per-chain van der Waals interactions with the solvent could then result in the observed decrease in molecular loss during washing. Washing non-annealed (Figure S.A.10) and annealed (Figure S.A.11) samples with THF yields similar results. Washing with toluene, the least polar solvent tested here, resulted in minimal molecular removal and/or disordering for samples transferred with either room temperature or annealing protocols (Figures S.A.12 and S.A.13). We note that in samples transferred at room temperature, there are frequently areas of standing phase molecules, and that washing sometimes has the impact

of redistributing molecules from these areas into vacancies on the surface. This type of backfilling is observed in a vacancy in the larger-scale image series in Figure S.A.8. Areas without large-scale vacancies were selected for the surface coverage analysis in the manuscript.
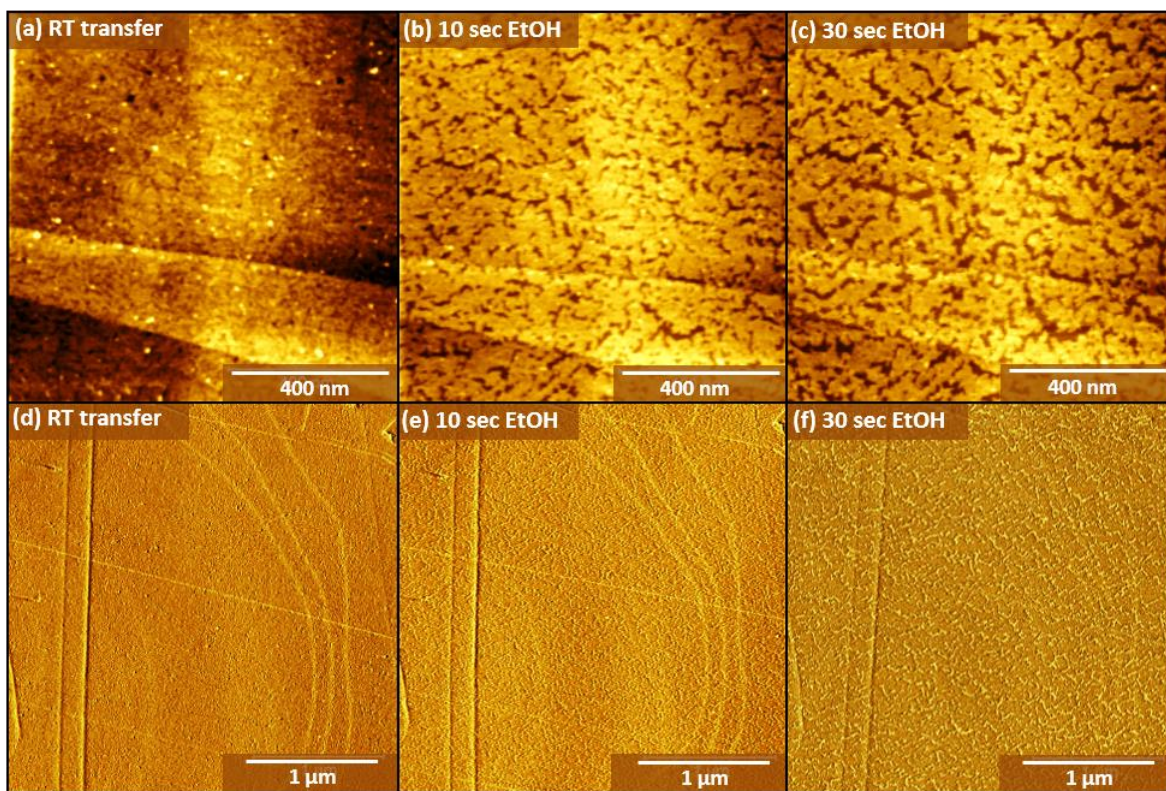

Figure S.A.8. AFM images of diyne PE samples transferred at room temperature and washed with ddH$_2$O. (a,d) High-resolution and larger-scale images of the sample surface prior to washing. High-resolution and larger scale images of the same position on the sample after (b,e) 10 seconds and (c,f) 30 seconds of vigorous washing with ddH$_2$O.
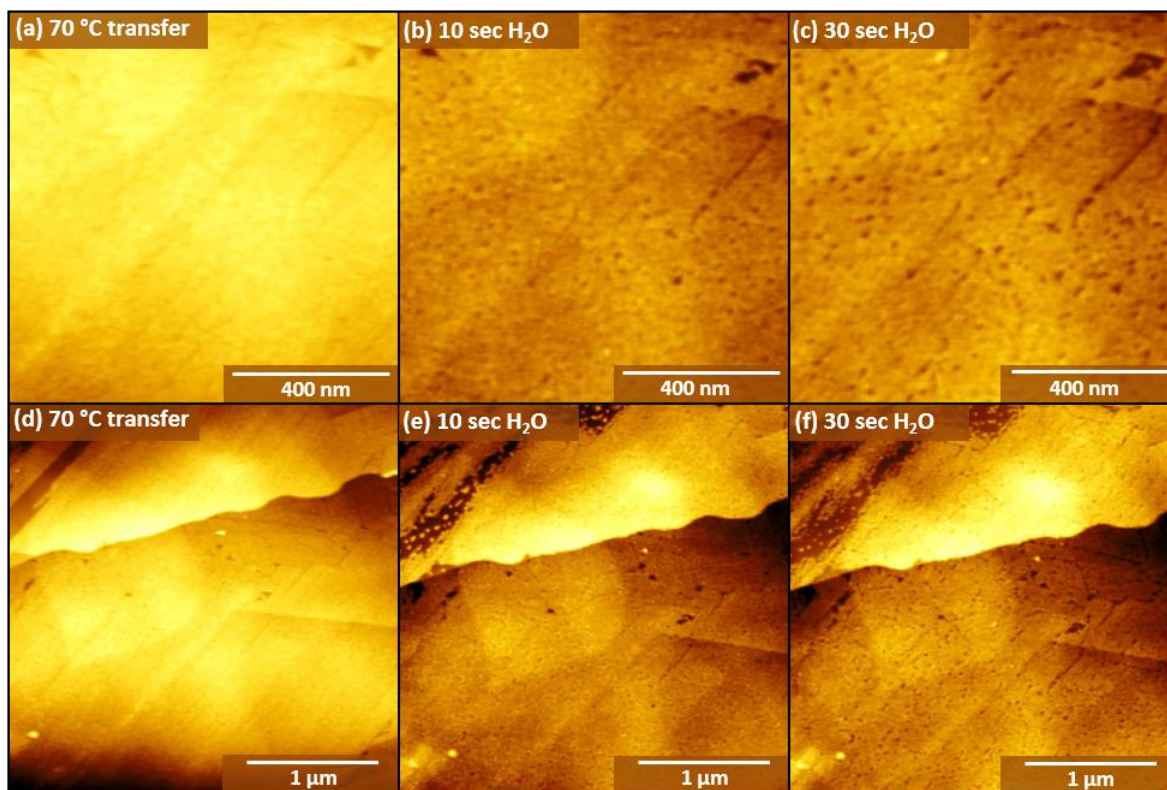
Figure S.A.9. AFM images of diyne PE samples transferred with *in situ* annealing and washed with ddH$_2$O. (a,d) High-resolution and larger-scale images of the sample surface prior to washing. High-resolution and larger scale images of the same position on the sample after (b,e) 10 seconds and (c,f) 30 seconds of vigorous washing with ddH$_2$O.
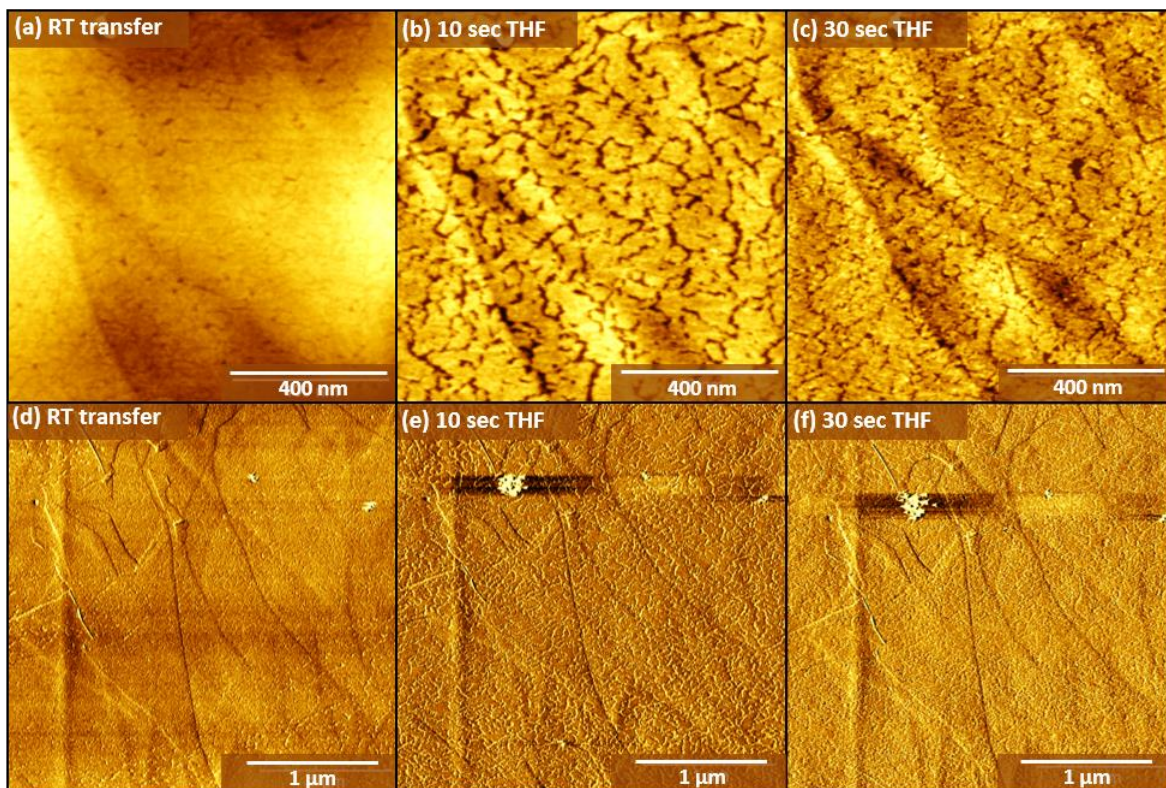
Figure S.A.10. AFM images of diyne PE samples transferred at room temperature and washed with THF. (a,d) High-resolution and larger-scale images of the sample surface prior to washing. High-resolution and larger scale images of the same position on the sample after (b,e) 10 seconds and (c,f) 30 seconds of vigorous washing with THF.
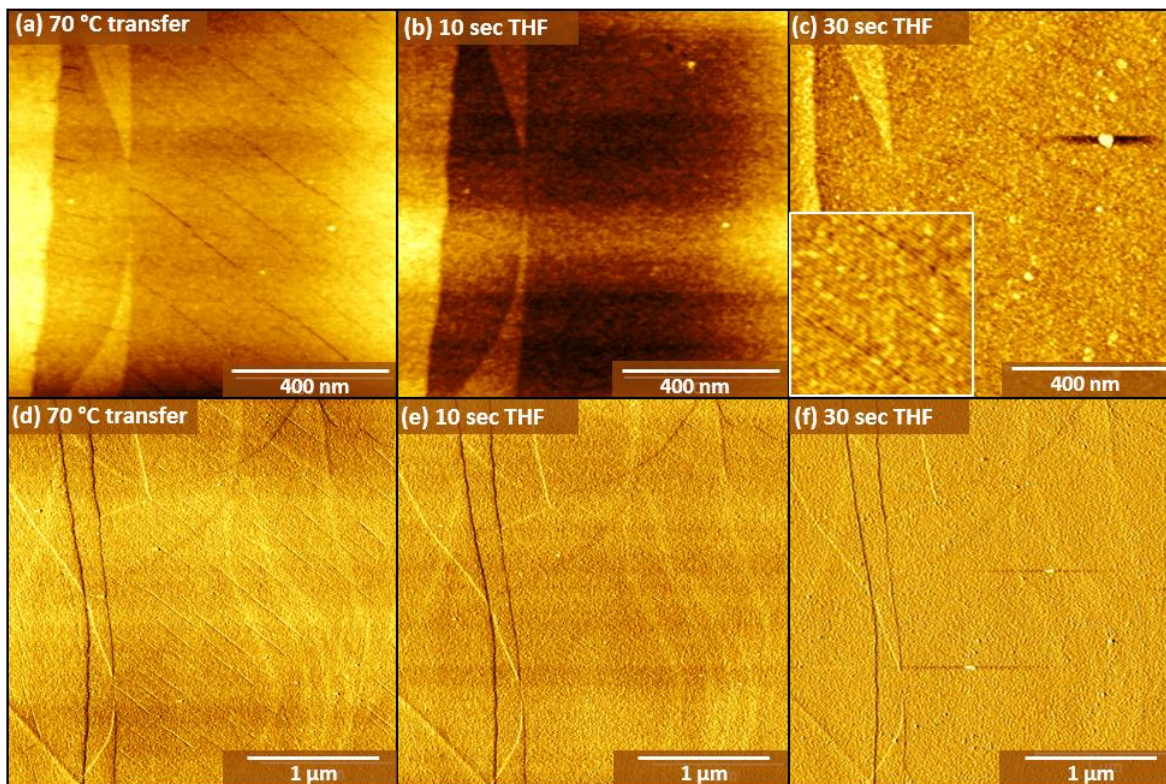
Figure S.A.11. AFM images of diyne PE samples transferred with *in situ* annealing and washed with THF. (a,d) High-resolution and larger-scale images of the sample surface prior to washing. High-resolution and larger scale images of the same position on the sample after (b,e) 10 seconds and (c,f) 30 seconds of vigorous washing with THF.
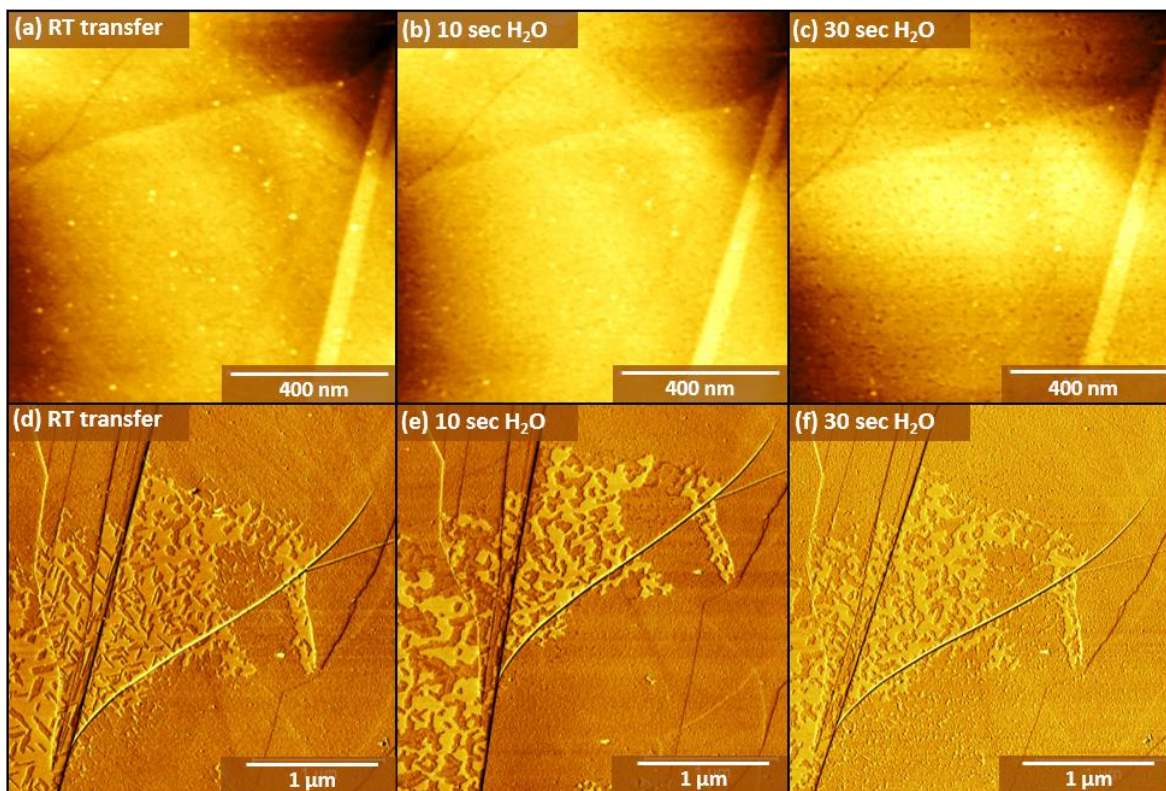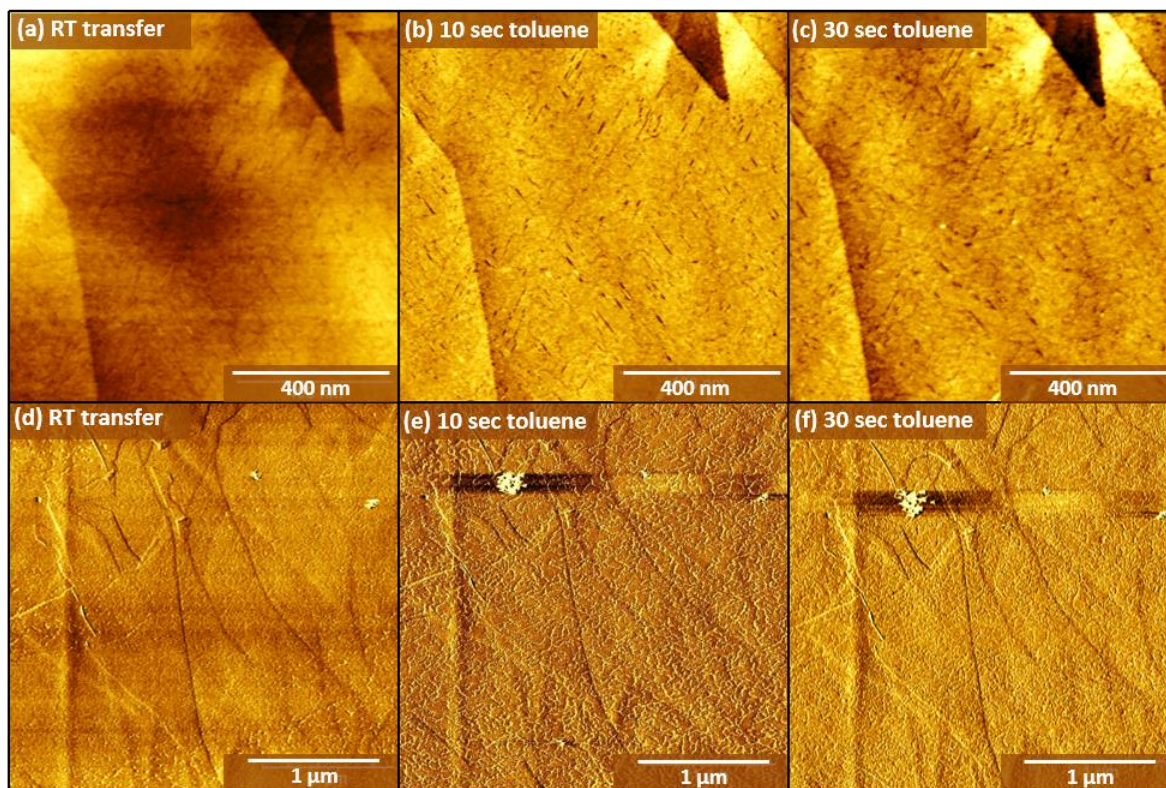
Figure S.A.12. AFM images of diyne PE samples transferred at room temperature and washed with toluene. (a,d) High-resolution and larger-scale images of the sample surface prior to washing. High-resolution and larger scale images of the same position on the sample after (b,e) 10 seconds and (c,f) 30 seconds of vigorous washing with toluene.
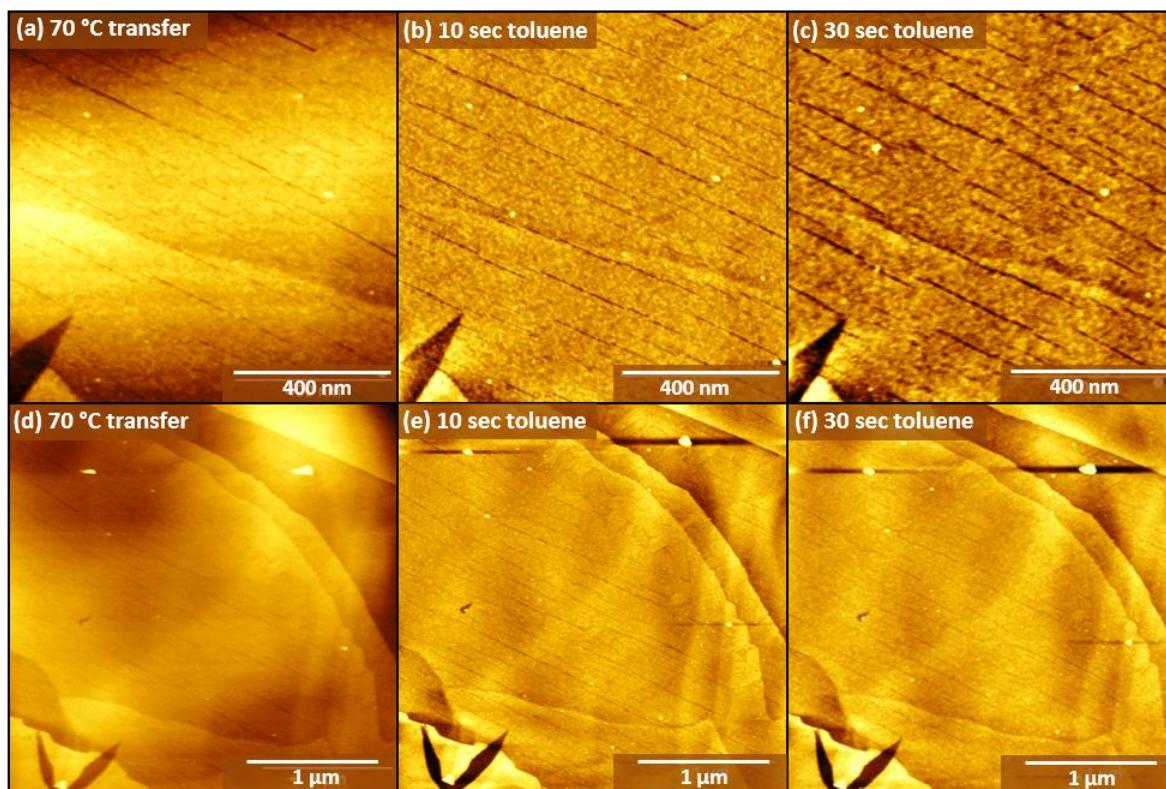
Figure S.A.13. AFM images of diyne PE samples transferred with in situ annealing and washed with toluene. (a,d) High-resolution and larger-scale images of the sample surface prior to washing. High-resolution and larger scale images of the same position on the sample after (b,e) 10 seconds and (c,f) 30 seconds of vigorous washing with toluene.

Surface Coverage Quantification of Solvent-Washed Diyne PE Thin Films

Fractional surface coverage after solvent washing was quantified by digital image analysis. Images were initially processed using Gwyddion SPM software (www.gwyddion.net). Raw bitmap images were subjected to data leveling by mean plane subtraction, median row alignment, and horizontal scar correction.

After initial image processing, the bitmap file was opened within Adobe Photoshop (Figure S.A.14a). To aid in the selection of pixels representing vacancies, image brightness and contrast were adjusted (Figure S.A.14b,c). Next, black pixels were manually selected using the automated region selection tool (Figure S.A.14d).. Subsequently, the highlighted pixel count was obtained from the image analysis measurement log. The fractional coverage was calculated as the fraction of selected pixels divided by the total pixels in the image.
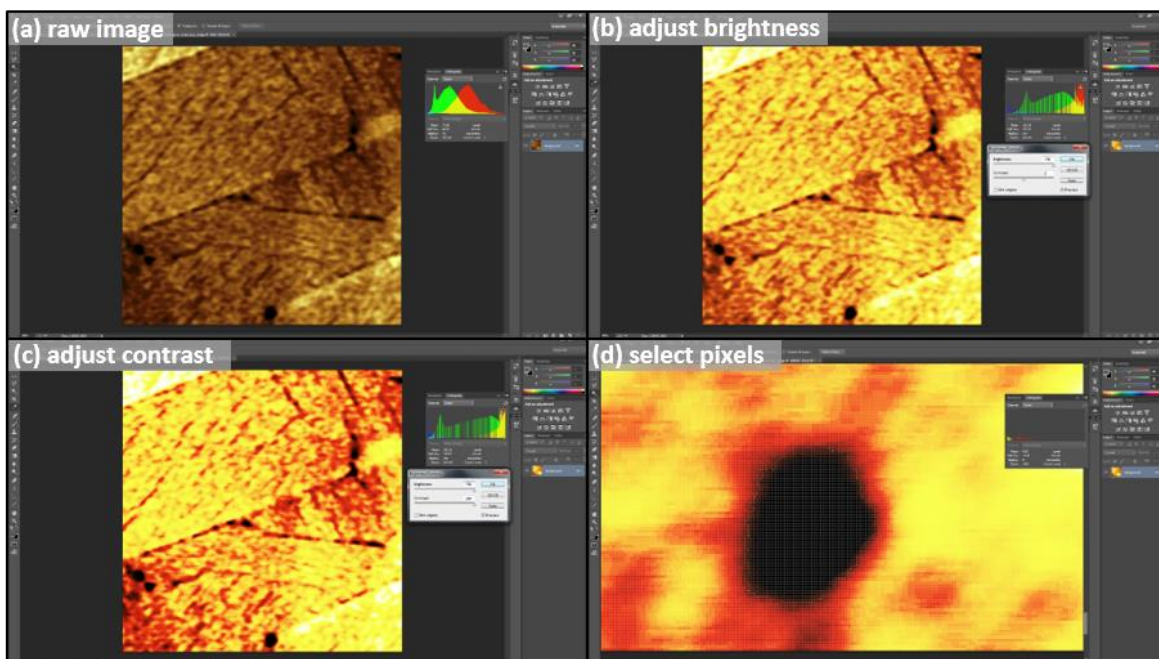
Figure S.A.14. (a) MultiMode AFM bitmap image processed with Gwyddion SPM data analysis software opened in Adobe Photoshop CC 2015, (b) image contrast increased, (c) image brightness increased, (d) black pixels were manually selected under image magnification using the magic wand tool with a set tolerance value ≤ 15.

Domain Edge Contour Density Quantification of Solvent-Processed Diyne PE Thin Films

Domain edge contour density was quantified through digital image analysis using the same initial raw bitmap file workup with Gwyddion SPM software previously described for surface coverage quantification. Image brightness and contrast were adjusted using Adobe Photoshop (Figure S.A.15a), and manual edge selection with a stylus was used to create a mask layer including cracking defects (Figure S.A.15b), and excluding cracking defects (Figure S.A.15c). The traced pixel count was obtained from the measurement log and converted to units of length (µm) based on the scan area of the 1024×1024 pixel AFM micrograph.
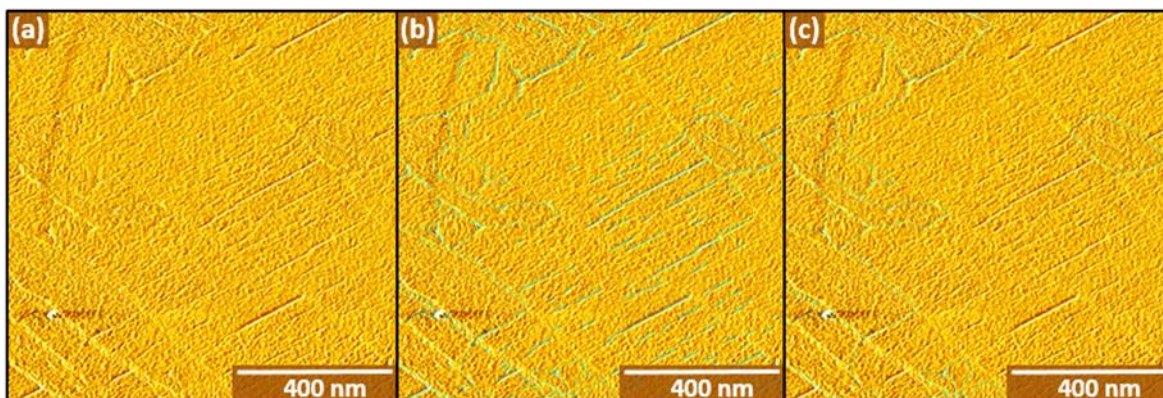
Figure S.A.15. Example AFM phase image from the diyne PE film transferred for 1 minute with a stage setpoint temperature of 80 °C. (a) Image after global contrast enhancement, (b) domain edge mask trace including cracking defects, and (c) domain edge mask trace excluding cracking defects.

Schematic of Thermally Controlled LS Transfer Stage

As described in the manuscript, the transfer stage comprises an aluminum cylinder with an embedded cartridge heater regulated by a PID controller (Figure S.A.16a). Samples are mounted on the cylinder utilizing standard 12 mm diameter high quality magnetic stainless steel AFM specimen discs (alloy 430, Ted Pella, Inc.) that mount onto a magnet recessed in the body of the cylinder. Prior to dipping, the temperature of each substrate is measured using a thermocouple placed in contact with at least two different areas on the substrate surface (Figure S.A.16b). HOPG is cleaved after contact with the thermocouple to ensure a clean surface is exposed for molecular transfer (Figure S.A.16c). Tests of HOPG surface temperature immediately as the surface breaks contact with the aqueous subphase indicate that the surface remains within 2 °C of the setpoint temperature at 50 °C, and within 5 °C of the setpoint temperature at 80 °C.
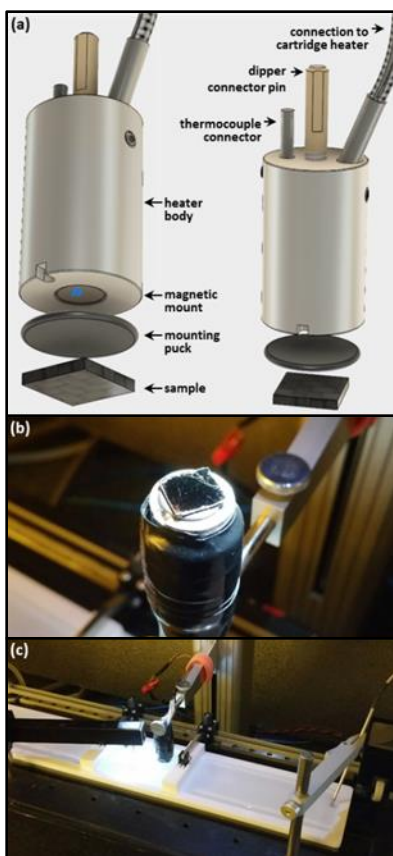
Figure S.A.16. (a) Fusion360 CAD schematic of heated dipper attachment, (b) photograph of sample mounted on dipper attachment, and (c) photograph of dipper attachment mounted on commercial Langmuir trough dipper accessory.

Effect of Up/Down Temperature Ramps on Transferred Domain Structure

To examine the effects of temperature ramps during *in situ* annealing on domain structure, samples were prepared by mounting a substrate on the dipper assembly heated to an initial setpoint temperature and then guided through a temperature ramp during molecular transfer, utilizing a relatively slow ramp rate of 5 °C/min. Figure S.A.17 shows representative images acquired from samples prepared with a ramp-up transfer from 50 °C to 70 °C (Figure S.A.17a,e), ramp-up transfer from 55 °C to 85 °C (Figure S.A.17b,f), ramp-down transfer from 85 °C to 55 °C (Figure S.A.17c,g), and ramp-down transfer from 85 °C to 35 °C (Figure S.A.17d,h).

The temperature ranges over which the ramp up and ramp down depositions were performed were chosen to bracket the temperature range over which large ordered domains were observed in single-temperature transfer (Figure S.A.17a,e), or to bracket the upper (Figure S.A.17b,f and Figure S.A.17c,g) and lower bounds (Figure S.A.17d,h) of our temperatures

examined in the manuscript. Overall, the diyne PE films under ramp-up and ramp-down conditions do not exhibit appreciable changes in domain transfer in comparison with transfers at single setpoint temperatures.
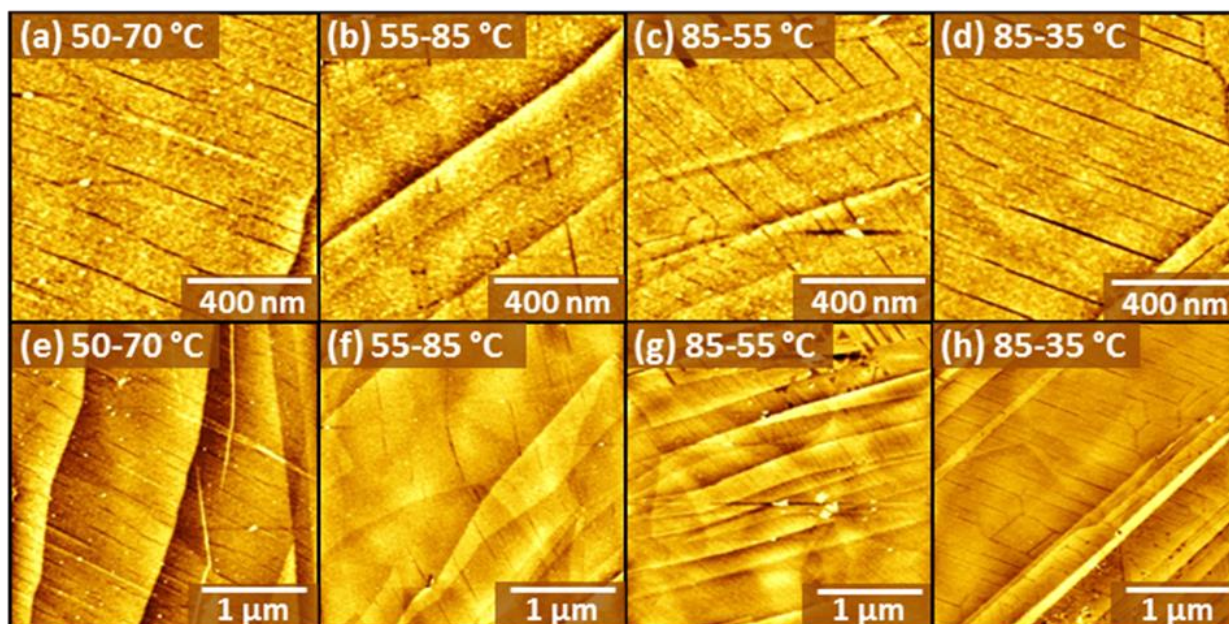
Figure S.A.17. AFM images of diyne PE samples transferred with *in situ* annealing and temperature ramps. High-resolution and larger-scale images of transfer with ramp up from 50 °C to 70 °C (a,e), ramp-up from 55 °C to 85 °C (b,f), ramp-down from 85 °C to 55 °C (c,g), and ramp-down from 85 °C to 35 °C (d,h).

APPENDIX B. SUPPORTING INFORMATION FOR CHAPTER 3

Large-Scale Noncovalent Functionalization of 2D Materials through Thermally Controlled Rotary Langmuir–Schaefer Conversion

Design of TCR–LS Transfer Stage

In the *Experimental Methods* section of the main manuscript, we describe the design of the thermally controlled rotary transfer stage in detail. Here we provide a CAD schematic (Figure S.B.1) of the stage with labeled key components that promote TCR–LS conversion.
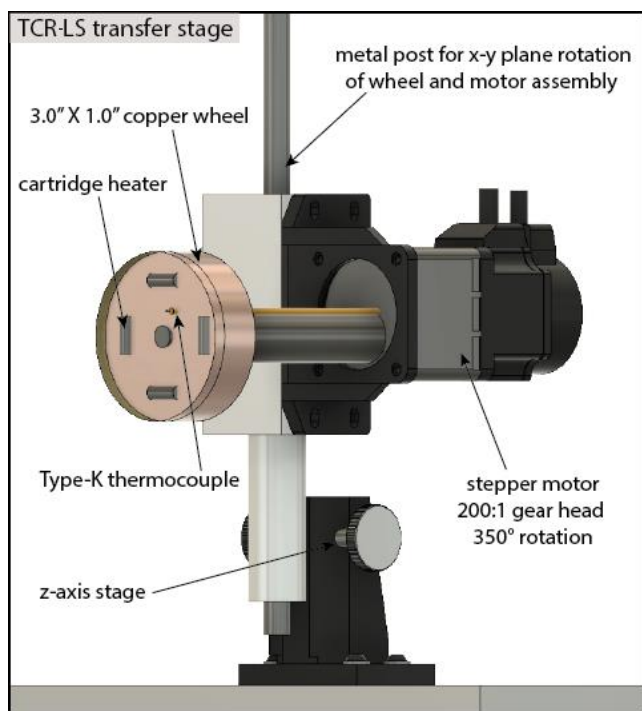
Figure S.B.1. CAD schematic of thermally controlled rotary transfer stage design, including copper wheel, cartridge heaters, Type-K thermocouple, Z-axis translation stage, and stepper motor.

Preparation of Flexible HOPG Substrate Films

In the *Experimental Methods* section of the main manuscript, we describe the preparation of flexible HOPG substrate films in detail. For a visual aid (Figure S.B.2), we have provided a

series of images highlighting the key steps for successful film preparation, along with images of how the belt appears when mounted to the copper disk of the transfer stage.
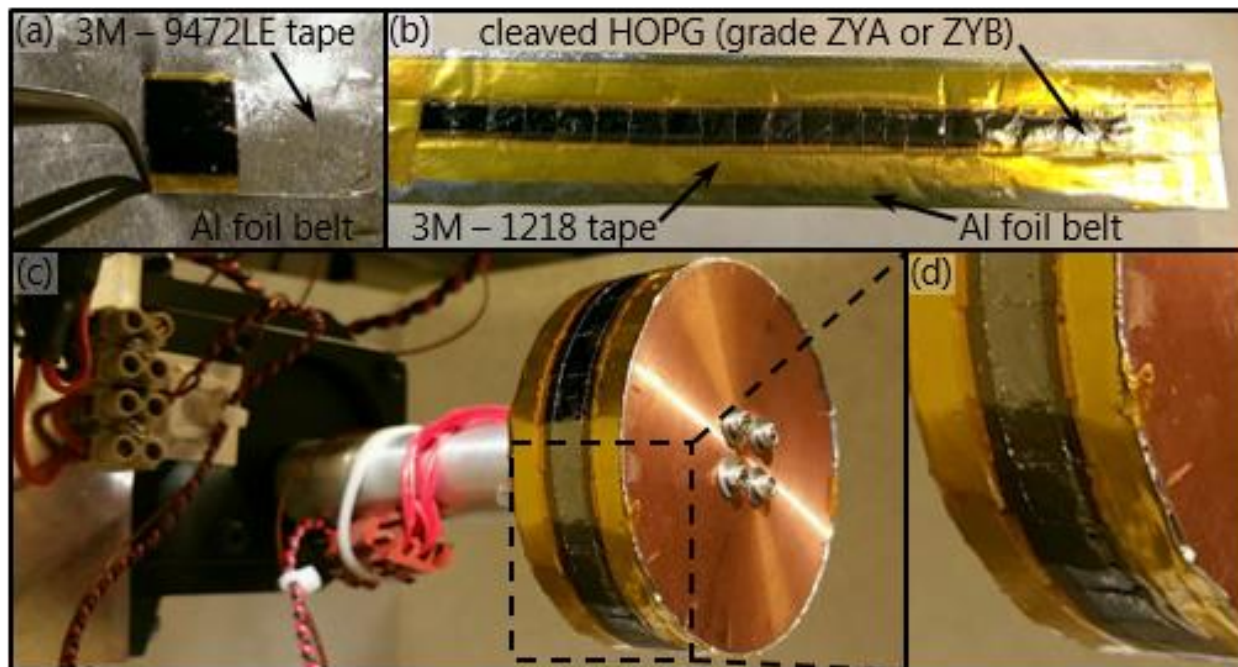
Figure S.B.2. Pliant HOPG films were prepared to accommodate the curved surface of the copper wheel. (a) HOPG cleaved with 3M 1218 high temperature single-sided polyimide tape is adhered to 3M 9472LE laminating adhesive transfer tape atop an aluminum foil belt. (b) 7.5-in film of cleaved HOPG framed by 3M 1219 tape to cover any exposed adhesive from cleaved segments. (c) Flexible HOPG film mounted to thermally controlled rotary (TCR) transfer stage. (d) Inset of (c) highlighting curvature of pliant HOPG film mounted to wheel.

Conversion of Motor Shaft Rotation Rates to Translation Rates of Flexible HOPG Films

The TCR-LS transfer stage incorporates a brushless DC motor with a 200:1 gear head and programmable driver that permits a minimum shaft speed of 0.005 RPM, corresponding to 1 RPM programmed software motor speed. Shaft rotation speeds of 0.035 RPM, 0.135 RPM and 0.270 RPM (set in the software as motor speeds of 7, 27, and 54 RPM, respectively) were utilized for the experiments described in the main manuscript. The circumference of the 3.0-in diameter copper disk is 23.9 cm; thus, the shaft rotation speeds described above lead to HOPG translation rates of 0.14 mm/s, 0.54 mm/s, and 1.10 mm/s, respectively. These translation rates produce HOPG/Langmuir film contact times of 4.0 min, 1.0 min, or 0.5 min, based on an average distance of 33 mm between advancing and receding edges of the HOPG–subphase contact meniscus.

Image Analysis

Prior to any quantitative digital image analysis, all images were processed with Gwyddion SPM software (http://gwyddion.net). All raw data files (*e.g.* AFM, SEM, and TEM) were subjected to data leveling by mean plane subtraction. Additional row alignment processing by fitting to 5th degree polynomial for AFM raw data files, matching for SEM raw data files, and median for raw TEM image files was performed. Finally, AFM raw data files were subjected to horizontal scar correction processing.

Surface coverage quantification and molecular domain size analysis was achieved using representative SEM images collected from three discrete locations within each of the following five zones along the HOPG film: 10–20 mm, 40–50 mm, 70–80 mm, 100–110 mm, and 130–140 mm. Analysis was performed using the Java-based image processing program ImageJ (NIH, Bethesda, MD). See respective sections of Appendix B below for more details.

Surface Coverage Quantification of Diyne PE Thin Films Transferred via TCR–LS Conversion

Surface coverage in each image set was determined by masking unfunctionalized areas within each image via color thresholding in ImageJ. The large range of length scales encompassed by each image, and relatively small differences in contrast associated with domain edges, in some cases necessitated manual identification of unfunctionalized regions. The fraction of masked pixels in each image was then calculated and subtracted from the total number of pixels to yield the fractional surface coverage within each image, which was tabulated and graphed in Figure 3.4d in the main manuscript. Both unmasked and masked images are included below (Figures S.B.3-S.B.8) for visual comparison.
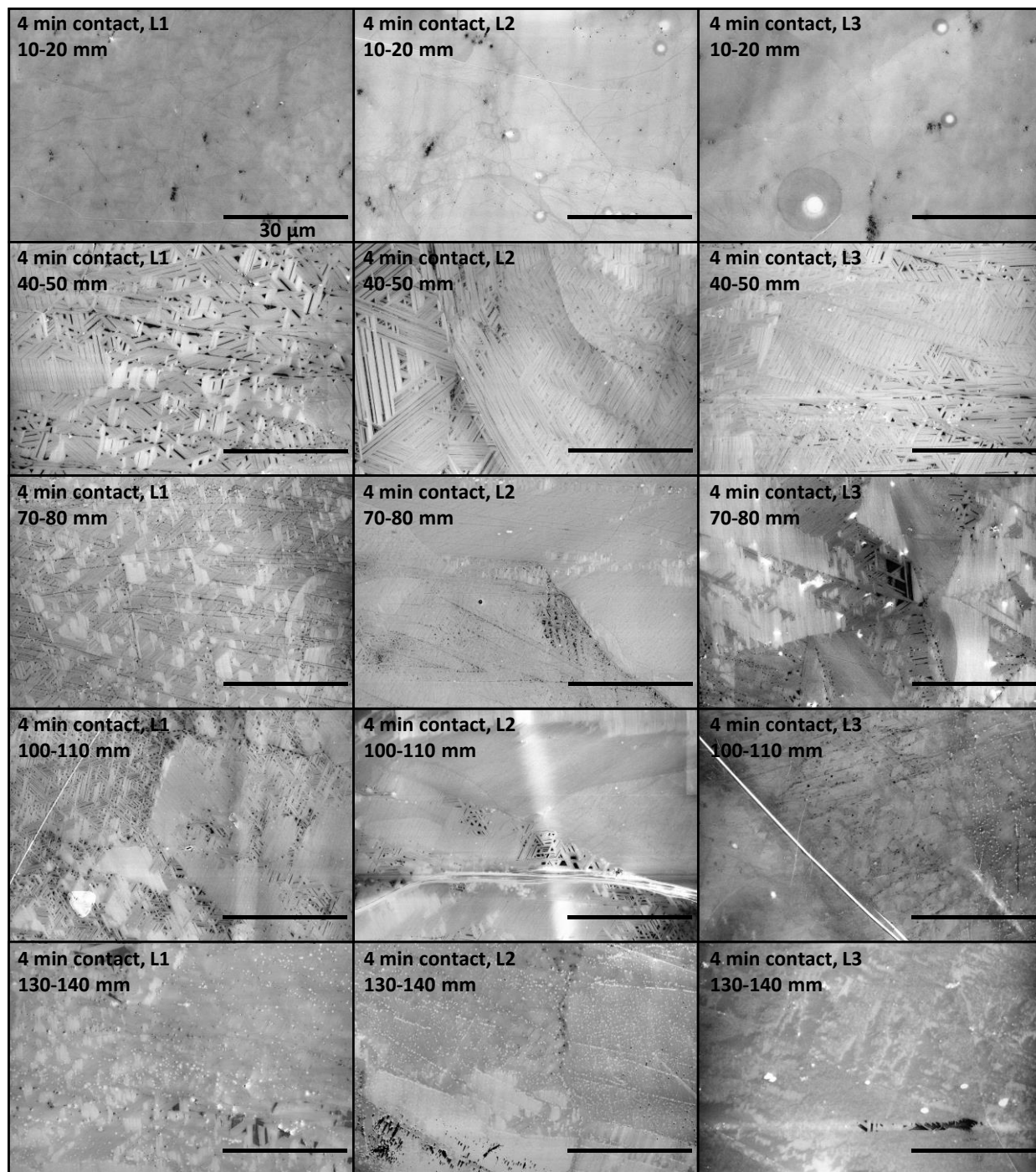
Figure S.B.3. Unmasked SEM images of diyne PE transferred to flexible HOPG film with 4 min contact time (translation rate of 0.14 mm/s), in regions 10–20 mm, 40–50 mm, 70–80 mm, 100–110 mm, or 130–140 mm from the leading edge of the HOPG film. Three regions (indicated as L1–L3 in the images above) were captured in each region of the film. Scale bar is 30 μm.

Figure S.B.4. Masked SEM images of diyne PE transferred to flexible HOPG film with 4 min contact time (translation rate of 0.14 mm/s), in regions 10–20 mm, 40–50 mm, 70–80 mm, 100–110 mm, or 130–140 mm from the leading edge of the HOPG film. Three regions (indicated as L1–L3 in the images above) were captured in each region of the film. Masked area (red) was used to quantify unfunctionalized surface area in each image. Scale bar is 30 μm.
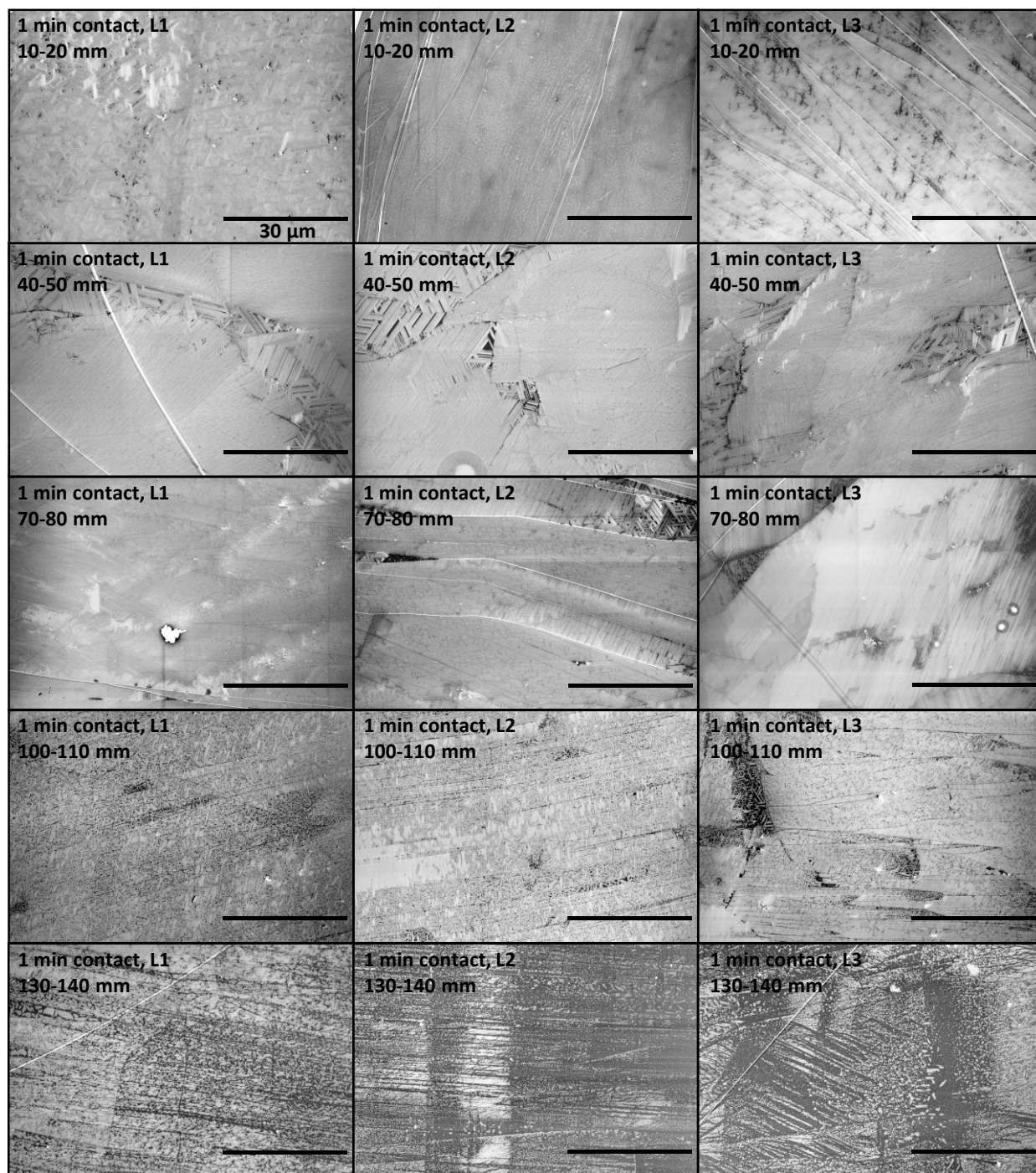
Figure S.B.5. Unmasked SEM images of diyne PE transferred to flexible HOPG film with 1 min contact time (translation rate of 0.54 mm/s), in regions 10–20 mm, 40–50 mm, 70–80 mm, 100–110 mm, or 130–140 mm from the leading edge of the HOPG film. Three regions (indicated as L1–L3 in the images above) were captured in each region of the film. Scale bar is 30 µm.
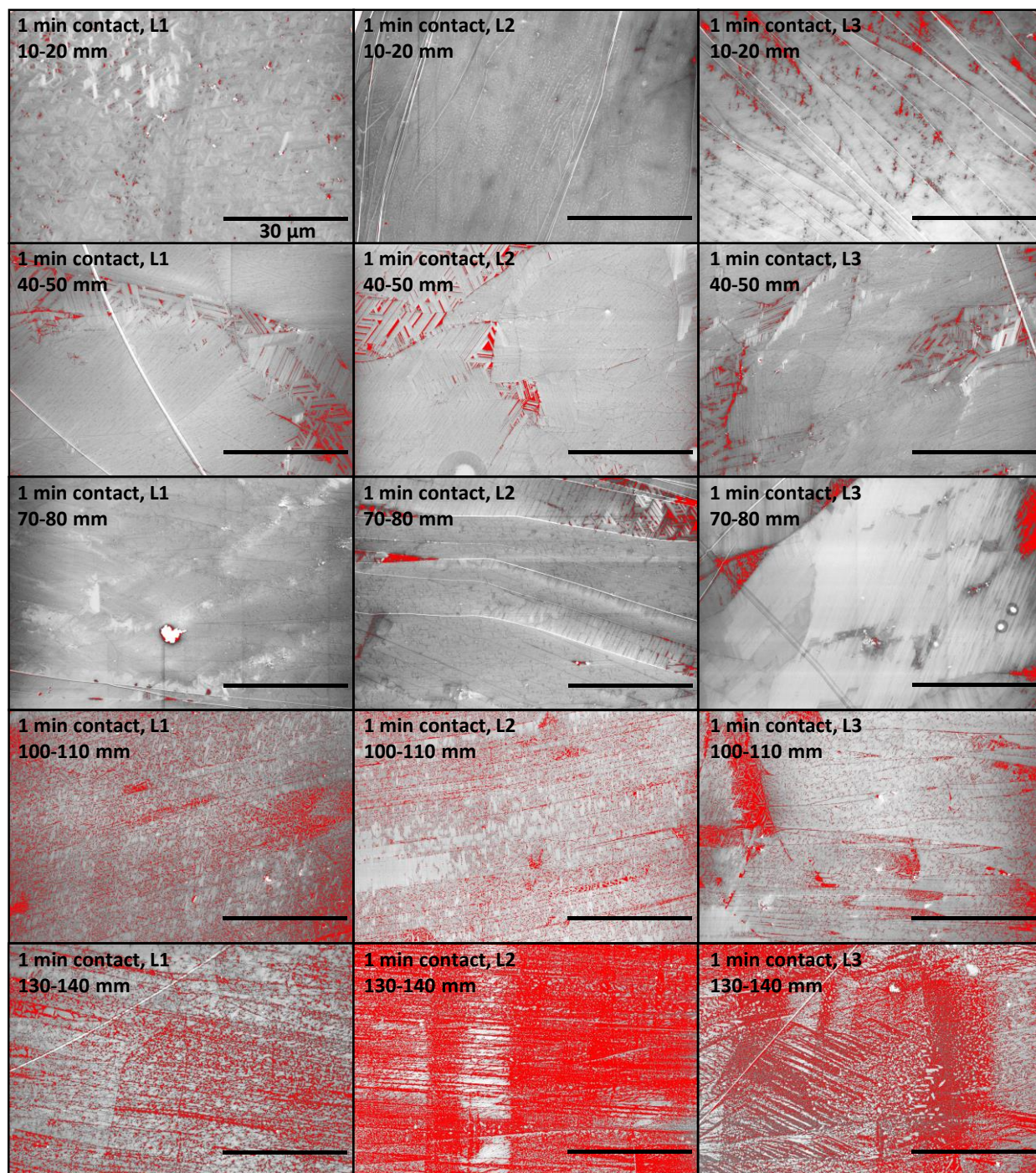
Figure S.B.6. Masked SEM images of diyne PE transferred to flexible HOPG film with 1 min contact time (translation rate of 0.54 mm/s), in regions 10–20 mm, 40–50 mm, 70–80 mm, 100–110 mm, or 130–140 mm from the leading edge of the HOPG film. Three regions (indicated as L1–L3 in the images above) were captured in each region of the film. Masked area (red) was used to quantify unfunctionalized surface area in each image. Scale bar is 30 µm.
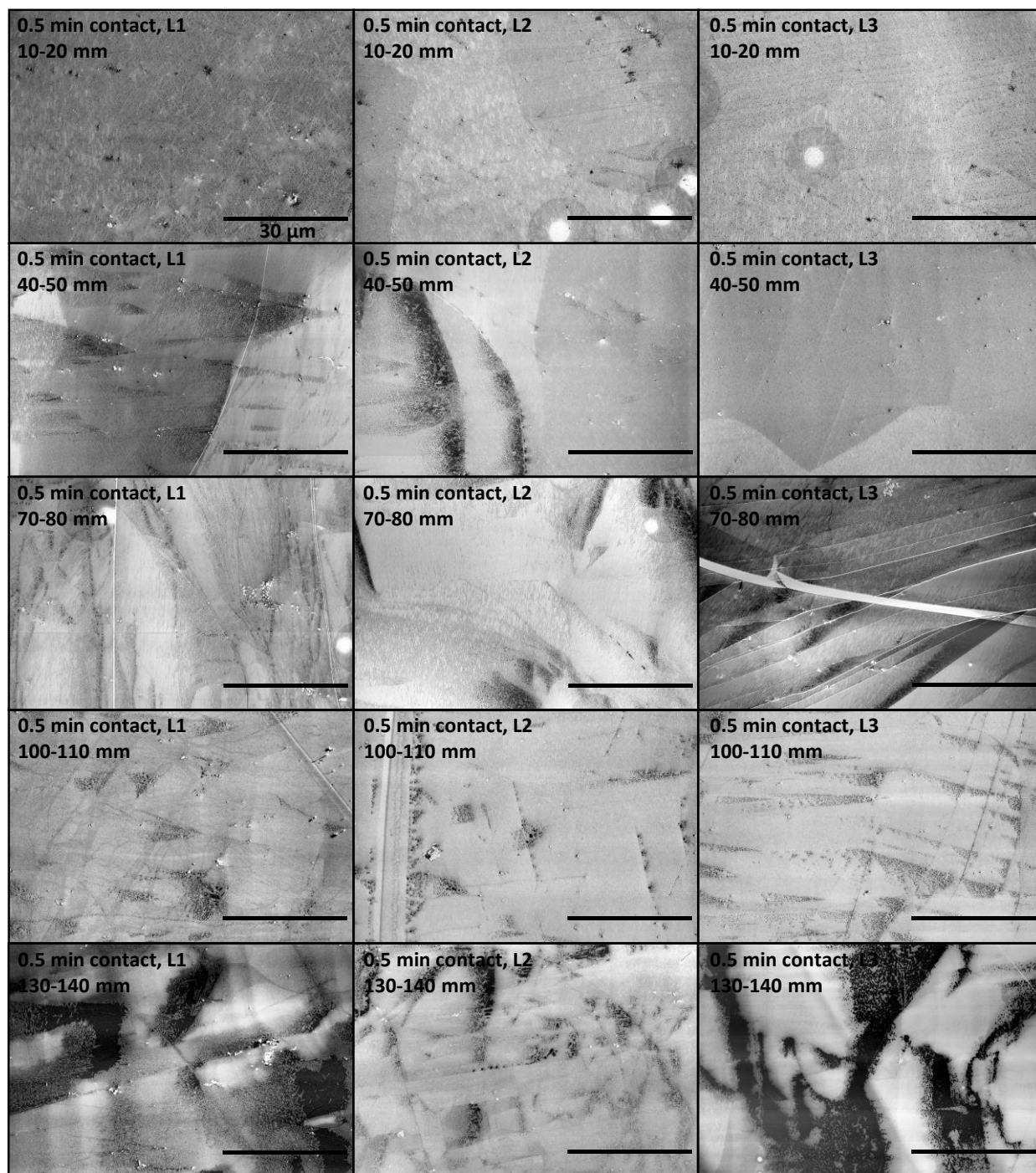
Figure S.B.7. Unmasked SEM images of diyne PE transferred to flexible HOPG film with 0.5 min contact time (translation rate of 1.10 mm/s), in regions 10–20 mm, 40–50 mm, 70–80 mm, 100–110 mm, or 130–140 mm from the leading edge of the HOPG film. Three regions (indicated as L1–L3 in the images above) were captured in each region of the film. Scale bar is 30 μm.
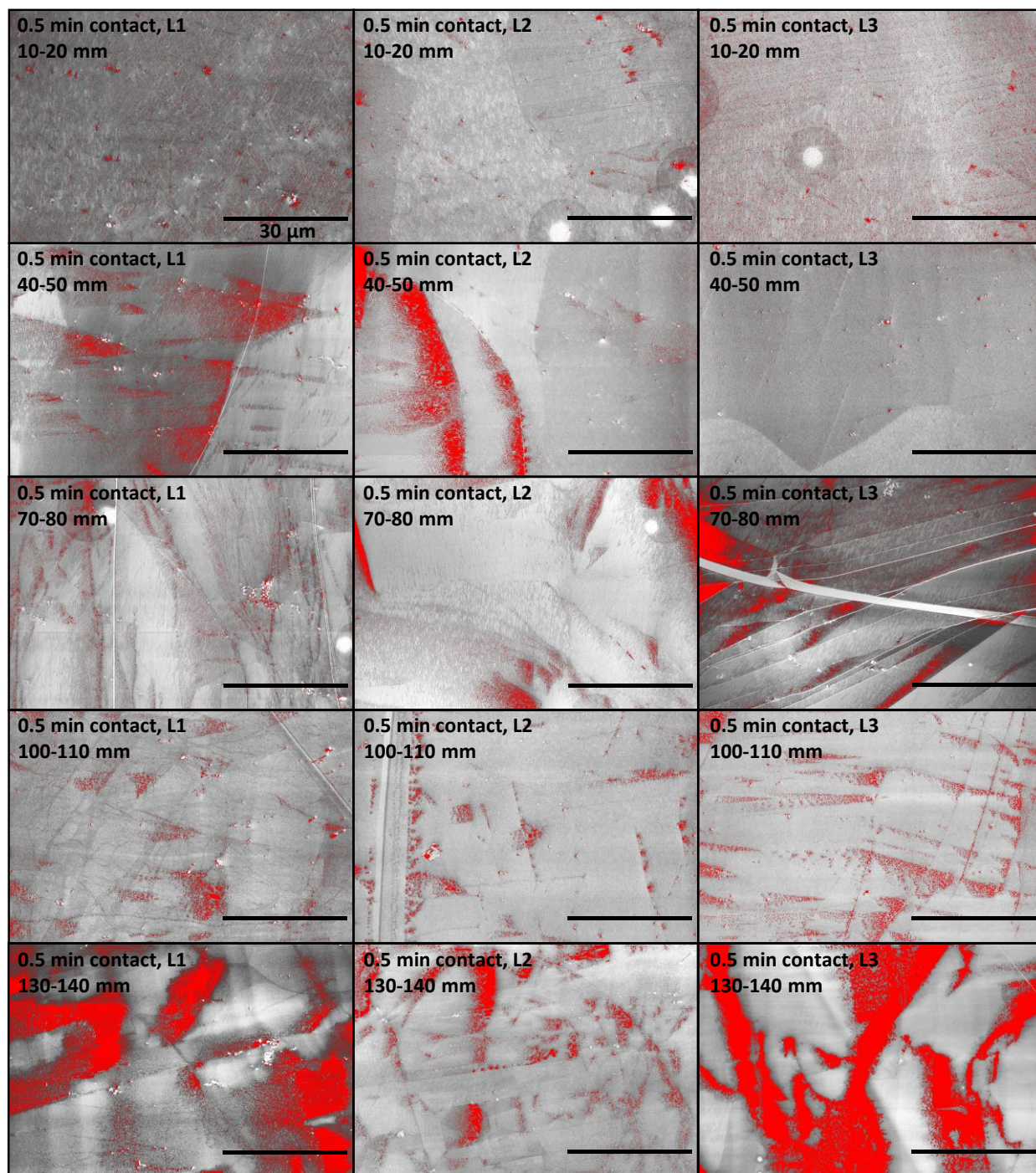
Figure S.B.8. Masked SEM images of diyne PE transferred to flexible HOPG film with 0.5 min contact time (translation rate of 1.10 mm/s), in regions 10–20 mm, 40–50 mm, 70–80 mm, 100–110 mm, or 130–140 mm from the leading edge of the HOPG film. Three regions (indicated as L1–L3 in the image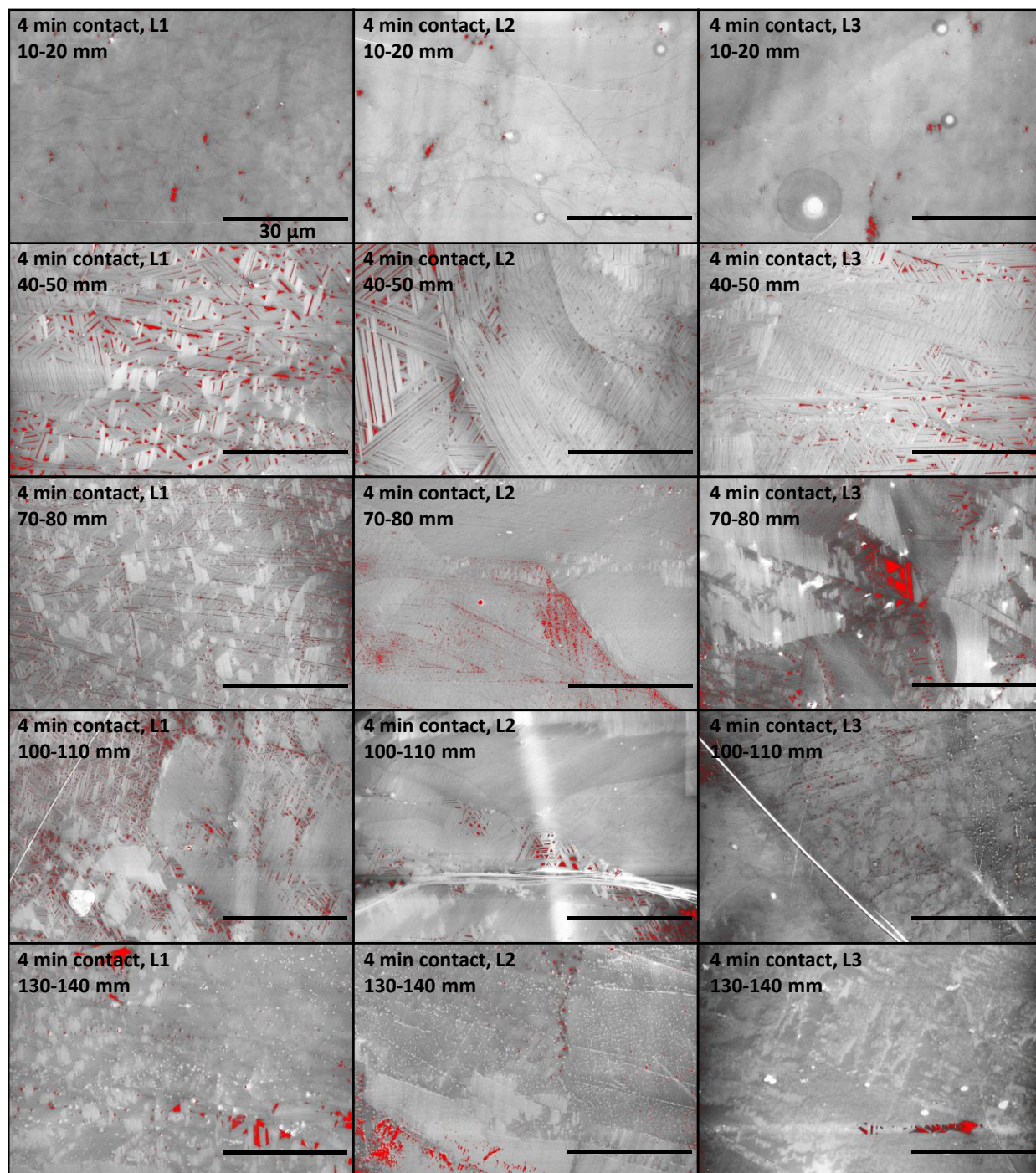s above) were captured in each region of the film. Masked area (red) was used to quantify unfunctionalized surface area in each image. Scale bar is 30 µm.

Quantifying Molecular Domain Size Distribution at Test Points Along Flexible Substrate Films

Quantification of molecular domain sizes was performed utilizing images acquired from three locations per zone (*e.g.* 10–20 mm, 40–50 mm, 70–80 mm, 100–110 mm, and 130–140 mm from the leading edge of the HOPG film) for films with translation rates of 0.14 mm/s, 0.54 mm/s, and 1.10 mm/s. Image processing was performed using ImageJ. One representative SEM image was selected at each of the three imaging locations within the five sampled regions for each of the three tested transfer speeds. In many of the representative images selected, it is evident through visual inspection that the range of domain sizes can vary by several orders of magnitude. Therefore, we segmented representative contiguous blocks of 100 domains and recorded the area (pixels^2) of each traced selection. Since large domains are of greater utility for implementation as molecular templates (*e.g.* more robust towards solvent processing due to lower domain edge contour density), the largest domain that had its entire perimeter visible in a given image was selected first – followed by manual selection of domains in a contiguous pattern outwards from domain #1 in order to capture a representative cross-section of domain sizes present (Figure S.B.9). The areas for each of the 100 domains were then converted from pixels^2 to μm^2. Histograms of quantified molecular domain sizes for translation rates of 0.14 mm/s, 0.54 mm/s, and 1.10 mm/s (contact times of 4.0 min, 1.0 min, and 0.5 min, respectively) were then compiled for the five regions along the flexible substrate film from the 300 domains recorded in each. Domains were binned by domain area, μm^2, in scaled $\log_{10}$ units of 0.2. The measured values are tabulated in histograms based on frequency (counts), as well as the percent of the total measured area (of the summed area of the 300 domains) occupied by the domains of that size.
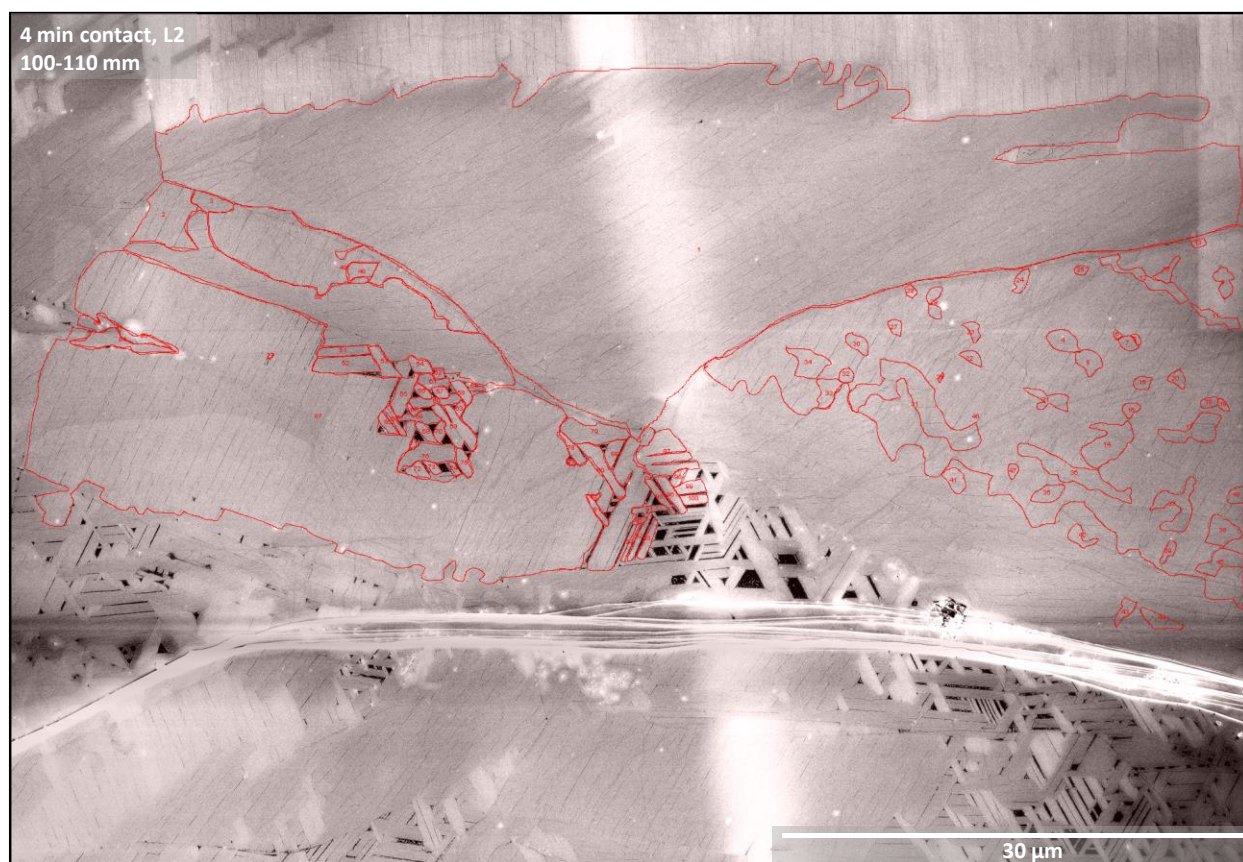
Figure S.B.9. Example of SEM image segmented in ImageJ with a contiguous block of 100 domains capturing a representative cross-section of domain sizes present, sampled outwards from the largest visible domain (*i.e.* domain #1). The segmented SEM image in this figure is diyne PE transferred to flexible HOPG film with a translation rate of 0.14 mm/s (4.0 min contact time) from location 2 (L2) of the test point region 100–110 mm from the leading edge of the HOPG film.

AuNW Synthetic Protocol

The synthetic procedure[130] outlined below, was previously adapted from literature[131-134] by our group to grow AuNWs for subsequent transfer to noncovalently adsorbed monolayers of photopolymerizable amphiphiles on 2D materials. To generate adequate growth solution for roller transfer of AuNWs to TCR–LS transferred diyne PE monolayer films, two identical reactions were carried out in the following manner: Molecular sieves were added to a mixture containing 2.5 mg of $HAuCl_4 \cdot 3H_2O$ and 2.2 mL of dry cyclohexane at ambient temperature. Oleylamine (84 µL) was added and the reaction and was briefly agitated using a vortex mixer. Next, triisopropylsilane (120 µL) was added, and the solution was promptly sealed and mixed again. The reaction mixture was then transferred to a humidity-controlled environment to age at

ambient temperature for 14.5 h. After aging, the two reaction mixtures were combined and then diluted by a factor of 34 with dry cyclohexane to reach a final volume of 100 mL.

Long-Range Sequential Rotary Transfer of AuNWs to TCR–LS Converted Diyne PE Monolayer Films

In the *Results and Discussion* section of the main manuscript, we highlight the practical utility of TCR–LS conversion in the sequential buildup of more complex film interfaces through sequential transfer cycles. Here, we show the transfer of AuNWs to the striped surface templates of TCR–LS converted diyne PE along the entire length of the substrate belt (Figure S.B.10
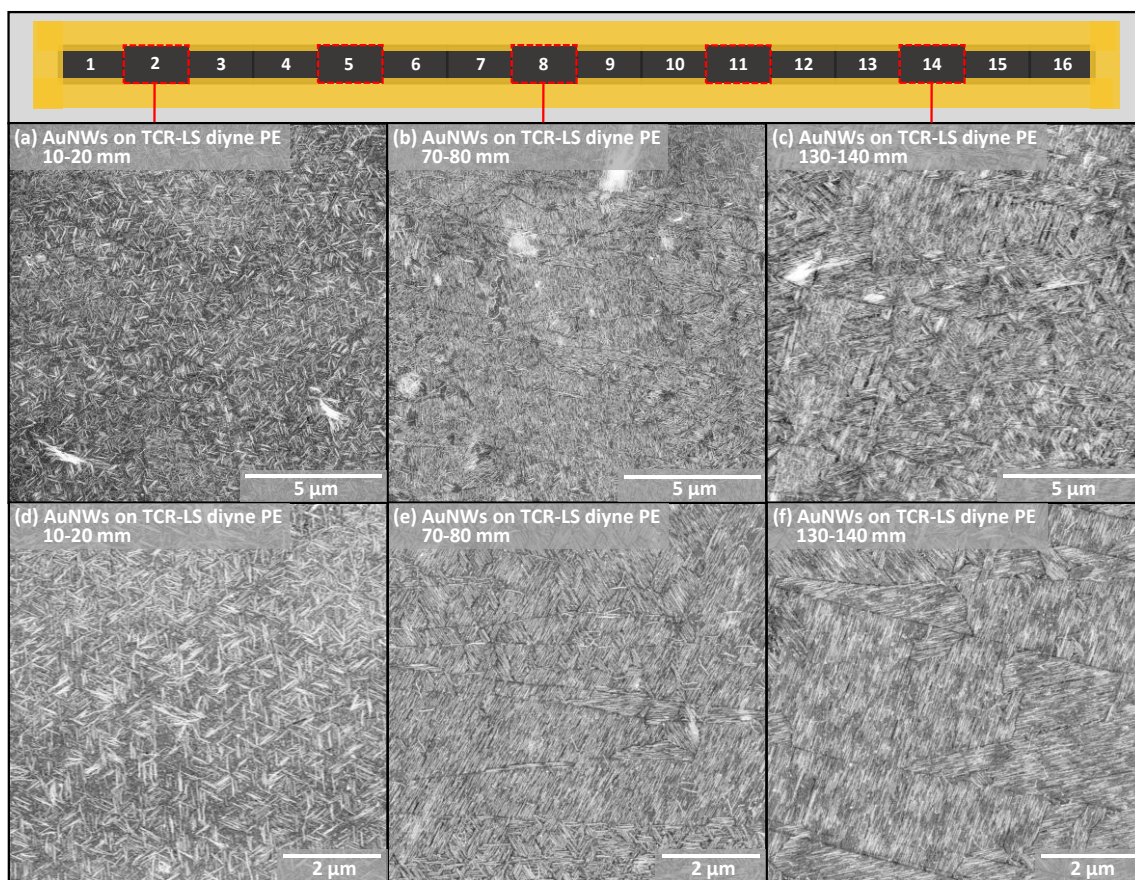
Figure S.B.10. SEM images of AuNWs on TCR–LS diyne PE (TCR–LS conditions: 38 mN/m surface pressure, 0.28 mm/s, 83 ± 3 °C heated transfer stage) translated at 0.02 mm/s through AuNW growth solution at room temperature. (a,d) AuNWs on TCR–LS diyne PE at 10–20 mm test point along film. (b,e) AuNWs on TCR–LS diyne PE at 70–80 mm test point along film. AuNW alignment over large domains is pronounced. (c,f) AuNWs on TCR–LS diyne PE at 130–140 mm test point along film. AuNW alignment and surface density over large domains is nearly identical with (b,e) at 70–80 mm region demonstrating consistency of AuNW transfer along fil

REFERENCES

1. Novoselov, K. S.; Geim, A. K.; Morozov, S. V.; Jiang, D.; Zhang, Y.; Dubonos, S. V.; Grigorieva, I. V.; Firsov, A. A., Electric field effect in atomically thin carbon films. *Science* **2004,** *306* (5696), 666-669.

2. Geim, A. K.; Novoselov, K. S., The rise of graphene. *Nat. Mater.* **2007,** *6* (3), 183-191.

3. Zhang, H., Ultrathin Two-Dimensional Nanomaterials. *ACS Nano* **2015,** *9* (10), 9451-9469.

4. Tan, C. L.; Cao, X. H.; Wu, X. J.; He, Q. Y.; Yang, J.; Zhang, X.; Chen, J. Z.; Zhao, W.; Han, S. K.; Nam, G. H.; Sindoro, M.; Zhang, H., Recent Advances in Ultrathin Two-Dimensional Nanomaterials. *Chem. Rev.* **2017,** *117* (9), 6225-6331.

5. Zhang, Y. B.; Tan, Y. W.; Stormer, H. L.; Kim, P., Experimental observation of the quantum Hall effect and Berry's phase in graphene. *Nature* **2005,** *438* (7065), 201-204.

6. Stoller, M. D.; Park, S. J.; Zhu, Y. W.; An, J. H.; Ruoff, R. S., Graphene-Based Ultracapacitors. *Nano Letters* **2008,** *8* (10), 3498-3502.

7. Lee, C.; Wei, X. D.; Kysar, J. W.; Hone, J., Measurement of the elastic properties and intrinsic strength of monolayer graphene. *Science* **2008,** *321* (5887), 385-388.

8. Nair, R. R.; Blake, P.; Grigorenko, A. N.; Novoselov, K. S.; Booth, T. J.; Stauber, T.; Peres, N. M. R.; Geim, A. K., Fine structure constant defines visual transparency of graphene. *Science* **2008,** *320* (5881), 1308-1308.

9. Balandin, A. A.; Ghosh, S.; Bao, W. Z.; Calizo, I.; Teweldebrhan, D.; Miao, F.; Lau, C. N., Superior thermal conductivity of single-layer graphene. *Nano Letters* **2008,** *8* (3), 902-907.

10. Novoselov, K. S.; Jiang, D.; Schedin, F.; Booth, T. J.; Khotkevich, V. V.; Morozov, S. V.; Geim, A. K., Two-dimensional atomic crystals. *Proceedings of the National Academy of Sciences of the United States of America* **2005,** *102* (30), 10451-10453.

11. Huang, X.; Zeng, Z. Y.; Zhang, H., Metal dichalcogenide nanosheets: preparation, properties and applications. *Chem. Soc. Rev.* **2013,** *42* (5), 1934-1946.

12. Chhowalla, M.; Shin, H. S.; Eda, G.; Li, L. J.; Loh, K. P.; Zhang, H., The chemistry of two-dimensional layered transition metal dichalcogenide nanosheets. *Nat. Chem.* **2013,** *5* (4), 263-275.

13. Lin, Y.; Williams, T. V.; Connell, J. W., Soluble, Exfoliated Hexagonal Boron Nitride Nanosheets. *J. Phys. Chem. Lett.* **2010,** *1* (1), 277-283.

14. Liu, H.; Du, Y. C.; Deng, Y. X.; Ye, P. D., Semiconducting black phosphorus: synthesis, transport properties and electronic applications. *Chem. Soc. Rev.* **2015,** *44* (9), 2732-2743.

15. Butler, S. Z.; Hollen, S. M.; Cao, L.; Cui, Y.; Gupta, J. A.; Gutierrez, H. R.; Heinz, T. F.; Hong, S. S.; Huang, J.; Ismach, A. F.; Johnston-Halperin, E.; Kuno, M.; Plashnitsa, V. V.; Robinson, R. D.; Ruoff, R. S.; Salahuddin, S.; Shan, J.; Shi, L.; Spencer, M. G.; Terrones, M.; Windl, W.; Goldberger, J. E., Progress, Challenges, and Opportunities in Two-Dimensional Materials Beyond Graphene. *ACS Nano* **2013,** *7* (4), 2898-2926.

16. Podzorov, V.; Gershenson, M. E.; Kloc, C.; Zeis, R.; Bucher, E., High-mobility field-effect transistors based on transition metal dichalcogenides. *Applied Physics Letters* **2004,** *84* (17), 3301-3303.

17. Avouris, P.; Chen, Z. H.; Perebeinos, V., Carbon-based electronics. *Nat. Nanotechnol.* **2007,** *2* (10), 605-615.

18. Schwierz, F., Graphene transistors. *Nat. Nanotechnol.* **2010,** *5* (7), 487-496.

19. Radisavljevic, B.; Radenovic, A.; Brivio, J.; Giacometti, V.; Kis, A., Single-layer MoS2 transistors. *Nat. Nanotechnol.* **2011,** *6* (3), 147-150.

20. Kim, S. J.; Choi, K.; Lee, B.; Kim, Y.; Hong, B. H., Materials for Flexible, Stretchable Electronics: Graphene and 2D Materials. In *Annual Review of Materials Research, Vol 45*, Clarke, D. R., Ed. Annual Reviews: Palo Alto, 2015; Vol. 45, pp 63-84.

21. Wang, Q. H.; Kalantar-Zadeh, K.; Kis, A.; Coleman, J. N.; Strano, M. S., Electronics and optoelectronics of two-dimensional transition metal dichalcogenides. *Nat. Nanotechnol.* **2012,** *7* (11), 699-712.

22. Wang, X.; Zhi, L. J.; Mullen, K., Transparent, conductive graphene electrodes for dye-sensitized solar cells. *Nano Letters* **2008,** *8* (1), 323-327.

23. Schedin, F.; Geim, A. K.; Morozov, S. V.; Hill, E. W.; Blake, P.; Katsnelson, M. I.; Novoselov, K. S., Detection of individual gas molecules adsorbed on graphene. *Nat. Mater.* **2007,** *6* (9), 652-655.

24. Fowler, J. D.; Allen, M. J.; Tung, V. C.; Yang, Y.; Kaner, R. B.; Weiller, B. H., Practical Chemical Sensors from Chemically Derived Graphene. *ACS Nano* **2009,** *3* (2), 301-306.

25. He, Q. Y.; Zeng, Z. Y.; Yin, Z. Y.; Li, H.; Wu, S. X.; Huang, X.; Zhang, H., Fabrication of Flexible MoS2 Thin-Film Transistor Arrays for Practical Gas-Sensing Applications. *Small* **2012,** *8* (19), 2994-2999.

26. Biswas, A.; Bayer, I. S.; Biris, A. S.; Wang, T.; Dervishi, E.; Faupel, F., Advances in top-down and bottom-up surface nanofabrication: Techniques, applications & future prospects. *Adv. Colloid Interface Sci.* **2012,** *170* (1-2), 2-27.

27. Chou, S. Y.; Krauss, P. R.; Zhang, W.; Guo, L. J.; Zhuang, L., Sub-10 nm imprint lithography and applications. *Journal of Vacuum Science & Technology B* **1997,** *15* (6), 2897-2904.

28. Vieu, C.; Carcenac, F.; Pepin, A.; Chen, Y.; Mejias, M.; Lebib, A.; Manin-Ferlazzo, L.; Couraud, L.; Launois, H., Electron beam lithography: resolution limits and applications. *Appl. Surf. Sci.* **2000,** *164*, 111-117.

29. Li, L.; Liu, X.; Pal, S.; Wang, S. L.; Ober, C. K.; Giannelis, E. P., Extreme ultraviolet resist materials for sub-7 nm patterning. *Chem. Soc. Rev.* **2017,** *46* (16), 4855-4866.

30. Kim, C. H.; Kymissis, I., Graphene-organic hybrid electronics. *J. Mater. Chem. C* **2017,** *5* (19), 4598-4613.

31. Jariwala, D.; Howell, S. L.; Chen, K. S.; Kang, J. M.; Sangwan, V. K.; Filippone, S. A.; Turrisi, R.; Marks, T. J.; Lauhon, L. J.; Hersam, M. C., Hybrid, Gate-Tunable, van der Waals p-n Heterojunctions from Pentacene and MoS2. *Nano Letters* **2016,** *16* (1), 497-503.

32. Jariwala, D.; Davoyan, A. R.; Wong, J.; Atwater, H. A., Van der Waals Materials for Atomically-Thin Photovoltaics: Promise and Outlook. *Acs Photonics* **2017,** *4* (12), 2962-2970.

33. Shen, W.; Yu, Y. Q.; Shu, J. N.; Cui, H., A graphene-based composite material noncovalently functionalized with a chemiluminescence reagent: synthesis and intrinsic chemiluminescence activity. *Chem. Commun.* **2012,** *48* (23), 2894-2896.

34. Yin, P. T.; Shah, S.; Chhowalla, M.; Lee, K. B., Design, Synthesis, and Characterization of Graphene-Nanoparticle Hybrid Materials for Bioapplications. *Chem. Rev.* **2015,** *115* (7), 2483-2531.

35. Mann, J. A.; Dichtel, W. R., Noncovalent Functionalization of Graphene by Molecular and Polymeric Adsorbates. *J. Phys. Chem. Lett.* **2013,** *4* (16), 2649-2657.

36. MacLeod, J. M.; Rosei, F., Molecular Self-Assembly on Graphene. *Small* **2014,** *10* (6), 1038-1049.

37. Stergiou, A.; Tagmatarchis, N., Molecular Functionalization of Two-Dimensional MoS2 Nanosheets. *Chem. Eur. J.* **2018,** *24* (69), 18246-18257.

38. Abellan, G.; Lloret, V.; Mundloch, U.; Marcia, M.; Neiss, C.; Gorling, A.; Varela, M.; Hauke, F.; Hirsch, A., Noncovalent Functionalization of Black Phosphorus. *Angew. Chem. Int. Ed.* **2016,** *55* (47), 14557-14562.

39. Rabe, J. P.; Buchholz, S., Commensurability and Mobility in Two-Dimensional Molecular Patterns on Graphite. *Science* **1991,** *253* (5018), 424-427.

40. Mali, K. S.; Pearce, N.; De Feyter, S.; Champness, N. R., Frontiers of supramolecular chemistry at solid surfaces. *Chem. Soc. Rev.* **2017,** *46* (9), 2520-2542.

41. Cai, B.; Zhang, S. L.; Yan, Z.; Zeng, H. B., Noncovalent Molecular Doping of Two-Dimensional Materials. *ChemNanoMat* **2015,** *1* (8), 542-557.

42. Hoeben, F. J. M.; Jonkheijm, P.; Meijer, E. W.; Schenning, A., About supramolecular assemblies of pi-conjugated systems. *Chem. Rev.* **2005,** *105* (4), 1491-1546.

43. Georgakilas, V.; Tiwari, J. N.; Kemp, K. C.; Perman, J. A.; Bourlinos, A. B.; Kim, K. S.; Zboril, R., Noncovalent Functionalization of Graphene and Graphene Oxide for Energy Materials, Biosensing, Catalytic, and Biomedical Applications. *Chem. Rev.* **2016,** *116* (9), 5464-5519.

44. Toth, P. S.; Velicky, M.; Ramasse, Q. M.; Kepaptsoglou, D. M.; Dryfe, R. A. W., Symmetric and Asymmetric Decoration of Graphene: Bimetal-Graphene Sandwiches. *Adv. Funct. Mater.* **2015,** *25* (19), 2899-2909.

45. Groszek, A. J., Preferential Adsorption of Long-Chain Normal Paraffins on MoS_2 WS_2 and Graphite from N-Heptane. *Nature* **1964,** *204* (495), 680-&.

46. McGonigal, G. C.; Bernhardt, R. H.; Thomson, D. J., Imaging Alkane Layers at the Liquid Graphite Interface with the Scanning Tunneling Microscope. *Applied Physics Letters* **1990,** *57* (1), 28-30.

47. Rabe, J. P.; Buchholz, S., Commensurability and Mobility in 2-Dimensional Molecular-Patterns on Graphite. *Science* **1991,** *253* (5018), 424-427.

48. Grim, P. C. M.; De Feyter, S.; Gesquiere, A.; Vanoppen, P.; Rucker, M.; Valiyaveettil, S.; Moessner, G.; Mullen, K.; De Schryver, F. C., Submolecularly resolved polymerization of diacetylene molecules on the graphite surface observed with scanning tunneling microscopy. *Angew. Chem. Int. Ed.* **1997,** *36* (23), 2601-2603.

49. Samori, P.; Fechtenkotter, A.; Jackel, F.; Bohme, T.; Mullen, K.; Rabe, J. P., Supramolecular staircase via self-assembly of disklike molecules at the solid-liquid interface. *J. Am. Chem. Soc.* **2001,** *123* (46), 11462-11467.

50. Okawa, Y.; Aono, M., Materials science - Nanoscale control of chain polymerization. *Nature* **2001,** *409* (6821), 683-684.

51. Deshpande, A.; Sham, C.-H.; Alaboson, J. M. P.; Mullin, J. M.; Schatz, G. C.; Hersam, M. C., Self-Assembly and Photopolymerization of Sub-2 nm One-Dimensional Organic Nanostructures on Graphene. *J. Am. Chem. Soc.* **2012,** *134* (40), 16759-16764.

52. Giridharagopal, R.; Kelly, K. F., Substrate-dependent properties of polydiacetylene nanowires on graphite and MoS2. *ACS Nano* **2008,** *2* (8), 1571-1580.

53. Okawa, Y.; Mandal, S. K.; Hu, C.; Tateyama, Y.; Goedecker, S.; Tsukamoto, S.; Hasegawa, T.; Gimzewski, J. K.; Aono, M., Chemical Wiring and Soldering toward All-Molecule Electronic Circuitry. *J. Am. Chem. Soc.* **2011,** *133* (21), 8227-8233.

54. Okawa, Y.; Takajo, D.; Tsukamoto, S.; Hasegawa, T.; Aono, M., Atomic force microscopy and theoretical investigation of the lifted-up conformation of polydiacetylene on a graphite substrate. *Soft Matter* **2008,** *4* (5), 1041-1047.

55. Okawa, Y.; Aono, M., Linear chain polymerization initiated by a scanning tunneling microscope tip at designated positions. *J. Chem. Phys.* **2001,** *115* (5), 2317-2322.

56. Bang, J. J.; Rupp, K. K.; Russell, S. R.; Choong, S. W.; Claridge, S. A., Sitting Phases of Polymerizable Amphiphiles for Controlled Functionalization of Layered Materials. *J. Am. Chem. Soc.* **2016,** *138* (13), 4448-4457.

57. Claridge, S. A., Standing, lying, and sitting: translating building principles of the cell membrane to synthetic 2D material interfaces. *Chem. Commun.* **2018,** *54* (50), 6681-6691.

58. Yang, Y.; Zimmt, M. B., Shape Amphiphiles in 2-D: Assembly of 1-D Stripes and Control of Their Surface Density. *J. Phys. Chem. B* **2015,** *119* (24), 7740-7748.

59. He, J.; Myerson, K. J.; Zimmt, M. B., Zipping and unzipping monolayers: switchable monolayer oligomerization and adhesion via thiol-disulfide interconversion. *Chem. Commun.* **2018,** *54* (29), 3636-3639.

60. Lee, S. L.; Yuan, Z. Y.; Chen, L.; Mali, K. S.; Mullen, K.; De Feyter, S., Forced To Align: Flow-Induced Long-Range Alignment of Hierarchical Molecular Assemblies from 2D to 3D. *J. Am. Chem. Soc.* **2014,** *136* (11), 4117-4120.

61. Lee, S. L.; Yuan, Z. Y.; Chen, L.; Mali, K. S.; Muellen, K.; De Feyter, S., Flow-Assisted 2D Polymorph Selection: Stabilizing Metastable Monolayers at the Liquid-Solid Interface. *J. Am. Chem. Soc.* **2014,** *136* (21), 7595-7598.

62. Lee, S. L.; Chi, C. Y. J.; Huang, M. J.; Chen, C. H.; Li, C. W.; Pati, K.; Liu, R. S., Shear-induced long-range uniaxial assembly of polyaromatic monolayers at molecular resolution. *J. Am. Chem. Soc.* **2008,** *130* (32), 10454-10455.

63. Davis, T. C.; Bang, J. J.; Brooks, J. T.; McMillan, D. G.; Claridge, S. A., Hierarchically Patterned Noncovalent Functionalization of 2D Materials by Controlled Langmuir-Schaefer Conversion. *Langmuir* **2018,** *34* (4), 1353-1362.

64. Chen, X. D.; Lenhert, S.; Hirtz, M.; Lu, N.; Fuchs, H.; Chi, L. F., Langmuir-Blodgett patterning: A bottom-up way to build mesostructures over large areas. *Acc. Chem. Res.* **2007,** *40* (6), 393-401.

65. Blodgett, K. B., Monomolecular films of fatty acids on glass. *J. Am. Chem. Soc.* **1934,** *56*, 495-495.

66. Blodgett, K. B.; Langmuir, I., Built-up films of barium stearate and their optical properties. *Phys. Rev.* **1937,** *51* (11), 0964-0982.

67. Langmuir, I.; Schaefer, V. J., Activities of urease and pepsin monolayers. *J. Am. Chem. Soc.* **1938,** *60*, 1351-1360.

68. Zasadzinski, J. A.; Viswanathan, R.; Madsen, L.; Garnaes, J.; Schwartz, D. K., Langmuir-Blodgett Films. *Science* **1994,** *263* (5154), 1726-1733.

69.   Villarreal, T. A.; Russell, S. R.; Bang, J. J.; Patterson, J. K.; Claridge, S. A., Modulating Wettability of Layered Materials by Controlling Ligand Polar Headgroup Dynamics. *J. Am. Chem. Soc.* **2017,** *139* (34), 11973-11979.

70.   Davis, T. C.; Russell, S. R.; Claridge, S. A., Edge-on adsorption of multi-chain functional alkanes stabilizes noncovalent monolayers on MoS$_2$. *Chem. Commun.* **2018,** *54* (83), 11709-11712.

71.   Zhang, G. M.; Kuwahara, Y.; Wu, J. W.; Horie, Y.; Matsunaga, T.; Saito, A.; Aono, M., Scanning tunneling microscopy observation of Langmuir-Blodgett diacetylene compound films deposited by Schaefer's method. *Jpn. J. Appl. Phys., Part 1* **2002,** *41* (4A), 2187-2188.

72.   Giridharagopal, R.; Kelly, K. F., STM-Induced desorption of polydiacetylene nanowires and reordering via molecular cascades. *J. Phys. Chem. C* **2007,** *111* (17), 6161-6166.

73.   Butler, S. Z.; Hollen, S. M.; Cao, L. Y.; Cui, Y.; Gupta, J. A.; Gutierrez, H. R.; Heinz, T. F.; Hong, S. S.; Huang, J. X.; Ismach, A. F.; Johnston-Halperin, E.; Kuno, M.; Plashnitsa, V. V.; Robinson, R. D.; Ruoff, R. S.; Salahuddin, S.; Shan, J.; Shi, L.; Spencer, M. G.; Terrones, M.; Windl, W.; Goldberger, J. E., Progress, Challenges, and Opportunities in Two-Dimensional Materials Beyond Graphene. *ACS Nano* **2013,** *7* (4), 2898-2926.

74.   Huang, X.; Qi, X.; Boey, F.; Zhang, H., Graphene-based composites. *Chem. Soc. Rev.* **2012,** *41* (2), 666-686.

75.   De Feyter, S.; De Schryver, F. C., Two-dimensional supramolecular self-assembly probed by scanning tunneling microscopy. *Chem. Soc. Rev.* **2003,** *32* (3), 139-150.

76.   Mali, K. S.; Greenwood, J.; Adisoejoso, J.; Phillipson, R.; De Feyter, S., Nanostructuring graphene for controlled and reproducible functionalization. *Nanoscale* **2015,** *7* (5), 1566-1585.

77.   Cyr, D. M.; Venkataraman, B.; Flynn, G. W., STM investigations of organic molecules physisorbed at the liquid-solid interface. *Chem. Mat.* **1996,** *8* (8), 1600-1615.

78.   Giancarlo, L. C.; Flynn, G. W., Scanning tunneling and atomic force microscopy probes of self-assembled, physisorbed monolayers: Peeking at the peaks. *Annu. Rev. Phys. Chem.* **1998,** *49*, 297-336.

79.   Gatti, R.; MacLeod, J. M.; Lipton-Duffin, J. A.; Moiseev, A. G.; Perepichka, D. F.; Rosei, F., Substrate, Molecular Structure, and Solvent Effects in 2D Self-Assembly via Hydrogen and Halogen Bonding. *J. Phys. Chem. C* **2014,** *118* (44), 25505-25516.

80.   Georgakilas, V.; Otyepka, M.; Bourlinos, A. B.; Chandra, V.; Kim, N.; Kemp, K. C.; Hobza, P.; Zboril, R.; Kim, K. S., Functionalization of Graphene: Covalent and Non-Covalent Approaches, Derivatives and Applications. *Chem. Rev.* **2012,** *112* (11), 6156-6214.

81.   Kuila, T.; Bose, S.; Mishra, A. K.; Khanra, P.; Kim, N. H.; Lee, J. H., Chemical functionalization of graphene and its applications. *Progress in Materials Science* **2012,** *57* (7), 1061-1105.

82.   Hong, G.; Wu, Q.-H.; Ren, J.; Wang, C.; Zhang, W.; Lee, S.-T., Recent progress in organic molecule/graphene interfaces. *Nano Today* **2013,** *8* (4), 388-402.

83.   Li, B.; Klekachev, A. V.; Cantoro, M.; Huyghebaert, C.; Stesmans, A.; Asselberghs, I.; De Gendt, S.; De Feyter, S., Toward tunable doping in graphene FETs by molecular self-assembled monolayers. *Nanoscale* **2013,** *5* (20), 9640-9644.

84.   Lockhart de la Rosa, C. J.; Phillipson, R.; Teyssandier, J.; Adisoejoso, J.; Balaji, Y.; Huyghebaert, C.; Radu, I.; Heyns, M.; De Feyter, S.; De Gendt, S., Molecular doping of MoS2 transistors by self-assembled oleylamine networks. *Applied Physics Letters* **2016,** *109* (25), 253112.

85.   Phillipson, R.; de la Rosa, C. J. L.; Teyssandier, J.; Walke, P.; Waghray, D.; Fujita, Y.; Adisoejoso, J.; Mali, K. S.; Asselierghs, I.; Huyghebaert, C.; Uji-i, H.; De Gendt, S.; De Feyter, S., Tunable doping of graphene by using physisorbed self-assembled networks. *Nanoscale* **2016,** *8* (48), 20017-20026.

86.   Choong, S. W.; Russell, S. R.; Bang, J. J.; Patterson, J. K.; Claridge, S. A., Sitting Phase Monolayers of Polymerizable Phospholipids Create Dimensional, Molecular-Scale Wetting Control for Scalable Solution Based Patterning of Layered Materials. *ACS Appl. Mater. Interfaces* **2017,** *9* (22), 19326-19334.

87.   Wang, Q. H.; Hersam, M. C., Room-temperature molecular-resolution characterization of self-assembled organic monolayers on epitaxial graphene. *Nat. Chem.* **2009,** *1* (3), 206-211.

88.   Alaboson, J. M. P.; Wang, Q. H.; Emery, J. D.; Lipson, A. L.; Bedzyk, M. J.; Elam, J. W.; Pellin, M. J.; Hersam, M. C., Seeding Atomic Layer Deposition of High-k Dielectrics on Epitaxial Graphene with Organic Self-Assembled Monolayers. *ACS Nano* **2011,** *5* (6), 5223-5232.

89.   Alaboson, J. M. P.; Sham, C. H.; Kewalramani, S.; Emery, J. D.; Johns, J. E.; Deshpande, A.; Chien, T. Y.; Bedzyk, M. J.; Elam, J. W.; Pellin, M. J.; Hersam, M. C., Templating Sub-10 nm Atomic Layer Deposited Oxide Nanostructures on Graphene via One-Dimensional Organic Self-Assembled Monolayers. *Nano Letters* **2013,** *13* (12), 5763-5770.

90.   Russell, S. R.; Claridge, S. A., Peptide interfaces with graphene: an emerging intersection of analytical chemistry, theory, and materials. *Anal. Bioanal. Chem.* **2016,** *408* (11), 2649-2658.

91.   Rabe, J. P.; Buchholz, S.; Askadskaya, L., Scanning Tunneling Microscopy of Several Alkylated Molecular Moieties in Monolayers on Graphite. *Synth. Met.* **1993,** *54* (1-3), 339-349.

92. Doudevski, I.; Schwartz, D. K., Mechanisms of self-assembled monolayer desorption determined using in situ atomic force microscopy. *Langmuir* **2000,** *16* (24), 9381-9384.

93. Schlenoff, J. B.; Li, M.; Ly, H., Stability and self-exchange in alkanethiol monolayers. *J. Am. Chem. Soc.* **1995,** *117* (50), 12528-12536.

94. Love, J. C.; Estroff, L. A.; Kriebel, J. K.; Nuzzo, R. G.; Whitesides, G. M., Self-assembled monolayers of thiolates on metals as a form of nanotechnology. *Chem. Rev.* **2005,** *105* (4), 1103-1169.

95. Mohammadi, E.; Zhao, C.; Meng, Y.; Qu, G.; Zhang, F.; Zhao, X.; Mei, J.; Zuo, J.-M.; Shukla, D.; Diao, Y., Dynamic-template-directed multiscale assembly for large-area coating of highly-aligned conjugated polymer thin films. *Nat. Commun.* **2017,** *8*, 1-11.

96. Stadermann, M.; Baxamusa, S. H.; Aracne-Ruddle, C.; Chea, M.; Li, S.; Youngblood, K.; Suratwala, T., Fabrication of Large-area Free-standing Ultrathin Polymer Films. *Jove-Journal of Visualized Experiments* **2015,** (100), 1-7.

97. Jurchescu, O. D.; Baas, J.; Palstra, T. T. M., Effect of impurities on the mobility of single crystal pentacene. *Applied Physics Letters* **2004,** *84* (16), 3061-3063.

98. Shao, W.; Dong, H.; Jiang, L.; Hu, W., Morphology control for high performance organic thin film transistors. *Chemical Science* **2011,** *2* (4), 590-600.

99. Binks, B. P., Insoluble Monolayers of Weakly Ionizing Low Molar Mass Materials and Their Deposition to Form Langmuir-Blodgett Multilayers. *Adv. Colloid Interface Sci.* **1991,** *34*, 343-432.

100. Honig, E. P.; Hengst, J. H. T.; Denengel.D, Langmuir-Blodgett Deposition Ratios. *J. Colloid Interface Sci.* **1973,** *45* (1), 92-102.

101. Okawa, Y.; Akai-Kasaya, M.; Kuwahara, Y.; Mandal, S. K.; Aono, M., Controlled chain polymerisation and chemical soldering for single-molecule electronics. *Nanoscale* **2012,** *4* (10), 3013-3028.

102. Claridge, S. A.; Liao, W.-S.; Thomas, J. C.; Zhao, Y.; Cao, H. H.; Cheunkar, S.; Serino, A. C.; Andrews, A. M.; Weiss, P. S., From the bottom up: dimensional control and characterization in molecular monolayers. *Chem. Soc. Rev.* **2013,** *42* (7), 2725-2745.

103. Miura, A.; De Feyter, S.; Abdel-Mottaleb, M. M. S.; Gesquiere, A.; Grim, P. C. M.; Moessner, G.; Sieffert, M.; Klapper, M.; Mullen, K.; De Schryver, F. C., Light- and STM-tip-induced formation of one-dimensional and two-dimensional organic nanostructures. *Langmuir* **2003,** *19* (16), 6474-6482.

104. Donhauser, Z. J.; Price, D. W.; Tour, J. M.; Weiss, P. S., Control of alkanethiolate monolayer structure using vapor-phase annealing. *J. Am. Chem. Soc.* **2003,** *125* (38), 11462-11463.

105.   Poirier, G. E.; Tarlov, M. J., Molecular Ordering and Gold Migration Observed in Butanethiol Self-Assembled Monolayers Using Scanning-Tunneling-Microscopy. *J. Phys. Chem.* **1995,** *99* (27), 10966-10970.

106.   Doudevski, I.; Hayes, W. A.; Schwartz, D. K., Submonolayer island nucleation and growth kinetics during self-assembled monolayer formation. *Phys. Rev. Lett.* **1998,** *81* (22), 4927-4930.

107.   Chance, R. R.; Patel, G. N.; Turi, E. A.; Khanna, Y. P., Energetics of Thermal Polymerization of a Diacetylene Crystal. *J. Am. Chem. Soc.* **1978,** *100* (4), 1307-1309.

108.   Doudevski, I.; Schwartz, D. K., Dynamic scaling of the submonolayer island size distribution during self-assembled monolayer growth. *Phys. Rev. B* **1999,** *60* (1), 14-17.

109.   Li, Z.; Wang, Y.; Kozbial, A.; Shenoy, G.; Zhou, F.; McGinley, R.; Ireland, P.; Morganstein, B.; Kunkel, A.; Surwade, S. P.; Li, L.; Liu, H., Effect of airborne contaminants on the wettability of supported graphene and graphite. *Nat. Mater.* **2013,** *12* (10), 925-931.

110.   Kozbial, A.; Zhou, F.; Li, Z.; Liu, H.; Li, L., Are Graphitic Surfaces Hydrophobic? *Acc. Chem. Res.* **2016,** *49* (12), 2765-2773.

111.   Carpick, R. W.; Mayer, T. M.; Sasaki, D. Y.; Burns, A. R., Spectroscopic ellipsometry and fluorescence study of thermochromism in an ultrathin poly(diacetylene) film: Reversibility and transition kinetics. *Langmuir* **2000,** *16* (10), 4639-4647.

112.   Bassler, H., Photopolymerization of Diacetylenes. *Advances in Polymer Science* **1984,** *63*, 1-48.

113.   Wegner, G., Topochemical Reactions of Monomers with Conjugated Triple Bonds. I. Polymerization of 2.4-Hexadiyn-1.6-Diols Derivatives in Crystalline State. *Zeitschrift Fur Naturforschung Part B-Chemie Biochemie Biophysik Biologie Und Verwandten Gebiete* **1969,** *B 24* (7), 824-826.

114.   Maryott, A. A.; Smith, E. R., *Table of Dielectric Constants of Pure Liquids*. United States Department of Commerce, Ed.: US Government Printing Office: Washington, DC, 1951; Vol. 514, pp 1-44.

115.   Ryder, C. R.; Wood, J. D.; Wells, S. A.; Hersam, M. C., Chemically Tailoring Semiconducting Two-Dimensional Transition Metal Dichalcogenides and Black Phosphorus. *ACS Nano* **2016,** *10* (4), 3900-3917.

116.   Okawa, Y.; Mandal, S. K.; Hu, C. P.; Tateyama, Y.; Goedecker, S.; Tsukamoto, S.; Hasegawa, T.; Gimzewski, J. K.; Aono, M., Chemical Wiring and Soldering toward All-Molecule Electronic Circuitry. *J. Am. Chem. Soc.* **2011,** *133* (21), 8227-8233.

117. Hayes, T. R.; Bang, J. J.; Davis, T. C.; Peterson, C. F.; McMillan, D. G.; Claridge, S. A., Multimicrometer Noncovalent Monolayer Domains on Layered Materials through Thermally Controlled Langmuir-Schaefer Conversion for Noncovalent 2D Functionalization. *ACS Appl. Mater. Interfaces* **2017,** *9* (41), 36409-36416.

118. Zhavnerko, G.; Marletta, G., Developing Langmuir-Blodgett strategies towards practical devices. *Mater. Sci. Eng. B-Adv. Funct. Solid-State Mater.* **2010,** *169* (1-3), 43-48.

119. Li, X.; Gilchrist, J. F., Large-Area Nanoparticle Films by Continuous Automated Langmuir-Blodgett Assembly and Deposition. *Langmuir* **2016,** *32* (5), 1220-1226.

120. Parchine, M.; McGrath, J.; Bardosova, M.; Pemble, M. E., Large Area 2D and 3D Colloidal Photonic Crystals Fabricated by a Roll-to-Roll Langmuir-Blodgett Method. *Langmuir* **2016,** *32* (23), 5862-5869.

121. Parchine, M.; Kohoutek, T.; Bardosova, M.; Pemble, M. E., Large area colloidal photonic crystals for light trapping in flexible organic photovoltaic modules applied using a roll-to-roll Langmuir-Blodgett method. *Sol. Energy Mater. Sol. Cells* **2018,** *185*, 158-165.

122. Russell, S. R.; Davis, T. C.; Bang, J. J.; Claridge, S. A., Spectroscopic Metrics for Alkyl Chain Ordering in Lying-Down Noncovalent Monolayers of Diynoic Acids on Graphene. *Chem. Mat.* **2018,** *30* (8), 2506-2514.

123. Bang, J. J.; Porter, A. G.; Davis, T. C.; Hayes, T. R.; Claridge, S. A., Spatially Controlled Noncovalent Functionalization of 2D Materials Based on Molecular Architecture. *Langmuir* **2018,** *34* (19), 5454-5463.

124. Davis, T. C.; Bechtold, J. O.; Hayes, T. R.; Villarreal, T. A.; Claridge, S. A., Hierarchically patterned striped phases of polymerized lipids: toward controlled carbohydrate presentation at interfaces. *Faraday Discuss.* **2019,** *219*, 229-243.

125. Leys, C.; Ley, C.; Klein, O.; Bernard, P.; Licata, L., Detecting outliers: Do not use standard deviation around the mean, use absolute deviation around the median. *Journal of Experimental Social Psychology* **2013,** *49* (4), 764-766.

126. Burrows, N. D.; Vartanian, A. M.; Abadeer, N. S.; Grzincic, E. M.; Jacob, L. M.; Lin, W. N.; Li, J.; Dennison, J. M.; Hinman, J. G.; Murphy, C. J., Anisotropic Nanoparticles and Anisotropic Surface Chemistry. *J. Phys. Chem. Lett.* **2016,** *7* (4), 632-641.

127. Boles, M. A.; Engel, M.; Talapin, D. V., Self-Assembly of Colloidal Nanocrystals: From Intricate Structures to Functional Materials. *Chem. Rev.* **2016,** *116* (18), 11220-11289.

128. Paik, T.; Diroll, B. T.; Kagan, C. R.; Murray, C. B., Binary and Ternary Superlattices Self-Assembled from Colloidal Nanodisks and Nanorods. *J. Am. Chem. Soc.* **2015,** *137* (20), 6662-6669.

129. Shevchenko, E. V.; Talapin, D. V.; Kotov, N. A.; O'Brien, S.; Murray, C. B., Structural diversity in binary nanoparticle superlattices. *Nature* **2006,** *439* (7072), 55-59.

130. Porter, A. G.; Ouyang, T.; Hayes, T. R.; Biechele-Speziale, J.; Russell, S. R.; Claridge, S. A., 1-nm-Wide Hydrated Dipole Arrays Regulate AuNW Assembly on Striped Monolayers in Nonpolar Solvent. *Chem* **2019,** *5* (8), 2264-2275.

131. Huo, Z. Y.; Tsung, C. K.; Huang, W. Y.; Zhang, X. F.; Yang, P. D., Sub-two nanometer single crystal Au nanowires. *Nano Letters* **2008,** *8* (7), 2041-2044.

132. Wang, C.; Hu, Y. J.; Lieber, C. M.; Sun, S. H., Ultrathin Au nanowires and their transport properties. *J. Am. Chem. Soc.* **2008,** *130* (28), 8902-+.

133. Loubat, A.; Imperor-Clerc, M.; Pansu, B.; Meneau, F.; Raquet, B.; Viau, G.; Lacroix, L. M., Growth and Self-Assembly of Ultrathin Au Nanowires into Expanded Hexagonal Super lattice Studied by in Situ SAXS. *Langmuir* **2014,** *30* (14), 4005-4012.

134. Reiser, B.; Gerstner, D.; Gonzalez-Garcia, L.; Maurer, J. H. M.; Kanelidis, I.; Kraus, T., Multivalent bonds in self-assembled bundles of ultrathin gold nanowires. *Phys. Chem. Chem. Phys.* **2016,** *18* (39), 27165-27169.